THERMOMECHANICAL STUDY OF H13 TOOL STEEL

by

Léa EBACHER

THESIS PRESENTED TO ÉCOLE DE TECHNOLOGIE SUPÉRIEURE
IN PARTIAL FULFILLMENT FOR A MASTER'S DEGREE
WITH THESIS IN MECHANICAL ENGINEERING
M.A.Sc.

MONTREAL, MAY 15, 2024

ÉCOLE DE TECHNOLOGIE SUPÉRIEURE
UNIVERSITÉ DU QUÉBEC

BOARD OF EXAMINERS

THIS THESIS HAS BEEN EVALUATED

BY THE FOLLOWING BOARD OF EXAMINERS:

M. Mohammad Jahazi, Thesis Supervisor
Department of Mechanical Engineering, École de technologie supérieure

Victor Songmene, Chair, Board of Examiners
Department of Mechanical Engineering, École de technologie supérieure

Henri Champliaud, Board of Examiners
Department of Mechanical Engineering, École de technologie supérieure

THIS THESIS WAS PRENSENTED AND DEFENDED

IN THE PRESENCE OF A BOARD OF EXAMINERS AND THE PUBLIC

FEBRUARY 14, 2024

AT ÉCOLE DE TECHNOLOGIE SUPÉRIEURE

ACKNOWLEDGEMENTS

I sincerely thank M. Mohammad Jahazi, my thesis supervisor, for his expertise and availability offered throughout my master's degree. He shared some of his scientific knowledge with me and guided me to one of my biggest personal projects to date.

To my colleagues at ÉTS (Radu Romanica, Mohammad Saadati, Davood Shahriari, Simin Dourandish, Prashant Dondapure), thank you for your help during the experimental trials and the analysis of the results. To all CM2P members, thank you for your suggestions during my presentations.

À Finkl Steel qui a été un partenaire essentiel durant la réalisation du projet et qui m'a permis de travailler dans le domaine passionnant du forgeage des aciers, un gros merci. C'est un beau cadeau pour une métallurgiste. Je remercie toute l'équipe (spécialement Jean-Benoit Morin, Mario Boisvert, David St-Onge, Patrick Lambert, Guy Lamoureux et Abdelhalim Loucif) pour votre participation active et pour avoir bonifié ma recherche d'un point de vue pratique. Un merci spécial à Louis-Philippe Lapierre-Boire de m'avoir contactée avant la fin de mes études au baccalauréat pour me proposer cette opportunité de maitrise et d'emploi.

Je remercie les Fonds de recherche du Québec en nature et technologies pour la bourse octroyée à mon projet.

Pour terminer, merci à ma famille (Sylvie, Yves, Karl, papi, grand-papa, grand-maman), mon copain (Cédric), Ian et mes amis qui m'ont toujours soutenu dans ce que j'ai entrepris. Merci pour vos encouragements, vos conseils et votre écoute.

Étude thermomécanique de l'acier à outil H13

Léa EBACHER

RÉSUMÉ

H13 est un acier à outils utilisé notamment comme matrice d'extrusion ou de forgeage pour la mise en forme de métaux. Il se caractérise par sa haute stabilité thermique et son importante résistance à l'usure. Pour fabriquer des outils de grandes dimensions, des barres d'alliage H13 sont typiquement produites par forgeage à chaud en matrice ouverte de lingots coulés. Dans ce cas-ci, le défi réside dans la sélection des paramètres de forgeage qui influencent significativement l'évolution de la microstructure et les propriétés finales de la pièce, mais aussi la formabilité de l'alliage. Des paramètres inadéquats sont susceptibles d'engendrer des fissures de surface et des défauts internes lors du forgeage. Ce mémoire présente l'étude thermomécanique de l'alliage H13 dans le but de quantifier l'impact de différentes conditions de déformation sur l'évolution de la microstructure et de mieux comprendre les caractéristiques de cet acier. Spécifiquement, les cinétiques du grossissement des grains et de la dissolution des carbures sont déterminées pour différentes températures de forgeage. Puis, des essais de compression à chaud permettent la modélisation des courbes de contrainte et déformation.

Mots clés : H13, Forgeage, Acier à outil

Thermomechanical Study of H13 Tool Steel

Léa EBACHER

ABSTRACT

H13 is a hot work tool steel used as extrusion and and forging dies in metal forming industries. It is characterized by its high thermal stability and wear resistance. For large size tools, H13 alloy bars are generally produced by hot open-die forging of cast ingots. However, the selection of the hot forging parameters significantly influences the evolution of the microstructure, and hence the final properties, as well as the formability of the alloy, which may lead to surface cracks and internal defects during forging. In the present work, a thermomechanical study of H13 was conducted to quantify the impact of different deformation conditions on microstructure evolution and to better understand the characteristics of this steel. Specifically, the kinetics of grain growth and carbide dissolution at different forging temperatures were determined. Then, hot compression tests enabled the modelling of stress strain curves.

Keywords: H13, Forging, Grain growth, Carbide dissolution, Modelling, Hot work tool steel

TABLE OF CONTENTS

LIST OF TABLES

Page

LIST OF FIGURES

LIST OF ABREVIATIONS AND ACRONYMS

BCC	Body-centered lattice
DRV	Dynamic recovery
DRX	Dynamic recrystallization
EDS	Energy dispersive X-ray spectroscopy
FCC	Face-centered lattice
FE	Finite element
FM	Free from Mannesmann effect (after upset, deformation of the workpiece laid on its side using an intermediate plate)
FML	FM on the workpiece length to increase its width
H&S	Hansel and Spittel model
JC	Johnson-Cook model
SEM	Scanning electron microscope
SH	Strain hardening
SRV	Static recovery
SRX	Static recrystallization

LIST OF SYMBOLS

A	Surface area [mm^2]
α	Model constant in Arrhenius [MPa^{-1}]
β	Constant in Arrhenius model
b	Barreling factor
D	Average grain diameter [µm]
d_0	Initial average grain size [µm]
E	Young Modulus [MPa]
Er	Average absolute relative error
ε	Strain
$\dot{\varepsilon}$	Strain rate [s^{-1}]
h	Height [mm]
L_0	Initial length [mm]
m	Strain rate sensitivity or inverse of the time exponent for grain growth
n	Strain hardening coefficient [MPa^{-1}]
n_g	Grain growth exponent
P	Applied force [N]
Q	Activation energy [$J.mol^{-1}$]
R	Universal gas constant [8,314 $J.mol^{-1}.°K^{-1}$]
r	Radius [mm]
σ	Stress [MPa]
t	Time [s]
T	Temperature [°C or °K]

θ	Work hardening
μ	Friction coefficient
v	Press speed [mm/s]
X	Recrystallized fraction
Z	Zener-Hollomon parameter

INTRODUCTION

Sorel facility of Finkl Steel Co. is devoted to the manufacture of specialty steel forgings and ingots. It produces large pieces of mold and tool steels, used in key sectors such as aerospace, energy and automotive. These dynamic sectors are seeing many technological advances requiring steel components that have more complex compositions, higher strength and hardness or require a specific set of mechanical properties. Consequently, Finkl Steel - Sorel tries constantly to overcome these challenges and produce forgings with improved mechanical properties to meet new demands and stay competitive on the market.

Forged bars of H13 alloy are one of the products recently introduced at Finkl Steel - Sorel. These pieces are used as extrusion and forging dies for ductile materials forming processes. However, recent tests led to a negative outcome: Several bars forged with the standard process showed important defects leading to rework and rejection of parts. Most defects were unclosed porosities up to 6.35 mm in diameter, located at the centerline. A thermomechanical study of H13 alloy will therefore help to better understand the effect of the different process variables and will provide guidelines for the modifications of the fabrication process that will improve the success rate.

CHAPTER 1 LITERATURE REVIEW

This literature review is a survey and discussion to evaluate previous and current researches on how it relates to the problematic. The aim is to gather important knowledge and provide a solid background for this present research. Specifically, it includes an overview of the process, starting with the origin of the porosities in the steel and the description of hot forging operations. It discusses the impact of different parameters on the effectiveness of porosities closure. Then, it explores stress strain flow curves characteristics and modelling. It also studies a few simulation cases. Finally, this chapter reviews the characteristics of H13 tool steel alloy.

1.1 Origin of Porosities in Forged Steels

Porosities are generated during the solidification of liquid steel poured into ingot molds. As the liquid steel temperature decreases, first germs of solid material nucleate at preferential sites (Campbell, 2011). Ingot walls are where the cooling rate is the highest, consequently solidification occurs from walls towards the center. Inclusions and elements with higher fusion temperatures also favour nucleation because they crystallize at higher temperatures. As the liquid continues to solidify, the material builds up on the initial germs in preferential directions with a dendritic shape. The growth of germs in a dendritic shape leaves pockets of liquid between the arms that are surrounded by a mushy zone and then a solid shell (Lan, 2014). Shrinkage occurs when the density rises as the material solidifies, which is the case for steels. Therefore, this densification leaves macro and micro shrinkage porosities between dendrite arms if the surrounding liquid steel cannot reach the retracting regions and fill them. According to Chen (2012), gas evolution may also cause porosities in the ingot. The gas bubbles must reach the top of the ingot before solidified material blocks them.

In large size ingots, the solidification is slow and the cooling rate through the ingot varies. Thus, ingots present large areas with porosities and segregated elements. A typical pattern is shown in Figure 1.1. The casting porosities are in larger volume fraction in the upper middle and center region of the ingot, because the cooling rate is higher near the walls and lower at the top due to the insulated feeder sometimes accompanied by exothermic panels.

Segregation bands of alloying elements are found between the centerline and the external surface (“A”) or along the centerline (“V”). Loucif (2018) shows that the enriched areas are still present after the forging process for large ingots.

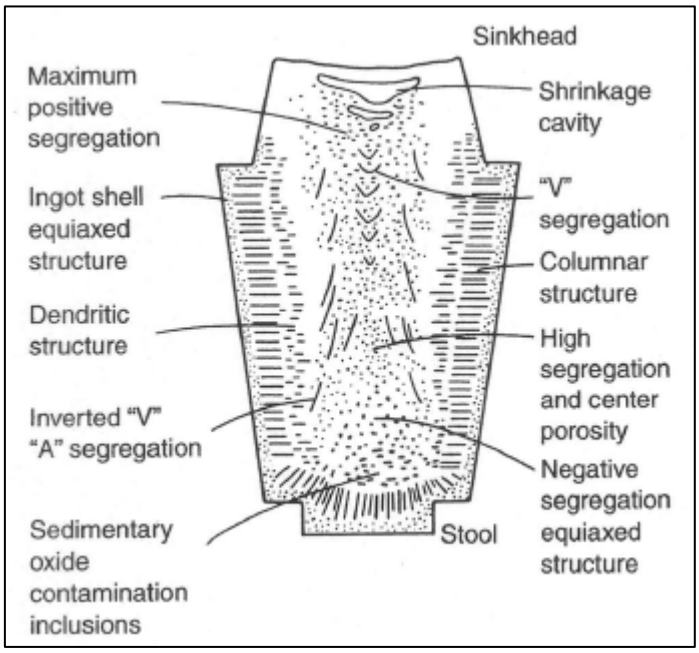

Figure 1.1 Macrosegregation in large steel ingot
Taken from
ASM Handbook Vol. 14 “Open Die Forging” (1988)

1.2 Hot Open Die Forging

Open die forging consists of compressing a piece between a set of dies for a series of blows to achieve a desired shape. In this work, the production of very large workpieces is studied, so only a portion is deformed at each stage. The process is therefore incremented until all the surface is shaped. Along with dimensioning, hot forging of cast ingots has many other important roles: breaking down the cast microstructure, closing internal porosities, redistributing the segregated elements and refining the grain size. These major microstructural changes are achieved through a complex thermomechanical cycle that consists of heating the piece at temperatures well above 0.6Tm (melting point) and applying an adapted sequence of compressive forces that could include up to 200 blows. When heating steel at forging temperature, it makes a phase transition from body-centered cubic lattice to

face-centered cubic lattice (austenite). This transition results in an increase in density and increase in ductility (« Open Die Forging », 1988). In addition, the high temperature and energy generated by the deformation allows the transformation of the columnar and equiaxed grains into much smaller size grains through the recrystallization process. This aspect is discussed in the section on the stress-strain flow curve.

1.2.1 Forging Sequence

Figure 1.2 shows the typical forging sequence of a bar.

a) The upsetting step compresses the cast ingot perpendicularly to its longitudinal axis and increases the cross section. An intermediate plate and the floor are used as anvils to apply the force on the entire top and bottom sections of the piece. This step has the biggest impact on the consolidation because the length can be reduced up to 40% for large ingots.

b) The FM process (free from Mannesmann effect) uses the same tools as the upset, but the ingot is laid down on its side. The term FML is used when in addition to the upper and lower sides, the adjacent side is also deformed. This step can follow the upset and FM operation if the width of the forging needs to be a lot bigger. FM is also associated with high deformation of the material, thus it can be performed to increase even more the consolidation after upset.

c) The cogging process elongates the piece along its longitudinal axis with successive blows. Each blow can overlap the previous or the full die width can be used. The latter leaves a mark between the blows that can be intentionally positioned near the middle of the die at the next pass, to ensure a systematic and homogeneous deformation of the part. To reach a round shape, intermediate shapes can be given to the piece. In general, a rough cogging step reduces the cross section when it is a square. Then, the piece is rotated 45° and brought to an octagon shape with dimensions close to the final diameter. The finishing cogging step gives a round shape to the piece as the pass is accomplished with small displacements and small rotations at each blow. For the deformation in octagon or round shapes, “V” or round dies can be used.

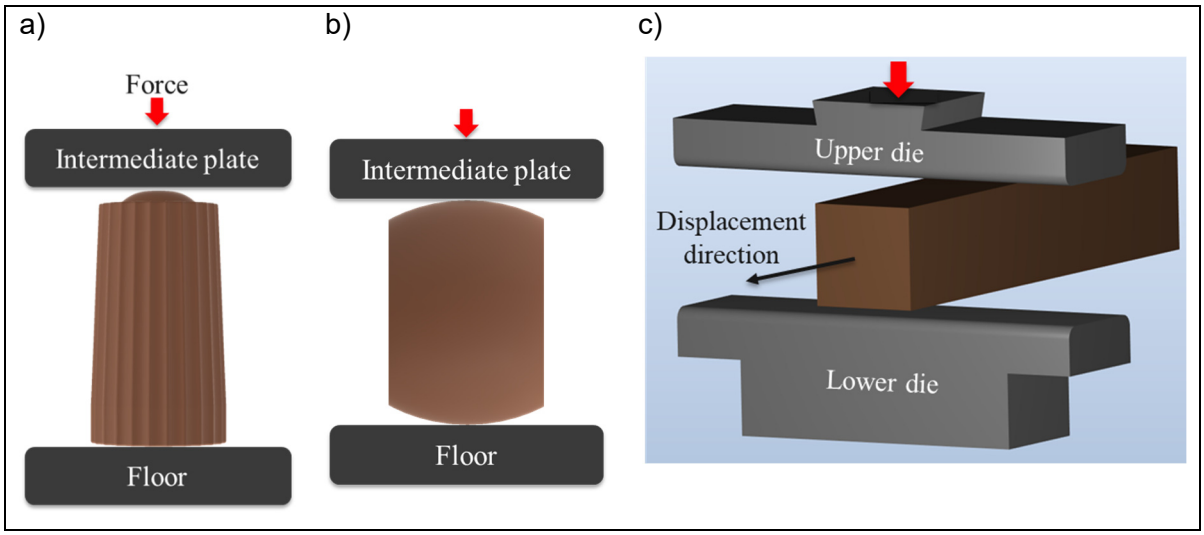

Figure 1.2 Typical forging sequence of a bar, (a) Upset, (b) FM, (c) cogging

1.2.2 Porosity Closure

Two principal phenomena lead to porosity closure: mechanical closure and material healing (Harris, 2016). Mechanical closure has the most important impact on the size of the porosities and is achieved with the forging process. On the other hand, material healing has a milder effect and is active when the steel is heated at a temperature allowing significant atomic diffusion. This mechanism of porosity closure is effective during both forging and heat treatment processes. Thus, porosity closure must be completed through the forging process because no subsequent step will impact much.

Depending on the material properties at time of deformation, an optimal stress state in the cast ingot allows mechanical closure of porosities. Specifically, from a mechanical perspective, two important conditions are:

a) The stress must exceed the elastic yield of the material and allow a permanent plastic deformation. Many researches show that effective strain has a strong and direct relationship on porosity closure (Lee, 2008 ; Wen, 2018). The larger the effective strain is in an area, the smaller the cavity size.

b) Triaxial compressive stress efficiently closes the porosities, especially during radial deformation. Lee (2008) shows that hydrostatic pressure has indirect and secondary influence on porosity closing by comparing two porosities with nearly the same applied effective strain. Tamura (1984) studied the characteristic stress state at the centerline of a bar with different forging processes. He concluded that a larger die width to workpiece thickness ratio generates triaxial compression. Biaxial and uniaxial compressions are achieved when the ratio is low. In these cases, the porosities in the centerline are in tension in the longitudinal direction and also in the transverse direction for the uniaxial compression. Figure 1.3 summarizes the different characteristic stress states during radial compressive deformation. Uniaxial or biaxial tension stresses may reopen nearly closed porosities.

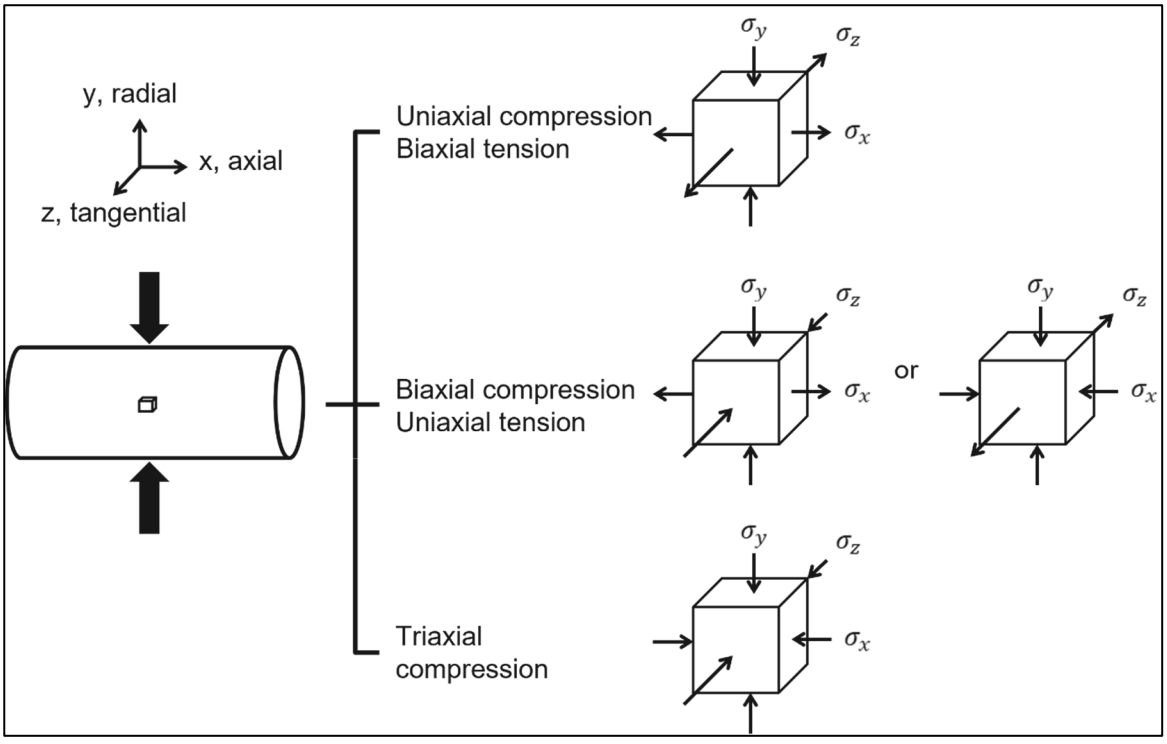

Figure 1.3 Characteristic stress states at the center of a bar during radial compressive deformation
Adapted from Tamura (1984)

Researches on mechanical porosity closure highlights many process parameters that impact the stress distribution and effectiveness of consolidation.

Temperature gradient has an effect, especially on porosities along the centerline. Hot deformation in the center is enhanced when the gradient is high from the surface to the center. When the surface is cooler, its flow stress is higher and the compressive force is transferred to the centerline. Thus, the consolidation is increased near the critical area of the ingot with the most porosities. To take benefit from the presence of temperature gradient, the workpiece may be deliberately air cooled from the soaking temperature before forging (ASM Handbook Vol. 14 "Open Die Forging", 1988 ; Tamura, 2003)

Friction coefficient affects the material behaviour near the surface in contact with the die. The metal flow is constrained by the frictional force and a dead zone is created in the surface region of the workpiece under the die. The higher the coefficient, the lower the material flow. However, the friction can be reduced with lubrication of the contact surface.

Buckingham (2016) illustrated the strain distribution after upset of a small sample. Their simulations show that the lowest effective strain is located at the center of the upper and lower surfaces which are in contact with the die, as illustrated in Figure 1.4.

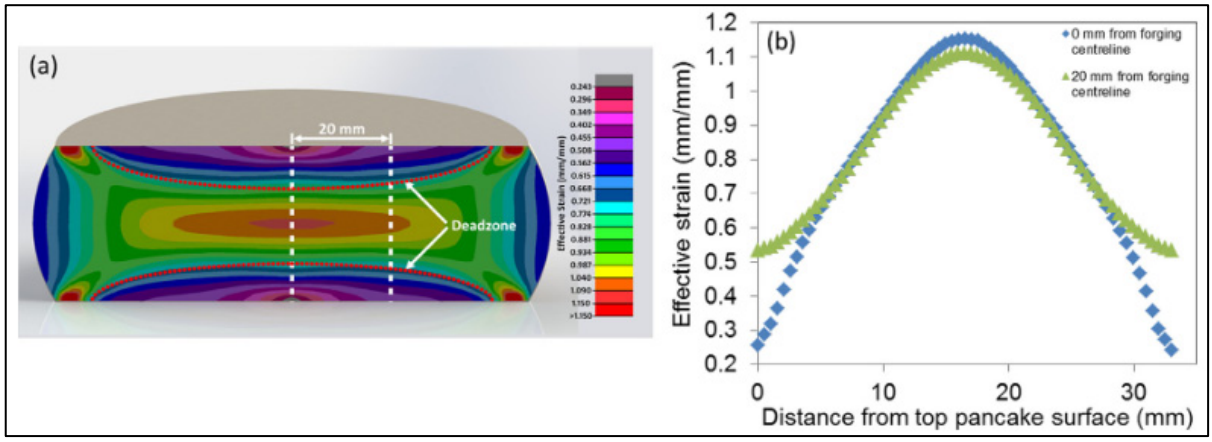

Figure 1.4 Strain distribution in sample after upset
Taken from Buckingham (2016)

Design of the working surface of the dies, also called anvils, influences the dead zone region caused by tool contact. If the die width is narrow and the press capacity is small, the depth of deformation will be small. According to Tamura (2003), for the same feed (longitudinal distance between hits) a smaller radius of die edge will increase the friction surface and the dead zone, which encourages the strain penetration. Regarding the die shape, Chen (2012)

found that “V” dies can provide much larger plastic deformation area than flat dies for radial forging with a mandrel. Buteler (2006) compared the stress state with different die shapes in a AISI 1045 cylinder using a finite element analysis software. For the same reduction in cylinder diameter, flat dies provided equivalent strains more concentrated in the middle of the cross-section, while “V” dies resulted in more uniformly distributed and more intense equivalent strains over the cylinder cross-section. In this particular case, “V” dies are better to favour a higher effective strain at centerline.

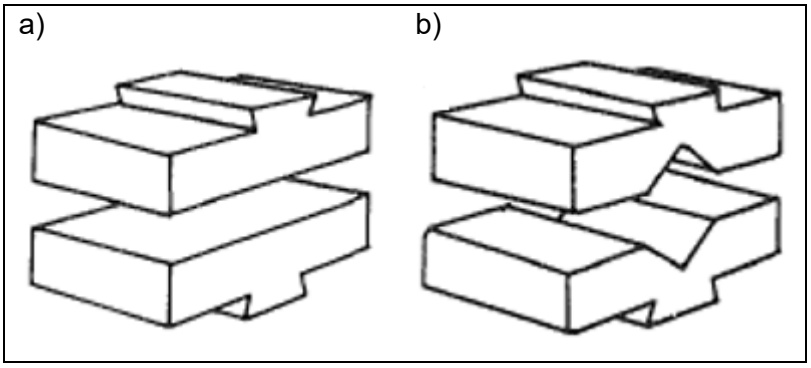

Figure 1.5 Die shape, (a) flat, (b) V

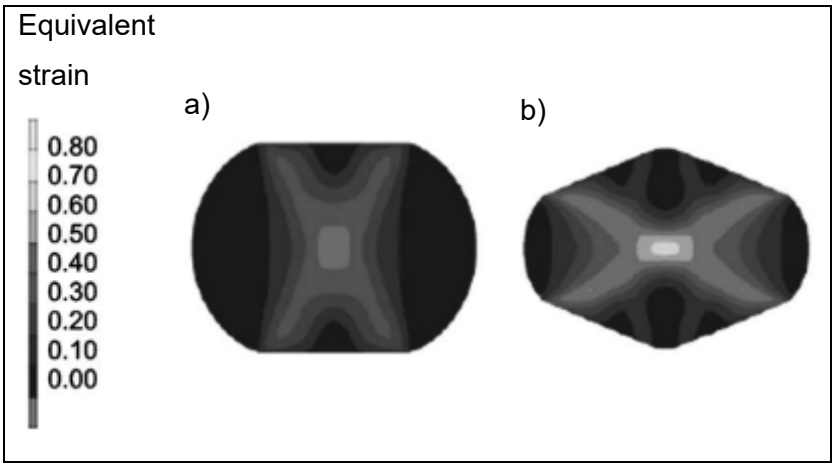

Figure 1.6 Effect of die design on distribution of equivalent strain (a) flat dies, (b) V dies Taken from Buteler (2006)

Deformation pattern, including magnitude of stroke and feed, has a significant impact on stress distribution. Since the dies width is small compared to the overall length of the

workpiece, the non-uniform deformation and zone affected by prior blows must be considered because they influence the subsequent passes.

Tamura (2003) studied the influence of operational conditions on equivalent plastic strain at the center of a forged piece. He found that the larger the magnitude of the stroke, the larger the strain. This also means that as the feed becomes large, the heterogeneity of the strain becomes worse at the center. The strain is higher at the central axis of the bite, but it is lower between the bites. This variation of strain is due to the dead metal region just below the contacting surface that acts as a rigid body and transfers the energy of the stroke deeper in the forging. However, with this kind of deformation pattern, low strain at the surface results in poor grain refinement at the surface. Tamura (2003) also mentions that it is required to refine the grain at both surface and center. It is especially important at the surface because insufficient refinement in this area may lead to forging defects generation in the subsequent strokes. Such surface cracks could propagate deep into the workpiece. In the same article, the author analyzes different passes schedules and concludes that the grain size refinement at the surface can be increased with an optimized schedule taking into account the plastic strain distribution due to friction at the contact surface.

Choi (2006) found that a feed rate of 0.6 times the target diameter of a round bar is optimal for productivity and roundness of the product. However, his study does not consider internal quality of the final piece.

Grain size evolves before and during forging. Heating and holding at forging temperature, before deformation, will affect the austenite grain size. The growth behavior under isothermal conditions varies according to the soaking temperature, the alloy composition, its precipitates and its thermal history. Experimentally, it is found that grain growth in single phase metals follows (Porter & Easterling, 2009a):

$$D = Kt^{n_g} \tag{1.1}$$

Where D is the average grain size, t is the holding time, n_g is the grain growth exponent and K is a proportionality constant increasing with temperature. It is found that n_g approaches 0.5

in very pure metals or at very high temperature and will be much less with presence of precipitates. Also, the above equation can be applied for normal grain growth.
The following Arrhenius type constitutive equation is also used to explain the kinetics of the austenite grain growth in medium carbon low alloy steel under isothermal austenitization conditions (Chentouf, Chamanfar, & Jahazi, 2020):

$$D = \left[d_0^m + A\ t\ exp\left(-\frac{Q}{RT}\right)\right]^{\frac{1}{m}} \tag{1.2}$$

Where D is the average grain size, t is the holding time, d_0 is the initial average grain size, m is the inverse of the time exponent for grain growth, A is a constant, Q is the activation energy, R is the universal gas constant and T is the austenitizing temperature. By taking the natural logarithm from both sides, the m and Q are defined. $1/m$ is the slope of $\ln d$-$\ln t$ graph at constant temperature and the Q is equal to the slope of the $\ln d$- $ln(1/T)$ graph times $-mR$ at constant holding time:

$$\frac{1}{m} = \left.\frac{\partial \ln D}{\partial \ln t}\right|_T \tag{1.3}$$

$$Q = -mR \left.\frac{\partial \ln D}{\partial ln(1/T)}\right|_t \tag{1.4}$$

Occasionally, discontinuous grain growth, coarsening, or secondary recrystallization occur due to the presence of segregation or precipitate arrays. He (2013) conducted heating-holding tests on 30Cr2Ni4MoV steel samples. He observed that a critical temperature exists above which certain austenite grains with favourable orientation grow much faster. This temperature is characterized with dissolution of second phase particles such carbides, nitrides and sulfides, and weakening of their pinning effect. There is no information about the grain growth kinetic and critical temperature for H13 hot work tool steel, which is rich in alloying elements and second phase particles.

Stability is reached as the three-dimensional polycrystalline structure gets closer to 120° angle at each boundary junctions and the grains are of a hexagonal shape. In Figure 1.7 (Porter & Easterling, 2009), the motion of grain boundaries is illustrated. Convex grains shrink as

concave grains enlarge. The volume fraction of precipitates will control the maximum grain size attainable. The particles will exert a pulling force on the boundaries and restrict its motion. As the grains enlarge, the driving force decreases until it is insufficient to overcome the drag of the particles and thus the grain growth stagnates.

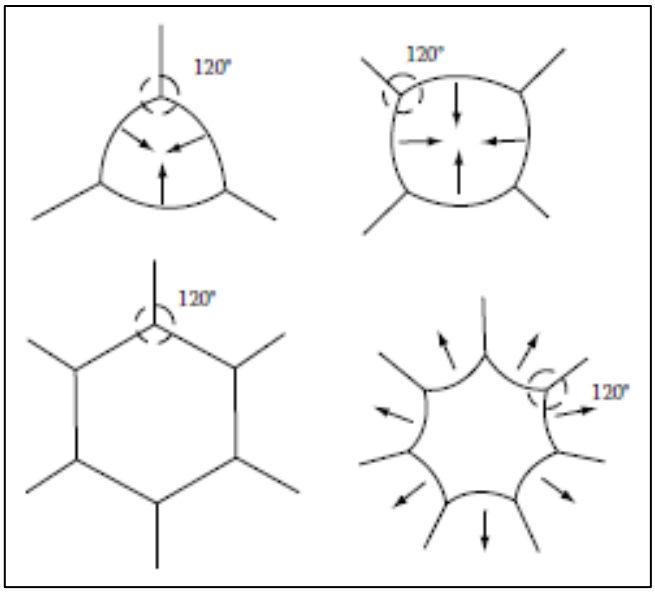

Figure 1.7 Grain boundaries migration during grain growth in 2D configuration Taken from Porter & Easterling (2009)

At the time of deformation, the grain size influences the hot ductility of the material because of its effect on Dynamic Recrystallization (DRX), as resumed by Connolly (2015). With a finer initial grain size, the energy required to initiate DRX is lower, thus critical recrystallization strain and temperature are lower. With DRX, more severe work hardening can be achieved. In large as cast ingots, the grain size and morphology will differ from surface to center, consequently the hot ductility will also differ. DRX is described in section 2.3.1.

Precipitates (carbides, nitrides and sulfides) are identified as the main sources for ductility loss (Connolly, 2015). Precipitation of some carbides and nitrides occurs preferentially at austenite grain boundaries because of the lower misfit and faster diffusion coefficient. The grain boundary becomes a strengthened or weakened area which could be preferentially deformed. This may create microvoids when strain becomes localized and very high. The precipitates will also delay the Dynamic Recovery (DRV) and Recrystallization (DRX) by

pinning dislocations and cell walls. During hot forging, their fraction in the material varies according to their dissolution temperature and kinetics as well as morphology. Long isothermal holding tests were conducted in the current study to help understand the critical conditions to promote dissolution of carbides in H13 before forging operations.

1.2.3 Porosity Created during Forging

The previous sections discussed on how hot forging closes more or less efficiently porosities in cast ingots. However, in some particular conditions, the opposite result may occur.

Hot forging may create new voids as the material flows. During plastic deformation, dislocations in the metal glide or climb up to the grain boundary intersection. So, they may pile up at a triple point or at the interface of a second phase particle and form a cavity.

Secondary tensile stress is also identified as a void reopening factor. Krishna (2019) analysed each step of the forging process of a carbon steel axle forging which had showed internal cracks. It was concluded that the center burst of the axle forging resulted from a high concentration of non-metallic inclusions in the central portion of the raw bar stock. However, the presence of these defects alone did not create the porosities. The high radial/lateral flow of material during the deformation generated substantial tensile stresses in the flow direction that internally tore apart the weakened material. Therefore, a strict control of the inclusions contained in the raw material is important for a biaxial and uniaxial compression stress state. These secondary tensile stresses, also called the Mannesmann effect are produced when a perpendicular compressive force is applied to the workpiece (« Open Die Forging », 1988) and may result in the formation of cavities along the longitudinal axis of bars subjected to highly inhomogeneous radial deformation as explained by Ghiotti (2009).

A high hydrogen content may also create defects related to voids. A non-uniform cooling may favour a positive segregation of this light element. When the concentration reaches a critical value, the light element combines with other atoms and the resulting gas locally raises the pressure that makes the material burst. The particularity of these defects is that they are in the shape of flakes. This phenomenon often occurs in central top zones or heavy sections of forgings with more than 2 ppm of hydrogen measured in the ladle (Tremaine, 2005).

1.3 Stress Strain Flow Curves

The stress-strain flow curve gives the stress required to cause the metal to flow to any given strain (Dieter, 1988). It provides a graphical measure of a material's formability under specific conditions.

Eq. (1.5) defines the true stress (σ) as the applied force (P) divided by the area of application (A). Eq. (1.6) defines the true strain (ε) as the change in linear dimension (L) divided by the instantaneous value of the dimension.

$$\sigma = \frac{P}{A} \tag{1.5}$$

$$\varepsilon = \int_{L_0}^{L_f} \frac{dL}{L} = ln\left(\frac{L_f}{L_0}\right) \tag{1.6}$$

1.3.1 Stages

A typical curve is illustrated in figure 1.8. It is characterized by four stages (Chadha & Shahriari, 2015) and three major sets of strain and stress values: elastic or yield (σ_0,ε_0), plastic or peak (σ_p,ε_p), and steady state (σ_s,ε_s).

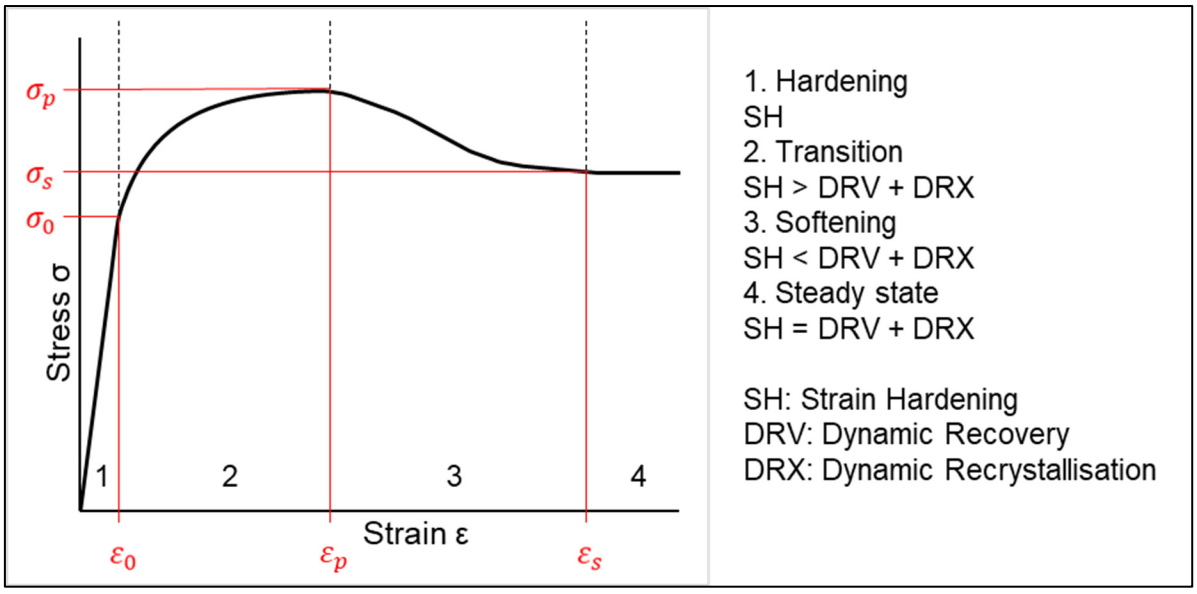

Figure 1.8 Typical stress-strain flow curve and stages

1.3.1.1 Strain hardening (SH)

In the first stage, increase in strain requires higher stress. This is due to an accumulation of dislocations; the density of dislocations increases. The relation is proportional up to (σ_0,ε_0), following Hooke's law described in Eq. (1.7), where E is the Young Modulus. During this stage, the deformation is called "elastic", meaning that the deformation is reversible and depends only on the initial and final states of stress and strain.

$$\sigma = E\varepsilon \qquad \text{For } \sigma < \sigma_0 \tag{1.7}$$

1.3.1.2 Transition stage

From the transition stage and beyond, the strain is "plastic". Part of the deformation is not reversible and depends on the loading path by which the final state is achieved. The following power equation is the most common expression for the portion from the beginning of plastic flow to the maximum load.

$$\sigma = K\varepsilon^n \qquad \text{For } \sigma_0 < \sigma < \sigma_p \tag{1.8}$$

K is a strength coefficient which corresponds to the stress at $\varepsilon = 1.0$ (MPa) and n is the strain hardening coefficient.

From the maximum load, stress may decrease or reach stability by the activation these mechanisms:

a) Dynamic recovery (DRV)

Beyond a critical density, the movement of dislocations enabled by deformation and temperature will allow the suppression of dislocations and reduce the stress. Structural changes that do not involve high angle boundary migration and do not change texture will occur:

- Annihilation and rearrangement of dislocations (dislocations of opposite signs on the same slip plane will attract and annihilate each other, and dislocation climb will also occur by the diffusion of vacancies or interstitials);
- Polygonization (dislocations migrate and line up in small angle tilt boundaries to form subgrains that will grow);
- Formation of recrystallization nuclei (with some nuclei energetically capable of growth).

The principal factors that favour DRV are high stacking fault energy, low volume fraction of precipitates, high strain and high deformation temperature (Dieter, 1988).

b) Dynamic recrystallization (DRX) and grain growth

DRX is the predominant softening mechanism in the hot working of all FCC metals except aluminum. During deformation, energy is stored in the material in the form of additional dislocations and increased grain boundary surface. Therefore, to lower the energy, new grains nucleate and grow to consume and replace the polygonized matrix. In general, DRX is divided in two parts:

- Formation of stable nuclei by coalescence of subgrains that lead to high angle boundaries and apparition of new grains;

- Growth of new grains by migration of high angle boundaries.

It is possible to observe a recrystallization texture because not all grains will grow at the same rate. Grains specially oriented with respect to the matrix will have boundaries with higher mobility. Also, a highly deformed or fine subgrained matrix will provide more energy for growth. The principal factors that favour DRX are high strain, specific strain texture, small initial grain size, low volume fraction of precipitates and high deformation temperature.

The kinetics of recrystallization can be quantified by Avrami equation (Bitterlin & Shahriari, 2018):

$$X = 1 - \exp(-kt^{n_{DRX}}) = 1 - \exp\left[-k\left(\frac{\varepsilon - \varepsilon_c}{\varepsilon_p}\right)^{n_{DRX}}\right] \quad (1.9)$$

Where X is the recrystallized fraction, ε_c is the critical strain at which the first nuclei of recrystallized grain appears, ε_p is the peak strain, k and n_{DRX} are dynamic recrystallization parameters corresponding to the Avrami constant and the time exponent, respectively. ε_c is hard to identified graphically, but the double differentiation method (Eq. (1.3) and (1.4)) was proved accurate by Najafizadeh (2006) and Bitterlin (2018).

$$\theta = \frac{\partial \sigma}{\partial \varepsilon} \quad (1.10)$$

$$-\frac{\partial \theta}{\partial \sigma} \quad (1.11)$$

Both DRV and DRX are softening mechanisms happening simultaneously at high deforming temperature with sufficient driving force. They are hard to be distinguished because recovery can create initiation sites for recrystallization (Humphreys, 1995). In addition, at high temperature, probability of DRV is high and this reduces the energy stocked in the deformed microstructure. Thus, as the deformation temperature will increase, the DRX temperature will also increase.

1.3.1.3 Softening

During softening stage, the strain hardening effect is lower than the softening effect of DRX and DRV. Thus, the stress needed to continue the deformation decreases.

1.3.1.4 Steady state

Steady state is achieved at the last stage. The strain hardening effect is equivalent to the softening effect of DRX and DRV.

It is worth mentioning that after deformation, but before any significant drop in temperature, both static recovery (SRV) and recrystallization (SRX) may occur and be followed by grain growth for alloys with low to medium stacking fault energy, such as alloyed steel (Dieter, 1988 ; « Open Die Forging », 1988). The softening processes will occur depending on the level of deformation and the energy stored in the material. If recrystallization takes place with no incubation time, it is known as “postdynamic” or “metadynamic”.

1.3.2 Effect of Temperature

Increase in temperature will lower the stress required to deform. When the temperature is higher, the critical dislocation density to activate DRV and DRX is lower due to the additional energy provided by the heat. The ductility of the material is also increased due to the higher mobility of the dislocations. However, structural changes may occur in certain temperature range and alter this behaviour: precipitation, recovery, recrystallization and phase transformation. The effect of temperature on flow stress at constant strain and strain rate is generally represented by Eq. (1.12).

$$\sigma = Ce^{Q/RT}\Big|_{\varepsilon,\dot{\varepsilon}} \tag{1.12}$$

figure 1.9 shows tensile curves at an engineering strain rate of approximately 0.0004 s^{-1} and different temperatures for quenched H13 samples (Lin, 2016). At room temperature, the

extremely high strength and the moderate ductility are attributed to the martensitic matrix with the dispersion of carbide precipitates. At higher temperature, the Young modulus, yield strength and ultimate strength are lower, and elongation is higher.

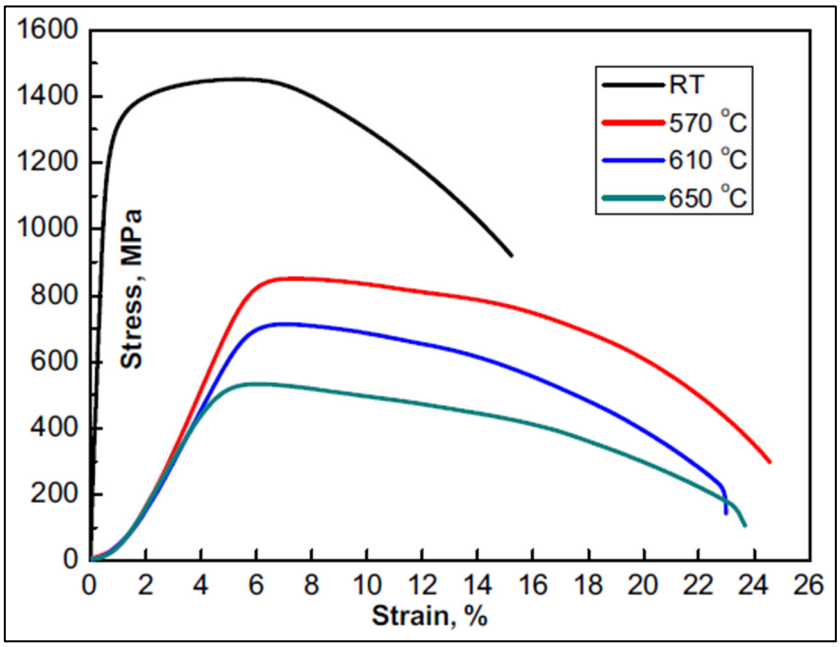

Figure 1.9 Stress-strain curves of quenched H13 at different temperatures
Taken from Lin (2016)

1.3.3 Effect of Strain Rate

The strain rate is defined in Eq. (1.13) as the deformation speed divided by the workpiece length. A general relationship between flow stress and strain rate, at constant strain and temperature is represented in Eq. (1.14), where m is known as the strain rate sensitivity. The strain rate dependence of stress increases with increasing temperature. Thus, m increases with temperature and is commonly in the range 0.1-0.2 in hot working. Arrhenius-type model is also used to describe the relationship:

$$\dot{\varepsilon} = \frac{d\varepsilon}{dt} = \frac{v}{L} \tag{1.13}$$

$$\sigma = C\dot{\varepsilon}^{m}|_{\varepsilon,T} \tag{1.14}$$

Strain rate and flow stress show a strong proportional relationship. A higher flow stress is achieved at higher strain rates because of a deceleration in dislocation annihilation. The accumulation of dislocations in misfit areas (grain boundaries and near precipitates) might cause anisotropic deformation accompanied with localized DRV and DRX (W. Wang et al., 2018).

1.3.4 Zener-Hollomon Parameter

As described above, the temperature and strain rate influence the flow stress. The Zener-Hollomon parameter, Z, suggests a useful relation that describes the combined effect of temperature and strain rate (Chadha & Shahriari, 2015 ; Dieter, 1988). It is defined as:

$$Z = \dot{\varepsilon}\, exp\left(\frac{Q}{RT}\right) \tag{1.15}$$

Where $\dot{\varepsilon}$ is the strain rate, Q is the activation energy for deformation, R is the universal gaz constant and T is the deformation temperature. The Z parameter quantifies the relative activity of various deformation mechanisms that are typically inversely proportional to temperature or strain rate. For example, a decreasing strain rate or increasing temperature will increase Z. Zhang (2013) reported that for high deformation temperature and low strain rate (low Z values), the driving force for DRX increases. This results in earlier DRX, and peak stress occurs at lower strains. Conversely, at low temperatures and high strain rates (high Z value), the driving force decreases and DRX is delayed.

1.3.5 Modelling

Compared to room temperature, flow stresses at elevated temperature are complicated to predict because of the activation of hardening and softening mechanisms at different strain levels. Several practical approaches have been developed to describe accurately the flow stress behaviour.

Ebrahimi (2006) suggested the form of Eq. (1.16) and (1.17) for the strain hardening and softening stages as a function of σ_p and ε_p, where C_1 and C_2 are constants of the material that would be weakly dependant on T and $\dot{\varepsilon}$. Their suitability were shown for application to a hot worked Ti-IF steel. However, these equations are not adapted for changing T and $\dot{\varepsilon}$ and thus cannot be integrated into a hot deformation simulation software.

$$\sigma = \sigma_p \left[\left(\frac{\varepsilon}{\varepsilon_p} \right) exp\left(1 - \frac{\varepsilon}{\varepsilon_p} \right) \right]^{C_1} ; \varepsilon \leq \varepsilon_p \tag{1.16}$$

$$\sigma = \sigma_S + (\sigma_p - \sigma_s) exp\left[C_2 \left(\varepsilon - \frac{\varepsilon_p}{2} - \frac{\varepsilon^2}{2\varepsilon_p} \right) \right]; \varepsilon \leq \varepsilon_p \tag{1.17}$$

The Hansel and Spittel (H&S) model in Eq. (1.18) predicts a viscoplastic flow stress considering material phenomena such as strain hardening, material softening, material sensitivity to strain and coupled effects with the temperature (Harris, 2016). The constant A is a corrective model coefficient and m_1 a temperature dependant exponent. The model's material dependant constants m_2 and m_3, correspond respectively to the Norton and strain rate sensitivity exponents. The constants m_4 to m_7 are other material parameters that may be taken as zero.

$$\sigma = A e^{m_1 T} \varepsilon^{m_2} \dot{\varepsilon}^{m_3} e^{\frac{m_4}{\varepsilon}} (1 + \varepsilon)^{m_5 T} e^{m_6 \varepsilon T^{m_7}} \tag{1.18}$$

The Arrhenius constitutive model in Eq. (1.19) is widely used to correlate the flow stress behaviour when recovery and recrystallization take place (Chadha & Shahriari, 2015). It can take into account the dynamic softening behaviour of the material, which can be observed at high temperatures and low strain rates. It is based on the Zener-Hollomon parameter Z in Eq. (1.20). Eq. (1.21), a Arrhenius-type model, describes the relationship between the strain rate $\dot{\varepsilon}$, flow stress σ, activation energy for deformation Q, universal gas constant R and the deformation temperature T, where A, α, n_1, n and β are material constants with $\alpha = \beta / n_1$.

$$\sigma = \frac{1}{\alpha} ln \left\{ \left(\frac{Z}{A} \right)^{1/n} + \left[\left(\frac{Z}{A} \right)^{2/n} + 1 \right]^{1/2} \right\} \tag{1.19}$$

$$Z = \dot{\varepsilon} exp\left(\frac{Q}{RT} \right) \tag{1.20}$$

$$\dot{\varepsilon} = AF(\sigma)exp\left(-\frac{Q}{RT}\right) \tag{1.21}$$

Where,

$F(\sigma) = \sigma^{n_1}$ $(\alpha\sigma < 0.8)$

$F(\sigma) = exp(\beta\sigma)$ $(\alpha\sigma > 1.2)$

$F(\sigma) = [\sinh(\alpha\sigma)]^n$ (for all σ)

The equations above do not take into account the deformation strain. It is compensated in polynomial equations for α, n, Q and A where the independent variable is ε, by:

$$\begin{aligned} \alpha &= B_0 + B_1\varepsilon + B_2\varepsilon^2 + \cdots + B_m\varepsilon^m \\ n &= C_0 + C_1\varepsilon + C_2\varepsilon^2 + \cdots + C_m\varepsilon^m \\ Q &= D_0 + D_1\varepsilon + D_2\varepsilon^2 + \cdots + D_m\varepsilon^m \\ \ln(A) &= E_0 + E_1\varepsilon + E_2\varepsilon^2 + \cdots + E_m\varepsilon^m \end{aligned} \tag{1.22}$$

The constants α, n, Q and A are calculated at varying strain, to develop the polynomial equations. They are found by inserting the value of $F(\sigma)$ in Eq (1.21). For low level and high level stress:

$$\begin{aligned} \dot{\varepsilon} &= B\sigma^{n_1} \\ \dot{\varepsilon} &= B'\exp(\beta\sigma) \end{aligned} \tag{1.23}$$

Where B, n_1 and B' are constants independent of deformation temperatures. Eq. (1.24) is obtained by taking logarithm on both sides and rearranging. Then, at various values of strain, plotting graphs of $\ln(\sigma)$ vs $\ln(\dot{\varepsilon})$ and σ vs $\ln(\dot{\varepsilon})$ and using linear regression gives the values of n_1, β and α ($\alpha = \beta/n_1$). The average of the slopes from different temperature is used.

$$\begin{aligned} \ln(\sigma) &= \frac{\ln(\dot{\varepsilon})}{n_1} - \frac{\ln(B)}{n_1} \\ \sigma &= \frac{\ln(\dot{\varepsilon})}{\beta} - \frac{\ln(B')}{\beta} \\ n &= \frac{\partial \ln(\dot{\varepsilon})}{\partial \ln(\sinh(\alpha\sigma))} \end{aligned} \tag{1.24}$$

$$Q = nR\frac{\partial \ln(\sinh(\alpha\sigma))}{\partial\left(\frac{1}{T}\right)}$$

For n, Q and $\ln(A)$, Eq. (1.21) is rearranged after taking logarithm on both sides:

$$\ln(\sinh(\alpha\sigma)) = \frac{1}{n}\ln(\dot{\varepsilon}) + \frac{Q}{nRT} - \frac{1}{n}\ln(A) \tag{1.25}$$

T and $\dot{\varepsilon}$ are taken as independent variables. Then, plotting graphs of $\ln(\sinh(\alpha\sigma))$ vs $\ln(\dot{\varepsilon})$ and $\ln(\sinh(\alpha\sigma))$ vs $\frac{1}{T}$ gives n and Q with linear regression. Finally, the constant $\ln(A)$ is the average of the intercept of $\ln(\sinh(\alpha\sigma))$ vs $\ln(\dot{\varepsilon})$ from different temperatures.

The Johnson-Cook (JC) empirical model has been used to predict the flow behavior of different materials and used in finite element simulations due to its high accuracy and simple form (T. Li, 2019). The model contains only five constants and is expressed as follows:

$$\sigma = (A + B\varepsilon^n)(1 + C_1 ln\dot{\varepsilon^*})(1 - T^{*m}) \tag{1.26}$$

Where $\sigma\ is$ the flow stress, ε is the strain and $\dot{\varepsilon^*}$ is the dimensionless strain rate from $\dot{\varepsilon}^* = \dot{\varepsilon}/\dot{\varepsilon}_{ref}$. $\dot{\varepsilon}_{ref}$ is the reference strain rate and corresponds to the lowest strain rate of the study interval. $T^* = \left(T - T_{ref}\right)/\left(T_m - T_{ref}\right)$ is the relative temperature, T is the experimental temperature, T_{ref} is the reference temperature (lowest of the study interval), and T_m is the melting temperature of the material. The constants are calculated from experimental data and have the following physical meaning. A is the yield stress at $\dot{\varepsilon}_{ref}$ and T_{ref} and it could be calculated directly from the engineering curve of stress and strain under the reference conditions. B is the material hardening coefficient, n is the material strain hardening index, C_1 is the strain rate sensitivity coefficient, and m is the temperature softening index.

Among the four models described above, H&S and JC are preferred for their simplicity and ease to incorporate in the material data code of a simulation software. However, the Arrhenius constitutive model is of great interest for the calculation of the material constant Q and its theoretical approach. This model is also a better adapted solution if the material shows a great

dynamic softening behaviour under the experimental conditions. It will be relevant to determine which model is most suited for H13 hot work tool steel at forging temperatures (1150 °C to 1260 °C) and strain rates (0.001 s^{-1} to 1 s^{-1}), for comparison and simulation purpose.

1.4 Simulations

The AISI H13 steel is widely used as die in the automotive industry. Thus, many studies on H13 steel including simulation focus on the utilisation of this hot work tool steel as a die instead of a workpiece, which is the application of interest in the current research. In most studies that deal with failure analysis, the flow stress is low or non-existent which is not representative of the industrial process (Kchaou, 2010; Marashi, Yakushina, Xirouchakis, Zante, & Foster, 2017; X. X. Zhang, 2012). However, Zhou and Blackketter (2012) conducted relevant studies, in collaboration with Finkl Steel - Chicago, on simulation of centerline defect closure in large open die forgings.

Zhou (2012) constructed numerical models in Forge® using data from footage of the actual process and Gleeble 3500 compression tests. The series of hot compression tests covered strain rate conditions of 0.01 to 0.13 s^{-1} and temperature conditions of 1230 to 1270 °C. He studied variables such reduction per pass (10 to 20%), feed ratio (10 to 60% overlap between each bite) and initial cooling time for an industrial case concerning large H13 steel ingots forged into bars. He measured the results by comparing the effective strain vs. billet length curves at different conditions. For the reduction, the author observed that the highest ratio resulted in higher centerline effective strain. Therefore the reduction amount should be set as high as possible, but according to Forge® computations, 20% was the highest value that did not exceeded the theoretical press capacity. For the feed ratio, 20% overlap was judged as the best scenario, taking into consideration. Lastly, the diagonally cogging process was found to have little impact on the centerline strain accumulation as long as the void closure is achieved during the previous cogging steps.

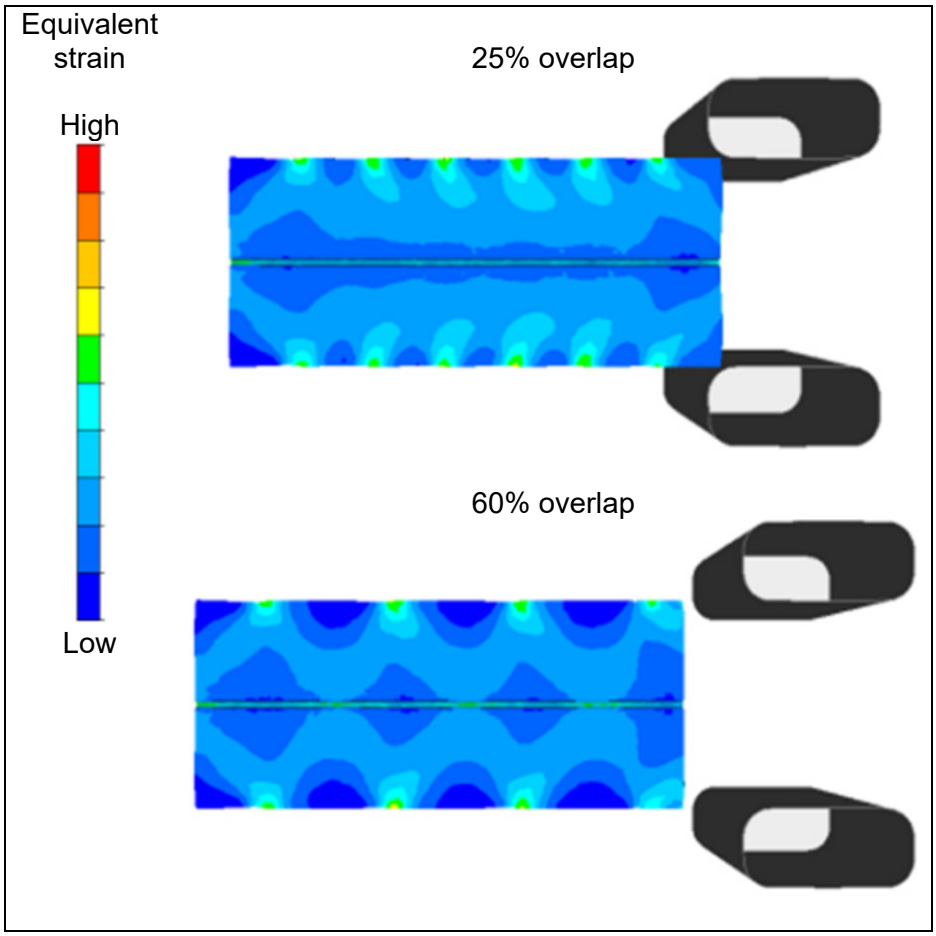

Figure 1.10 Effect of die overlap on equivalent strain during cogging of a H13 bar
Adapted from Zhou (2012)

Blackketter (2012) performed real scale single blow operation of a H13 test piece with a 25 mm drilled hole in the longitudinal axis, as shown in Figure 1.11. The analysis of cut slices showed no voids in high strain areas as predicted by simulation results. The critical effective strain value for closure of the hole was calculated at 0.6.

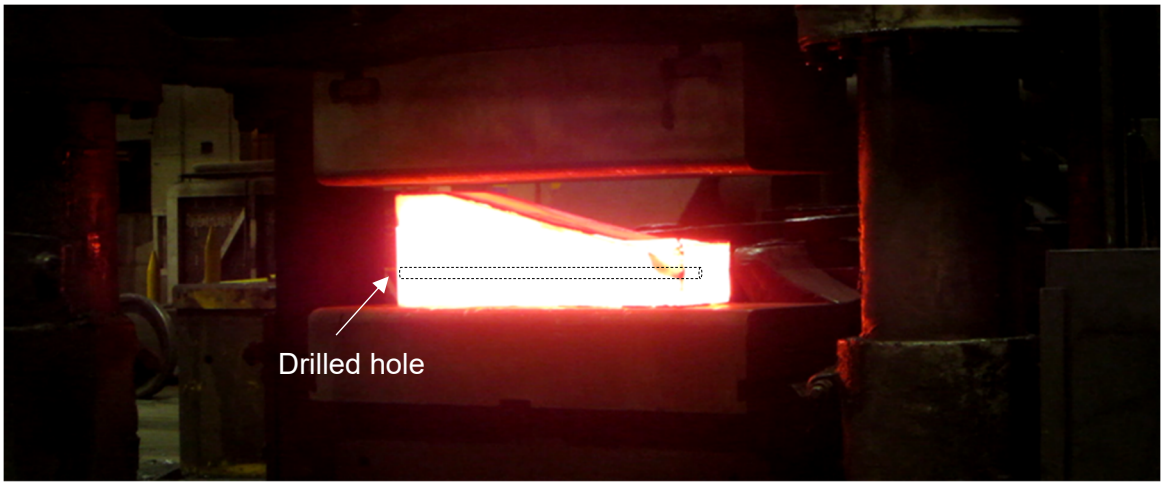

Figure 1.11 Single blow operation of a H13 test piece with a 25 mm drilled hole in the longitudinal axis
Adapted from Blackketter (2012)

Zhou and Blackketter studies demonstrated that finite element simulation is a fast and low-cost solution to evaluate the state during the actual forging procedure. Their simulations show opportunities in reduction ratio, die overlap, and critical effective strain value that could be simulated with Sorel's capacity and products. In addition, their studies concentrated on square shaped forgings, while Sorel's concern is for round shaped forgings.

To attempt new forging scenarios with a reliable FE model, the simulation must consider a multitude of physical phenomena during metal working, including heat transfer, stress-strain state, and phase or microstructural transformation, as shown in Figure 1.12 (Guo, 2018). This requires a wide range of material data to achieve reliable results. In his article, the author highlights the principal material inputs in a simulation software:

a) Phase transformation kinetics

TTT (time temperature transformation) and CCT (continuous cooling transformation) diagrams help predicting phase transformations as temperature decreases. This is not included in the present study, considering that the forging temperature never goes under the critical temperature of austenite transformation.

b) Property per phase

Softwares, such Thermo-Calc and JMATPRO®, calculate physical and thermophysical properties such thermal conductivity, heat capacity, Young's modulus, Poisson's ratio and thermal expansion ratio. With this information, calculations of strengthening mechanisms can be achieved for a specific alloy. These properties must be calculated for the corresponding grain size. It must be also noted that some of the predictions made by FactSage software need to be validated experimentally to ensure further reliability.

c) Stress-strain (flow) curves

Per Simsir (2018) and Guo (2018) these curves are the most important data input for simulation of forming processes. They are established experimentally for different levels of stress, strain, strain rate and temperature. Models are developed as described in the previous section.

d) Properties over a heating / cooling cycle

Hot open die forging usually consists of heating and cooling sequences and the material properties can be different between the two. It is therefore important to input the material data for the complete thermal cycle.

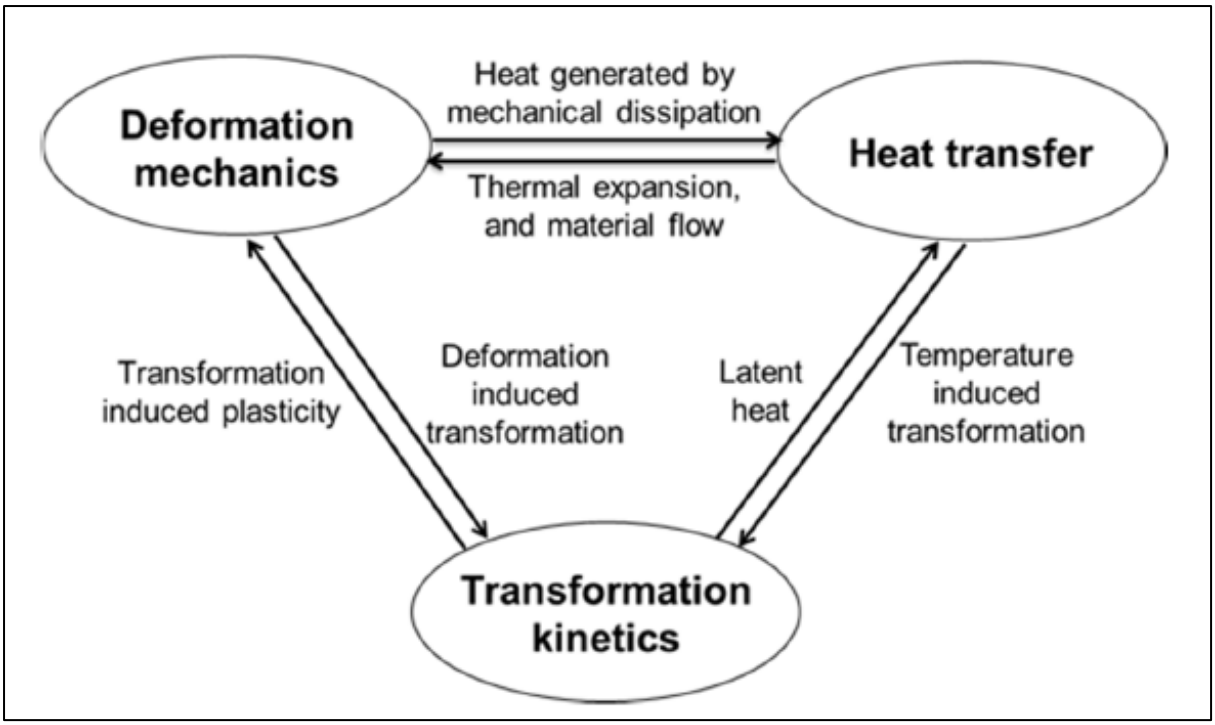

Figure 1.12 Interactions between three main physical phenomena in materials processing Taken from Guo (2018)

The chemical composition has an important impact on the material data above (J. Li, 2014 ; Ning, 2017 ; H. Wang, 2017). Finkl Steel – Sorel produces H13 with narrow aims between the vast AISI chemical composition requirements. Thus, it is relevant to calculate the properties and perform experimental tests with samples of an alloy composition that is of the type used by Finkl Steel, for the purpose of implementation in a simulation software.

1.5 H13 Hot Working Tool Steel

H13 is a hot work tool steel used as extrusion and forging dies in metal forming industries. It is characterized by its high thermal stability and wear resistance due to its high content of alloying elements and second phase particles. H13 alloy mainly serves as a hot work tool steel. Some typical applications are:

- Tooling for Aluminum die casting;
- Aluminum and Magnesium extrusion dies;

- Die inserts and forging dies;
- Plastic mold dies;
- Cores, sleeves and slides.

Equivalent appellations of AISI H13 are DIN 1.2344 and EN X40CrMoV5-1. Its commercial brand at Finkl Steel – Sorel is Finkl DC®. Its typical chemical analysis, as per ASTM A681 Standard Specification for Tool Steel Alloy, as well as the FINKL DC® composition, is presented in Table 1.1. This alloy also contains a non-negligible amount of Ni, Al and Cu.

Table 1.1 Typical chemical requirements for AISI H13 and FINKL DC® (%wt)

Source	**C**	**Mn**	**Si**	**Cr**	**Mo**	**V**
ASTM A681	0.32-0.45	0.20-0.60	0.80-1.25	4.75-5.50	1.10-1.75	0.80-1.20
FINKL DC®	0.38	0.35	1.00	5.25	1.50	1.00

A particularity of hot working tool steel alloys is a high content of carbides forming elements: chromium, molybdenum and vanadium (Avner, 1964). The dispersion of hard carbides particles, especially Cr and V, and the overall hardness of the steel grants it a high wear resistance. These carbides and its content of elements stabilizing austenite phase, Mn and Ni, also makes this steel hardenable when air cooled. H13 has greater corrosion resistance than P20, but lower than stainless steels which contain more than 11% of Cr. However, 5% of Cr is enough to give a good strength at high temperature.

1.5.1 Carbides in H13

Carbides are important as a second phase in H13 steel. The type, quantity, size, morphology and distribution of carbides have an important effect on the performance of the steel. They give advantages such high hardenability and abrasive resistance, but they may lower the formability and toughness in specific conditions.

Ning (2017) calculated the approximated equilibrium solubility temperatures of carbides in H13. He uses equations (1.27) to (1.30) from the Gibbs free energy equations of the chemical

reactions. The equilibrium temperatures for Finkl DC® chemical composition were calculated and are presented in Table 1.2. Only when the temperature is over the equilibrium temperatures o these carbides dissolute. The typical forging temperature of H13 is over 860 °C (H. Wang, Li, Shi, Li, & He, 2017 ; Zhou & Blackketter, 2012) which means that $Cr_{23}C_6$ carbides are most likely dissolved, and MoC, VC and V_8C_7 may be precipitated.

$$ln\left(w[Cr]_{\%}^{23} \cdot w[C]_{\%}^{6}\right)_{\gamma} = 141.05 - \frac{115443.49}{T} \quad (1.27)$$

$$ln(w[V]_{\%} \cdot w[C]_{\%})_{\gamma} = 11.42 - \frac{17926.15}{T} \quad (1.28)$$

$$ln\left(w[V]_{\%} \cdot w[C]_{\%}^{0.875}\right)_{\alpha} = 13.01 - \frac{21510.02}{T} \quad (1.29)$$

$$ln(w[V]_{\%} \cdot w[C]_{\%})_{\gamma} = 15.48 - \frac{21878.5}{T} \quad (1.30)$$

Table 1.2 Calculated equilibrium solubility temperatures of specific carbides in Finkl DC® using Gibbs free energy equations
Adapted from Ning (2017)

Carbides	V_8C_7	MoC	VC	$Cr_{23}C_6$
Equilibrium solubility temperature (°C)	1279	1174	1050	788

Li (2014) and Wang (2017) studied the evolution of carbides in H13. They analysed the microstructure by SEM-EDS to identify the carbide types after different heat treatment process, as shown in Figure 1.13. They highlighted that both thermodynamic and kinetic conditions need to be met for the precipitation and decomposing of carbides and that the experimental result vary from the theoretical calculation depending on the heat treatment conditions. However, from their experiment and thermodynamic calculation, the precipitation and evolution of carbides in H13 is explained as follows:

a) Cast and annealed (Figure 1.13 a) and c))
   - During solidification, the austenite phase forms first in hypereutectoid steel and the solute elements concentrate in the remnant melt. When they are supersaturated, the elements precipitate as secondary phases.

- Increasing the bulk contents of Cr, Mo, V and C thermodynamically promotes the dissolution temperatures of the corresponding carbides and the possibility of the formation of primary carbides.
- The cast and annealed microstructure shows dendritic segregation and secondary phases in interdendritic spaces: a majority of V-rich and a minority of Mo-rich primary complex carbides. This proportion is explained because Mo has a lower affinity with C in comparison to V. No Cr carbides were observed, because of its even lower thermodynamic affinity with C and better diffusing ability.

b) Forged and annealed (Figure 1.13 b) and d))

- At forging temperature of 950 °C to 1050 °C, there is partial dissolution of Mo-rich and V-rich primary carbides.
- Forging broke and scattered a large amount of primary carbides. The forged and annealed microstructure shows scattered and smaller Mo-rich and V-rich carbides.

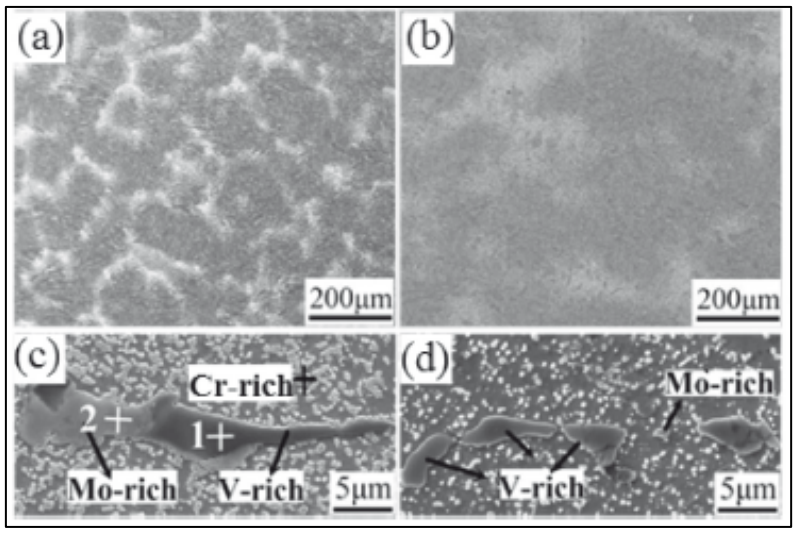

Figure 1.13 SEM observation of carbides, (a) and (c) cast and annealed, (b) and (d) forged and annealed
Taken from J. Li (2014)

With the objective to reduce the segregation and primary carbide size, Khan (2018) studied the effect of soaking ingots before forming bearing steel. According to the author, the degree of homogenization achieved during soaking depends on several factors, including the soaking temperature and time, dendritic arm spacing, the diffusion coefficient of the diffusing element,

any chemical inhomogeneity and the area of the ingot. For the bearing steel, soaking for 20h decreases the Cr concentration significantly in interdendritic areas, but not in the dendrite center. This result is due to a steeper concentration gradient close to interdendritic areas and hence a higher diffusion rate. Long isothermal holding tests that are conducted in the current study can help to understand the critical conditions required to promote diffusion and dissolution of carbides in H13 and reduce the segregation and carbide size before forging operation.

ESR (Electro Slag Refining) conversion of air melt steel ingots reduces the size and amount of inclusions (Liu et al., 2012). For H13, this process is especially useful for controlling large linear V, Cr and Mo carbides distributed at grain boundaries. However, this additional process adds important production costs.

CHAPTER 2 INDUSTRIAL PROCESS ANALYSIS

2.1 Industrial Process

The production process of a H13 bar differs from factory to factory. This section describes the general process at Finkl Steel – Sorel.

2.1.1 Casting

The smelter first melts steel scrap in an electric arc furnace. Then, the metal is poured in a ladle that is then brought to a station where alloying elements are added and another station for vacuum degassing. Then, the steel is bottom poured in fluted ingots of 1067 mm or 1600 mm diameter at the casting temperature. The smaller mold is used when the final bars produced have a diameter up to 559 mm.

2.1.2 Forging

Cast ingots are reheated in a gas furnace at least 7 hours for the smallest ingot, at a temperature of 1260 ± 25 °C. Then, they are forged with a 5000 T or a 2000 T hydraulic press equipped with flat dies and reheated 3 to 7 times. The process varies and is determined according to the final diameter of the bars. A minimum forging reduction ratio needs to be reached in function of customer specification. The general process is:

1. Bloom;
2. Upset;
3. FM;
4. Cog (square shape);
5. Cut in 2 to 4 subpieces;
6. Cog (octagon shape);
7. Cog (round shape).

Sensors give live data for many parameters on both presses, including principal cylinder pressure (N/mm^2), upper die position (mm), press speed (mm/s), manipulator position (mm) and manipulator rotation (°).

2.1.3 Post Forging Steps

After the forging process, the steps depend of the needs of the customer. This section describes typical operations.

2.1.3.1 Heat treating

The product is provided in the anneal condition since further machining will have to be perform by customer before final hardening heat treatment.

The primary purpose of the annealing is to soften the steel to maximum 223 HBW and transform the microstructure in stable ferrite with finely distributed spheroidal carbides. This state of the material eases the machining of the product. Quenching is performed to harden the steel and is achieved by rapidly cooling the austenitized part. H13 is hardened to improve its wear resistance when used as a hot working tool.

2.1.3.2 Machining

Bars are centered with a horizontal boring machine and rough turned with large engine lathes to a surface finish of 250 RMS. Sections of the bars can be saw cut and sent to the metallurgical laboratory for testing. Tensile, fracture, micro-cleanliness, microstructure, grain size and hardness tests can be performed.

2.1.3.3 Inspection

The last step before packaging and shipping is inspection of the products. Hardness is measured on the surface at five locations along the length with daily calibrated equipment. A portable device using the dynamic rebound testing method according to Leeb or a static workstation using the Brinell indentation method are used. Then, 100% of the volume of the bars is inspected by the contact ultrasonic method using a 25.4mm probe. This reveals internal defects on a distance-amplitude graph (A-Scan) using a frequency of 2.25 MHz. A reference curve (Distance Amplitude Curve, D.A.C.) calibrated on a 6.35 mm flat bottom holed block is used to evaluate the size of the flaws. Finally, the geometric dimensions of the bars (length and diameter) are measured precisely to make sure that they respect the customer's specification.

2.2 H13 Forging Process Analysis

During the period of May to August 2018, multiple bars of H13 were produced and inspected by the contact ultrasonic method. As illustrated in Figure 2.1, in the sample taken for this study, 30% showed intermittent clusters of porosities along the centerline, conducting to the rejection of a section of the length. Figure 2.2 shows examples of the voids observed at the centerline of the bars, on a transversal cut.

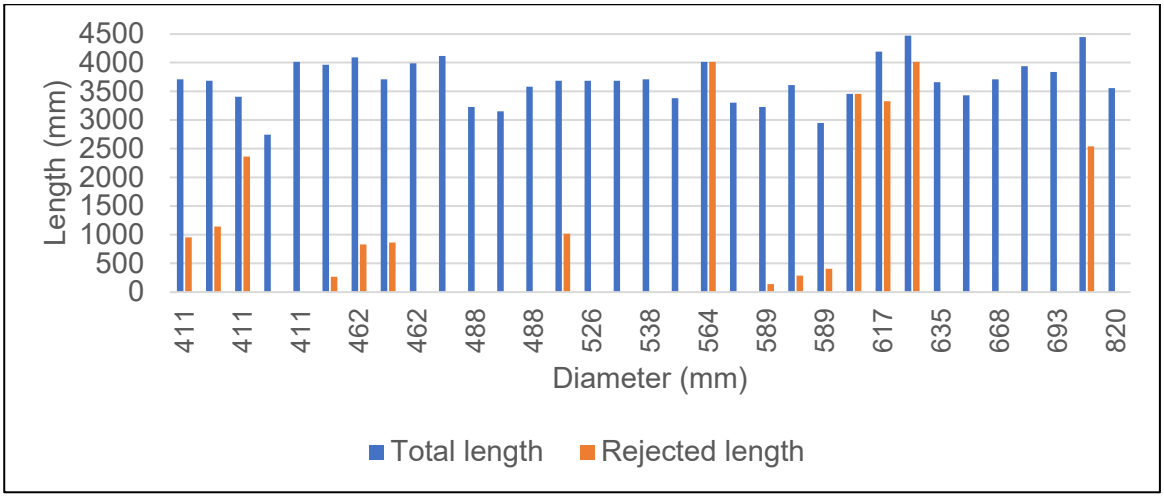

Figure 2.1 Total length and rejected length of the H13 bars forged from May to

August 2018

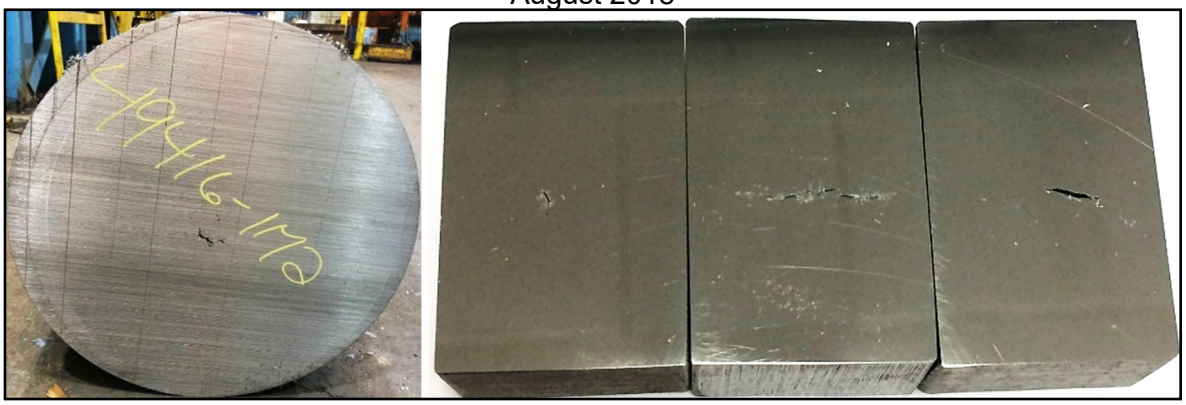

Figure 2.2 Porosities observed at the centerline of H13 bars on a transverse cut

A few available variables and controlled parameters of the forging process were analysed to identify the cause of the defects. The soaking times, press times, number of forging steps, reduction rates per step and total reduction rates were collected for the bars with and without defects. The soaking times exhibit great variability, with 38% before cutting in subpieces and 30% for the final steps. The difference is due to the inventory in the furnaces and the press schedule. The press times (including travel time to the press) also vary of 25%, mainly because of the skills and rapidity of the crane and press operators. The number of forging steps and reduction rates were dependant of the final forging size. In conclusion, even with the high variability of the process, no direct cause could be identified from this data. No tendency could be confirmed with this small sample of bars.

CHAPTER 3 DEFINITION OF THE PROBLEMATIC

During the summer of 2018, Sorel facility of Finkl Steel Co. produced H13 bars, which was a new product to them. Considering the long working experience of the company in forging of high strength steels, no specific problem was foreseen, particularly, that the company had already successfully forged large size cubic shape blocks made of H13. However, they had a 30% rejection rate on the chosen sample of H13 forged bars. While their standard forging procedure produces excellent results for bars of low-alloyed steels such as 4340, important sections of H13 forged bars present small voids along the centerline. The hot forging monitored parameters were analyzed; however, no obvious cause was identified. Also, as defined in the literature review, the presence of hydrogen “flakes” was rejected, because the shape is round and H content is of approximately 1 ppm as per the certified chemical composition. However, the defects were located in the centerline and mainly in top of ingots. Their position matches with the initial cavity segregation areas in cast ingots. Therefore, they can be unclosed porosities, voids generated by secondary tensile stresses or “burst”. These types of defects can be of mechanical, metallurgical, or both natures.

The literature review highlights important characteristics of the material that influences the stress distribution and effectiveness of consolidation during deformation. From a microstructural perspective, grain size and precipitates influence the ductility of the material. From a mechanical perspective, plastic deformation and triaxial compressive stresses are important factors that influence porosity closure. Furthermore, as the deformation temperature and strain rate strongly affect the stress state during deformation; their impact on high temperature deformation must be quantified.

The objective of this project is to study the influence of hot deformation parameters on the flow behavior and microstructure evolution of H13 steel in the centerline of forgings. To do so, the study focuses on the development of a representative material model. Specifically, the changes in grain growth, dissolution of carbides and stress-strain curves stages are analysed. This research aims to provide a material model and process control limits by means of experimental tests that give information on the forging conditions at the centerline of a round shape workpiece. From the literature search, this addresses gaps in the characterisation of H13, specifically in the forging temperatures interval. As many studies focus on the heat

treatment or tooling applications of H13 (Lin, 2016 ; H. Wang et al., 2017), few provide data at temperatures as high as the hot forming range (1150-1260°C). In addition, the chemical composition has an important impact on the properties (J. Li, 2014 ; Ning, 2017 ; H. Wang et al., 2017). Finkl Steel produces H13 with narrow aims between the vast AISI chemical composition requirements. Thus, it is relevant to perform experimental tests with samples of an alloy composition that is of the type used by Finkl Steel.

The objectives and hypotheses to verify are summarized below.

3.1 Objectives of the study:

- Characterise the kinetics of grain growth and carbide dissolution in H13 hot work tool steel during isothermal holding tests at forging temperatures.
- Quantify the impact of different deformation conditions (temperature, strain rate) on microstructure evolution at the centerline of a forging and stress-strain curves stages.
- Develop H13 constitutive model of stress-strain curves from hot compression tests data for the purpose of implementation in a simulation software.

3.2 Hypothesis to verify:

- The high content of carbides forming elements (Cr, Mo and V) in H13 has an impact on the formability of this alloy at the forging conditions of Finkl Steel.
- Grain growth may occur when soaking H13 alloy at forging temperatures.
- Hot compression tests provide data for accurate modelling of stress strain curves under specific conditions (chemical composition, temperature, strain rate).

CHAPTER 4 THERMOMECHANICAL STUDY OF H13

This chapter presents the calculations and experimental tests conducted to characterize H13 tool steel in hot forging conditions. First, theoretical thermodynamical properties and stress strain curves are calculated using Thermo-Calc and JMATPRO® softwares. Then, isothermal holding experiments and hot compression tests are conducted with H13 samples to quantify the material behavior at high temperature and under deformation.

4.1 Theoretical Thermodynamical Properties

The thermodynamical properties were calculated using Thermo-Calc and JMATPRO®. Both are a software package which calculate a large range of material properties. Thermo-Calc was used to calculate the phases in equilibrium at different temperatures. This is useful to estimate if phase transformation will occur and whether precipitates have a role to play during the deformation process (Mukherjee, Prahl, & Bleck, 2010). Then, the theoretical stress strain curves were calculated with JMATPRO® to compare with the experimental curves calculated from the hot compressive tests with Gleeble.

4.1.1 Methodology

The input in each database was the actual chemical composition of the material prepared for the hot compression tests, as presented in Table 4.1.

Table 4.1 Chemical composition of tested steel (%wt)

C	Mn	Si	Ni	Cr	Mo	V	Cu	Al
0.37	0.41	0.98	0.14	5.24	1.3	0.94	0.14	0.009

4.1.2 Results

The results of the phases in equilibrium and the stress strain curves are presented.

4.1.2.4 Phases in Equilibrium

The phases in equilibrium in the range from 700 °C to 1600 °C were calculated with Thermo-Calc and are illustrated in Figure 4.1. Key temperatures are presented in Table 4.2.

The results show that the steel is fully austenitic from 1342 °C to 1158 °C, at equilibrium. However, these critical temperatures will differ at the time of forging. Segregation of elements in different areas of the ingot and a short holding time will affect the phases in presence. These results give an estimation of the properties.

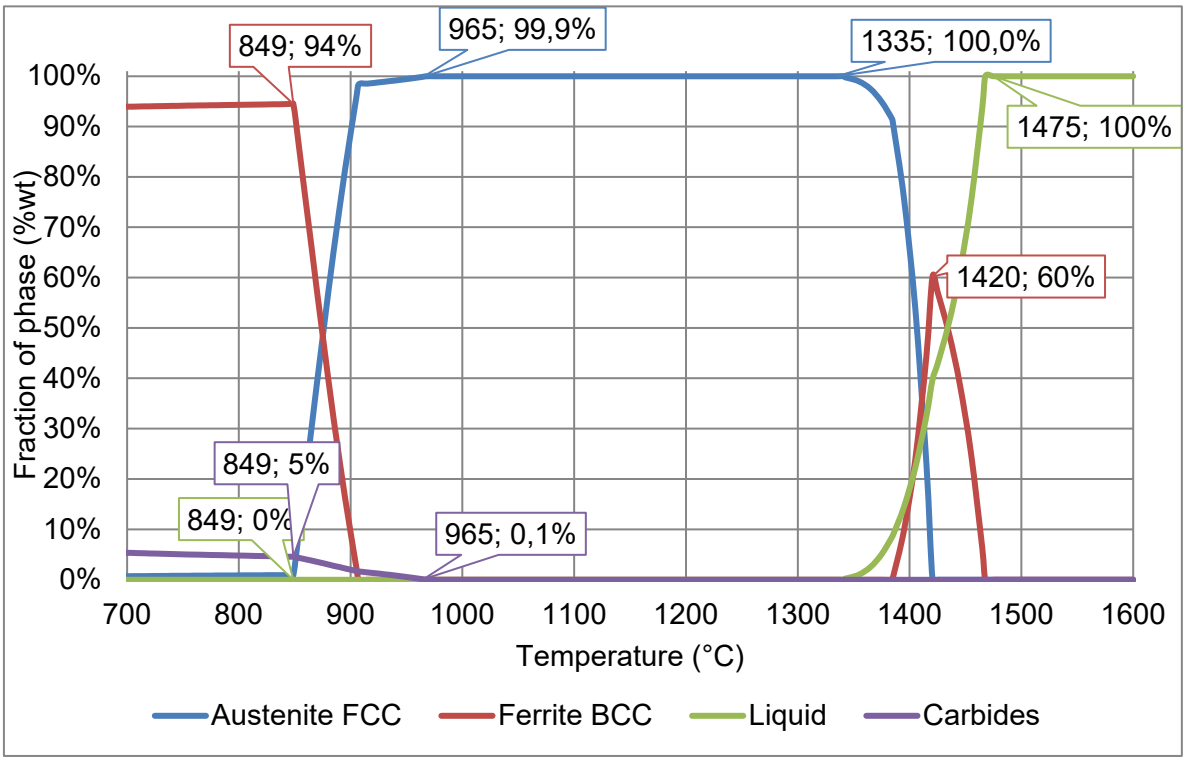

Figure 4.1 Equilibrium phases in the range from 700 °C to 1600 °C
Calculated with Thermo-Calc

Table 4.2 Critical temperatures of equilibrium phases Calculated with Thermo-Calc

Property	**Temperature (°C)**
Liquidus, lowest temperature for 100% liquid	1475
Solidus, highest temperature for 100% solid	1335
Delta ferrite start	1465
Delta ferrite end	1385
Austenite start	1420
Highest temperature for 100% austenitic	1335
Lowest temperature for 100% austenitic	1158
Austenite end	849
Carbides start	965
Alpha ferrite start	925

4.1.2.5 Calculated Stress Strain Curves with JMATPRO®

The stress-strain curves calculated with JMATPRO® are presented in Figure 4.2. As expected, the stress increases with increasing strain rate, and with decreasing temperature. In addition, they show a very short transition stage before the softening stage. The softening rate is constant for each curve.

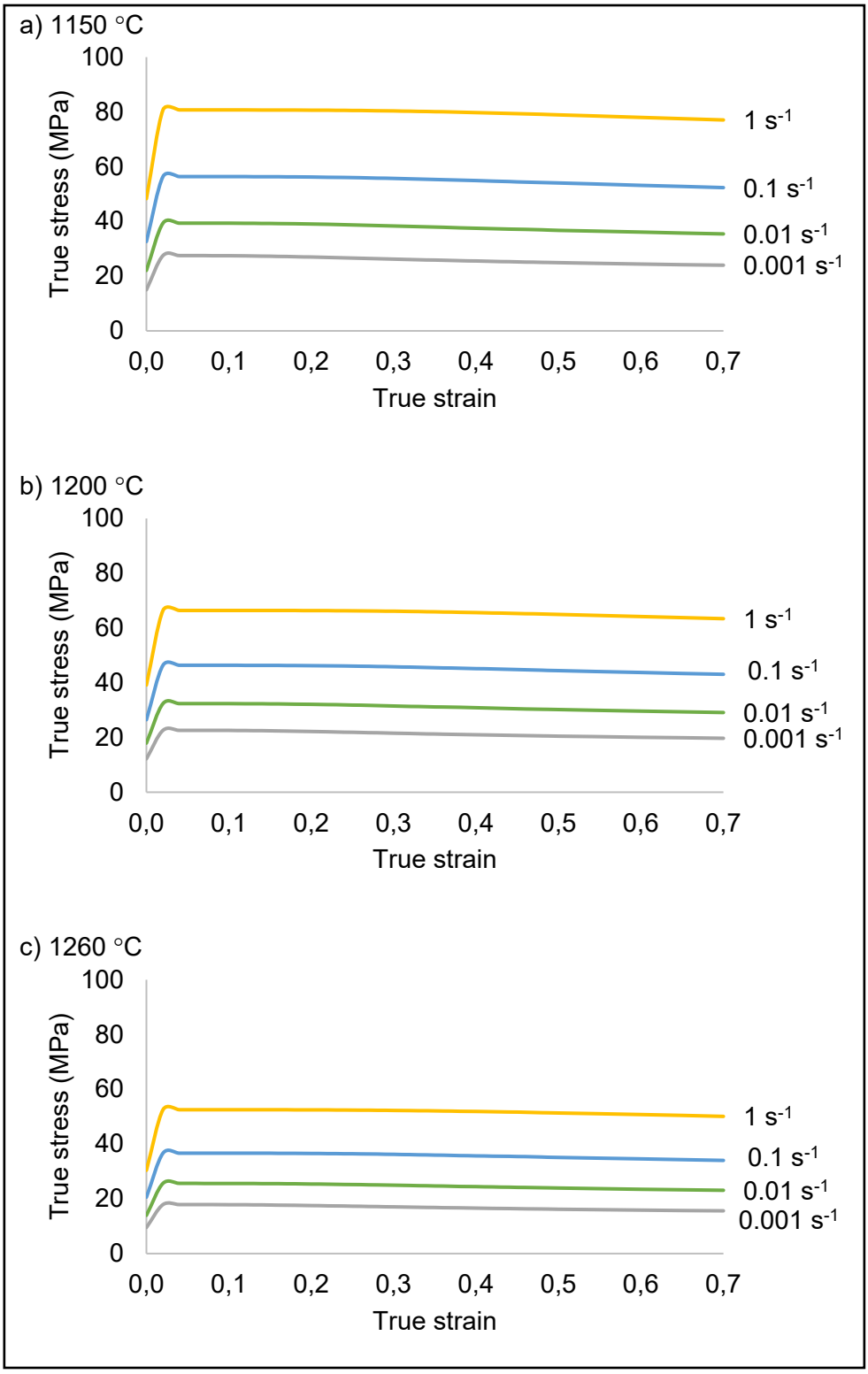

Figure 4.2 Stress-strain curves calculated with JMATPRO® at different strain rates and temperatures, (a) 1150 °C (b) 1200 °C and (c) 1260 °C

4.1.3 Discussion

The critical temperatures calculated with Thermo-Calc indicate that dynamic transformations may occur in the hot forging temperature range. During forging, the piece undergoes heating and cooling cycles (soaking in the furnace, cooling during transportation to the press, adiabatic heating and cooling during deformation). In this range of temperature, near the target of 1260 °C and below, the conditions are near the start of the austenitic (FCC) to carbide and ferritic transformation at 1158 °C. This could result in loss of ductility if the temperature drops and BCC phase transformation starts (« Open Die Forging », 1988).

The stress strain curves could be calculated with JMATPRO®. They show an increasing strain hardening rate with strain rate. At a strain of 0.04, the softening stage starts for all conditions, with the stress reducing at the same rate. The softening stage starts with a higher rate on a small range of deformation levels. According to Dieter (1988), the initiation of softening is characterized by deformation where strengthening mechanisms become unstable and the rate of softening exceeds the rate of area increase. The instability in compression is then related to the strain rate sensitivity (m): the greater the rate sensitivity, the sooner flow localization is initiated. The model used in JMATPRO® is unknown, but the rate of softening is calculated according to a set of parameters that can include a fixed strain rate sensitivity for all conditions, which is an approximation as the strain rate sensitivity increase with temperature. The experimental curves calculated in the next section give more information on the softening rate.

4.2 Grain Size Evolution and Carbide Dissolution

When holding H13 at high temperature, grain growth will occur. Meanwhile, precipitates dissolution takes place at different temperatures. For example, Chromium carbides dissolve over 788 °C while Vanadium carbides dissolve around 1279 °C (V_8C_7) and 1174 °C (VC), and Molybdenum carbides dissolve around 1050 °C (as per section 2.5.2). Isothermal holding tests were performed to characterize the behaviour of H13 steel when held at high temperature.

4.2.1 Methodology

To examine the grain growth behavior, kinetics under isothermal austenitization process and dissolution temperature of carbides, heat treatments at different temperatures (1150 to 1260 °C) and times (300 to 5400 s) were conducted, as defined in table 4.3. For the tests, 10 mm ø x 15 mm samples were prepared from the midradius area of a 406 mm diameter forged and annealed H13 bar. The starting grain size could not be accurately revealed from the as annealed microstructure. Thus, a sample was austenitized at 1150 °C and briefly soaked during 60 s.

A laboratory muffle furnace with ceramic heating plates (Nabertherm) was used. The furnace was programmed, and the samples were put in the furnace when the target soaking temperature was reached. The time started to be monitored when the furnace ramped back to the target temperature. When the soaking time was completed, the sample was taken out of the furnace and air cooled. Then, to reveal the grain size, the samples were cut at half their length to observe the microstructure in the transverse orientation. They were mechanically polished using different SiC papers up to 1200 grit followed by 1µm diamond paste as the final polishing step. The polished samples were then etched for 5 min with Nital 3%. The observations were made with Olympus LEXT OLS4100 laser microscope. Average grain size was measured based on the linear intercept method according to ASTM E112 standard, considering at least 50 grains to ensure representative data. Carbides concentration was evaluated by counting the number of particles per area. An image processing and analysis software (ImageJ) was used for the average grain size and carbides concentration.

Table 4.3 Design of experiment for isothermal holding tests

Process parameter	**Values**
Temperature (°C)	1150; 1175; 1205; 1230; 1260
Holding time (s)	60 (at 1150°C only, starting condition); 300; 900; 1800; 2700; 5400
Cooling	Air

Figure 4.3 Furnace and samples for isothermal holding tests

4.2.2 Results

The results are divided according to the two observed phenomena: grain growth and microstructure evolution.

4.2.2.1 Modeling the Kinetic of Grain Growth

First, the starting conditions need to be determined for the calibration of the model. The initial grain size was determined to be 28 µm, from the sample soaked for 60 s at 1150 °C.

The variation of the grain size with soaking time for different temperatures is shown in Figure 4.4 a). The grain size increased with time as expected, except for 1150 °C for which the grain size was constant at approximately 31 μm, with a standard deviation of 19 μm. As the average grain size increases so does the standard deviation. At 1260 °C with holding times of 2700 s and 5400 s, the error bars overlap; therefore, the average grain sizes are possibly very close to each other at approximately 468 μm. This suggested that the kinetics of grain growth was slower as the holding time increased and that a steady state was almost achieved after 2700 s. The effect of soaking temperature on the average grain size for different soaking times is represented in Figure 4.4 b). Grain growth was faster at higher holding temperatures.

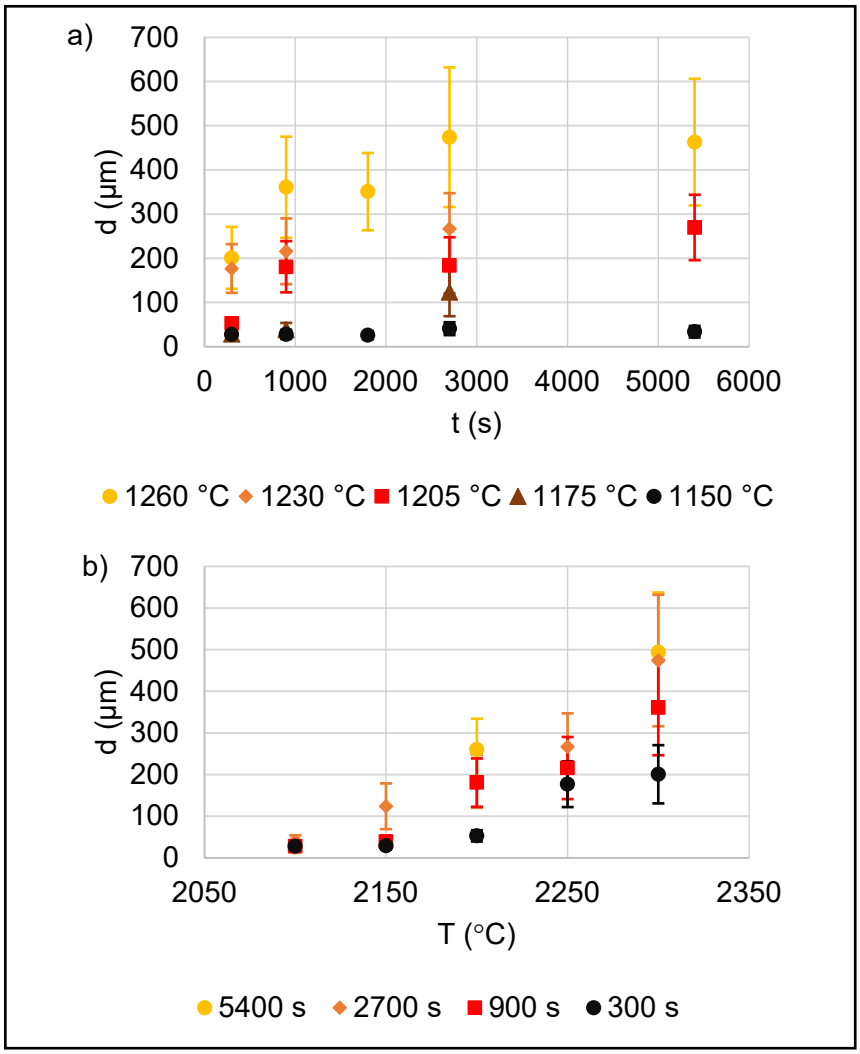

Figure 4.4 Variation of the average grain size after isothermal holding tests with (a) time, at constant temperature and (b) temperature, at constant time

Different models are proposed in the literature to predict the kinetics of austenite grain growth with the holding time and temperature. First, Porter & Easterling (2009a) relation was correlated with the results obtained in the present work. The best results were achieved with calculating the factor K and the grain growth exponent n_g as functions of temperature T (°C). Using the algorithm of non-linear optimisation Solver of Microsoft Excel, the resultant equation for the investigated conditions is:

$$D = (0.39T - 439)t^{(0.00032T - 0.12)} \quad (4.1)$$

Where D is the average grain size (µm) and t is the holding time (s).

In a recent publication, an Arrhenius type constitutive relationship (equation 29) was suggested by Chentouf (2020) for austenite grain growth in a medium carbon steel. The constant and the activation energy were calculated using the algorithm of non-linear optimisation Solver, of Microsoft Excel and the resultant equation is:

$$D = \left[d_0^{2.60} + 5.76 \times 10^{39}\ t\ exp\left(-\frac{1065868}{RT}\right)\right]^{\frac{1}{2.60}} \quad (4.2)$$

Where D is the average grain size (µm), t is the holding time (s), d_0 is the initial average grain size set at 28 µm, 2.60 is the inverse of the time exponent for grain growth m, 5.76×10^{39} is a constant, 1065868 is the activation energy Q (J/mol), R is the universal gas constant (8.314 J/(mol·K)) and T is the austenitizing temperature (K).

Figure 4.5 presents a comparison of the experimental and predicted average grain size with Porter and Chentouf models. The models were quantitatively compared by calculation of the average absolute relative error (Er) between the experimental D_e and predicted D_p grain size:

$$Er = \frac{1}{N}\sum_{i=1}^{N}\left|\frac{D_e^i - D_p^i}{D_e^i}\right| \times 100 \quad (4.3)$$

Among the two models suggested in the literature to predict the kinetics of austenite grain growth in medium carbon steels (Chentouf et al., 2020 ; Porter & Easterling, 2009a) the model of Porter showed the best fit with an average absolute relative error of 24 % and a good representation of the slower kinetics at high temperatures and long holding times. This high error was mostly attributed to the values where almost no grain growth occurred: 1150 °C, 300 s and 900s; 1175 °C, 300 s and 900 s; as well as 1200 °C, 300 s (circled in Figure 4.5). The experimental measurements are much lower than the calculated values. Without these points, the error drops to 6 %. As will be shown in the microstructure analysis below, the above conditions present a completely different kinetics of grain growth because of an important amount of non-dissolved carbides that pin the grain boundaries. Thus, the Porter model appears to be not well adapted for a system with two kinetics.

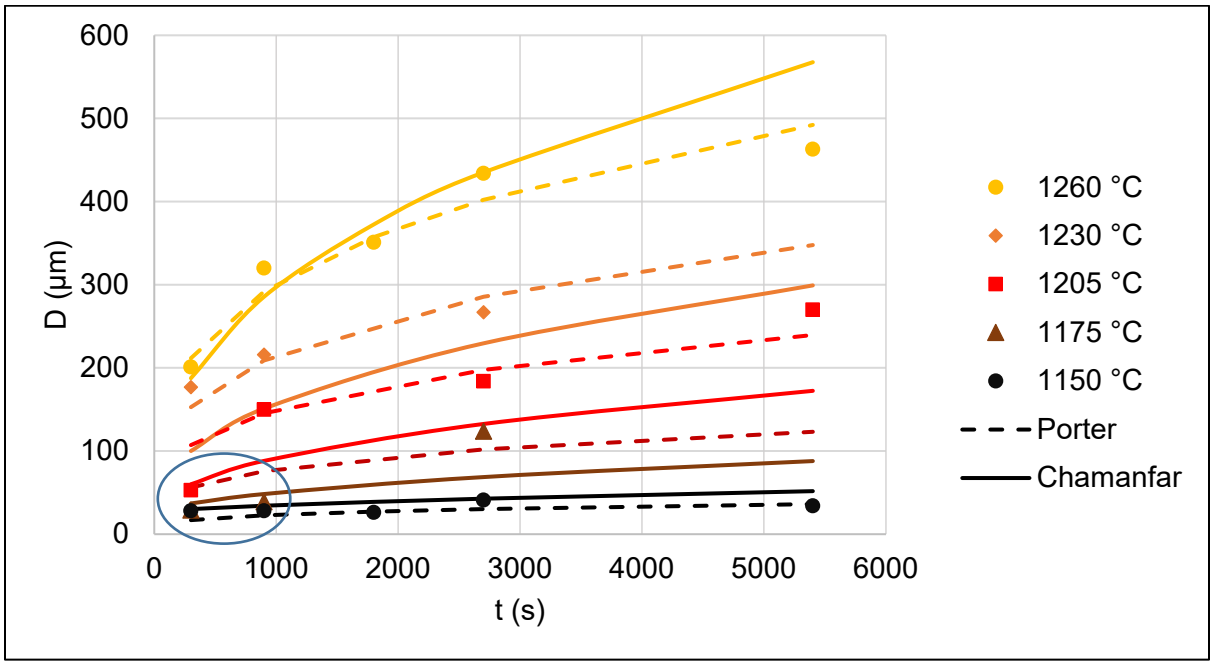

Figure 4.5 Variation of the average grain size after isothermal holding tests and modeling

4.2.2.2 Microstructure Analysis

In addition to the average grain size, the microstructures also provided information on the grain morphology and the carbide dissolution. Figure 4.6 and Figure 4.7 show the microstructure after soaking at different temperatures for 300 s and 2700 s, respectively. These are the observations:

- The quantity of undissolved carbides (black dots) decreased when increasing temperature and time. However, a significantly higher quantity of particles is observed at 1150 °C, 300 s and 2700 s when compared with the other temperatures.
- At 1175 °C after a soaking time of 300 s, the sample revealed a bimodal distribution of grain size.
- At 1230 °C and 1260 °C, the microstructure is characterized by the presence of many hexagonal grains with angles of 120 ° at the triple points and flat boundaries.

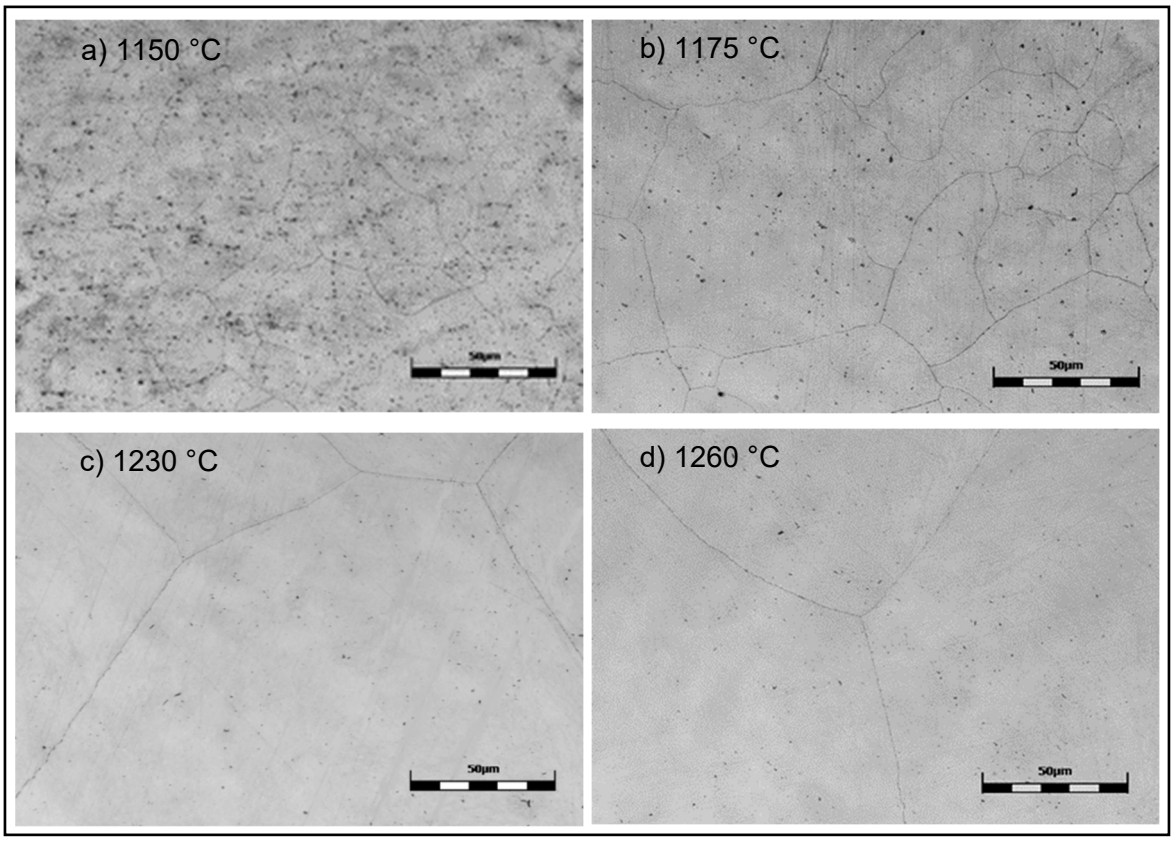

Figure 4.6 Microstructure after soaking 300 s at different temperatures, Nital 3%, laser microscope, 50X

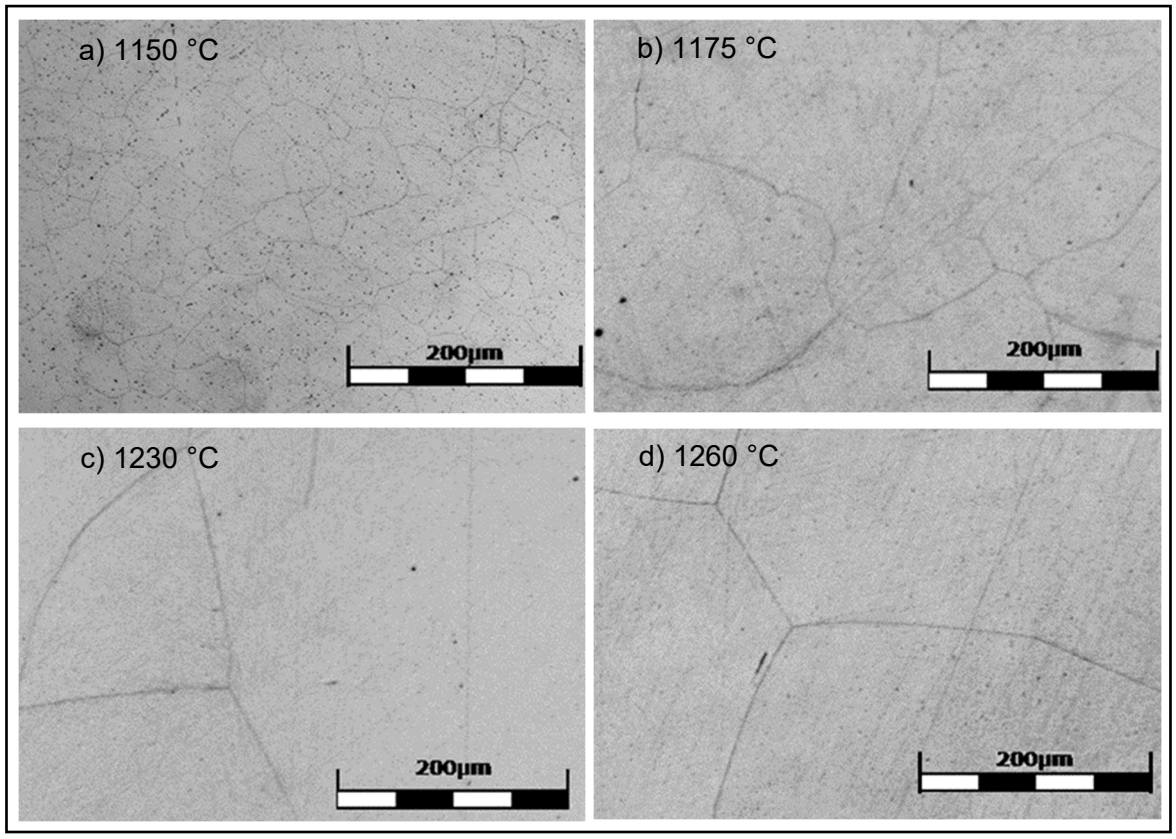

Figure 4.7 Microstructure after soaking 2700 s at different temperatures, Nital 3%, laser microscope, 100X

Afterwards, Scanning Electron Microscopy (SEM) and Energy Dispersive X-ray Spectroscopy (EDS) techniques were used to qualitatively determine the elemental composition of the particles, which corresponded to Cr, Mo or V rich carbides.

Figure 4.8 to 4.12 show results at 1150 °C. Figure 4.8 shows the initial microstructure with a short soaking time of 60 s. Grain boundaries and carbides were clearly observed. From the analysis of elemental maps generated by EDS, the grain boundaries showed a high concentration of Cr rich carbides and some Mo rich carbides were also identified. Through the grains, some Cr, Mo and V rich carbides were also identified. The elemental maps of the sample soaked 300 s shown in Figure 4.10 did not reveal any noticeable presence of carbides at the grain boundaries. However, the Cr map showed a non-uniform distribution of this element. Mo rich and V rich carbides were also observed within the grains. The sample soaked for 2700 s is shown in Figure 4.10. After this much longer soaking time, only randomly

distributed V rich carbides were identified and no presence of Cr or Mo rich regions were detected.

Figure 4.11 and 4.12 show the microstructure of the samples soaked at 1175 °C. After 300 s, a few V rich carbides and large size Mo rich carbides were identified as shown in Figure 4.11. The Cr was uniformly distributed. Then, Figure 4.12 shows a few small V rich carbides and a uniform distribution of Cr and Mo after soaking for 2700 s.

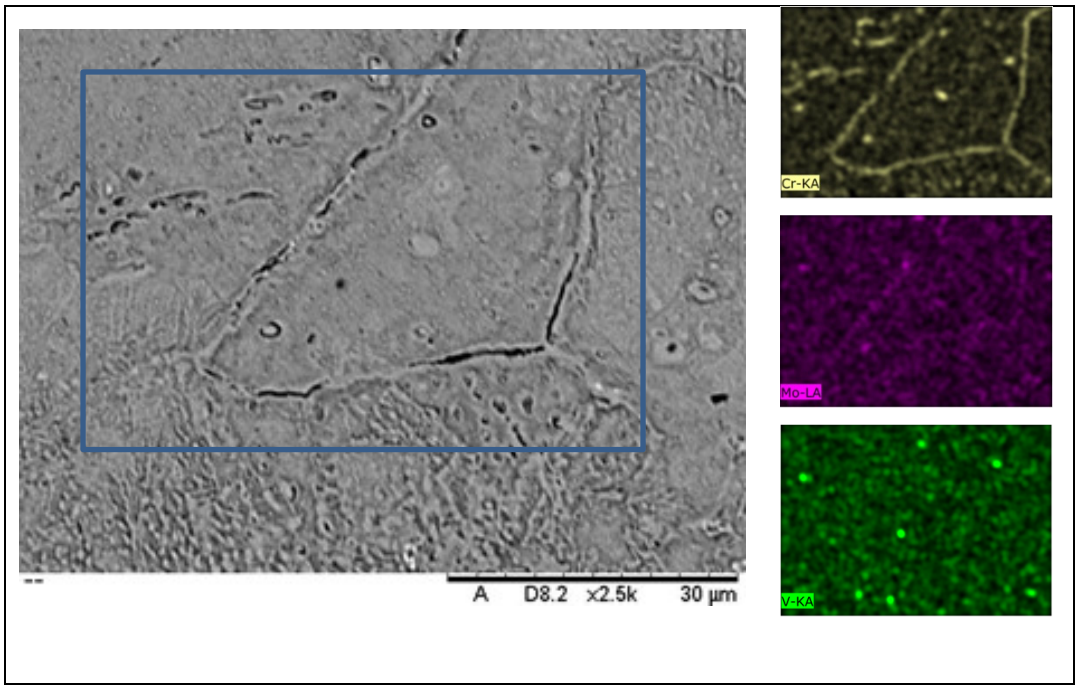

Figure 4.8 Initial microstructure (soaking 60 s at 1150 °C), Nital 3%, SEM images and EDS elemental mapping, 2500X

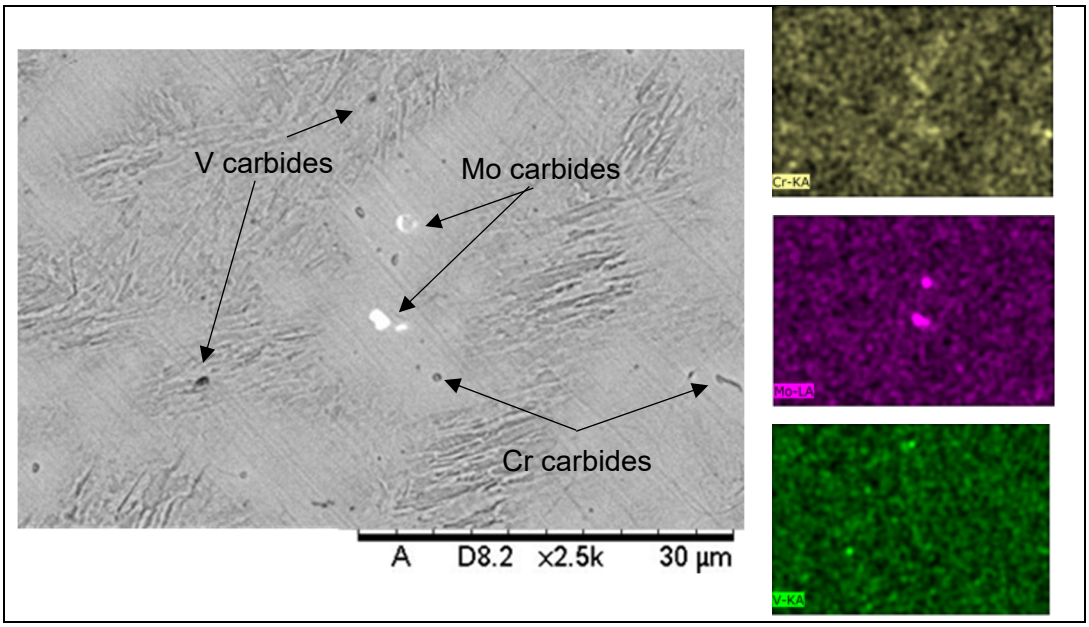

Figure 4.9 Microstructure after soaking 300 s at 1150 °C, Nital 3%, SEM images and EDS elemental mapping, 2500X

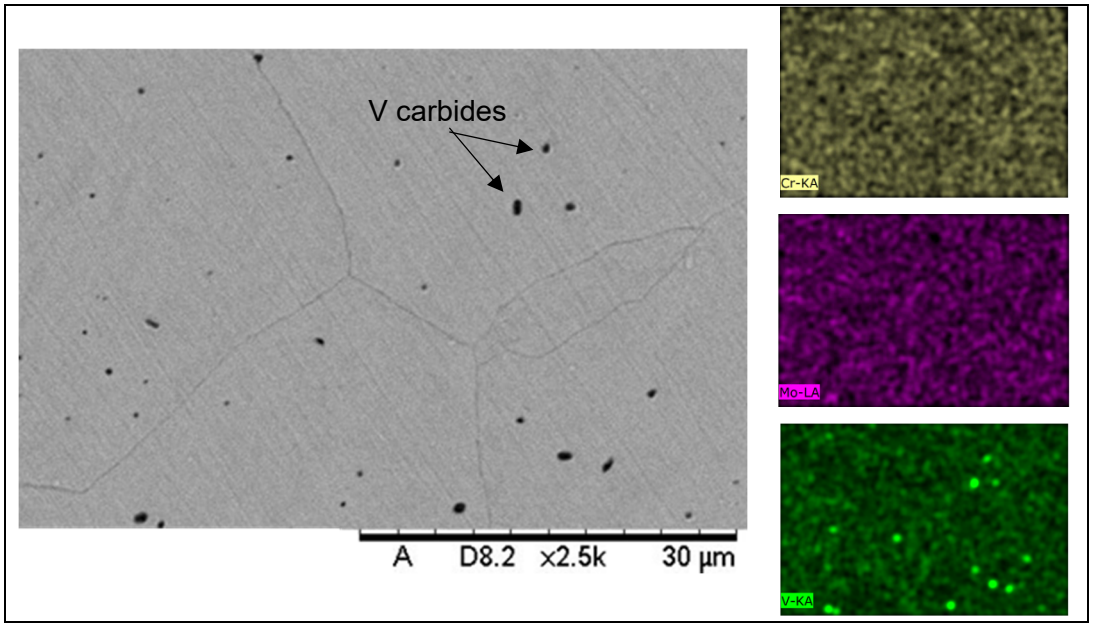

Figure 4.10 Microstructure after soaking 2700 s at 1150 °C, Nital 3%, SEM images and EDS elemental mapping, 2500X

.

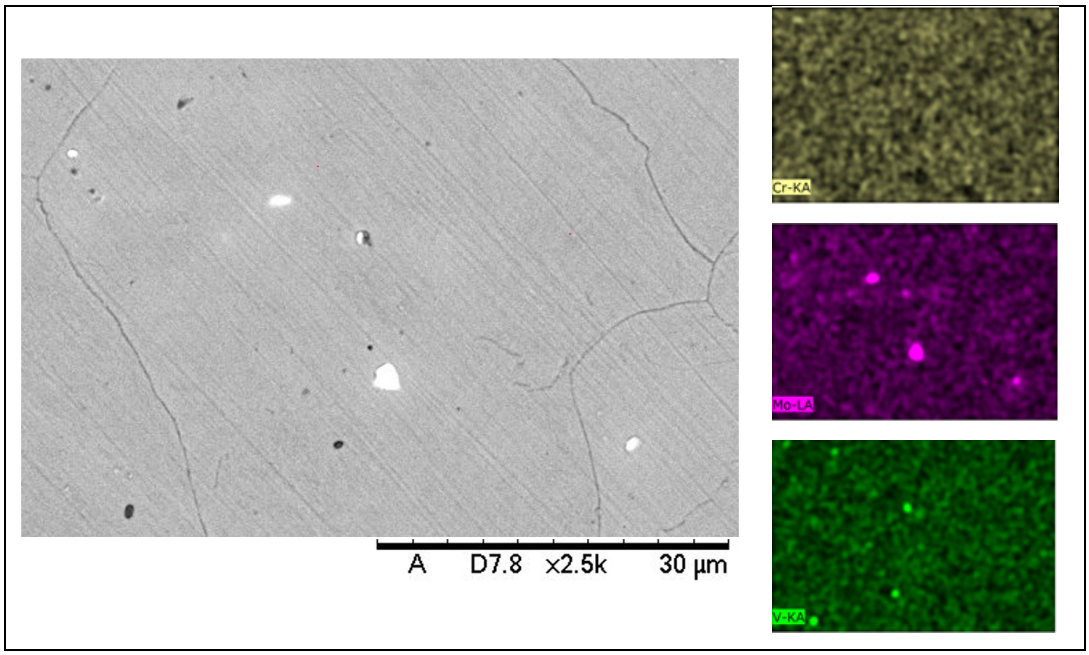

Figure 4.11 Microstructure after soaking 300 s at 1175 °C, Nital 3%, SEM images and EDS elemental mapping, 2500X

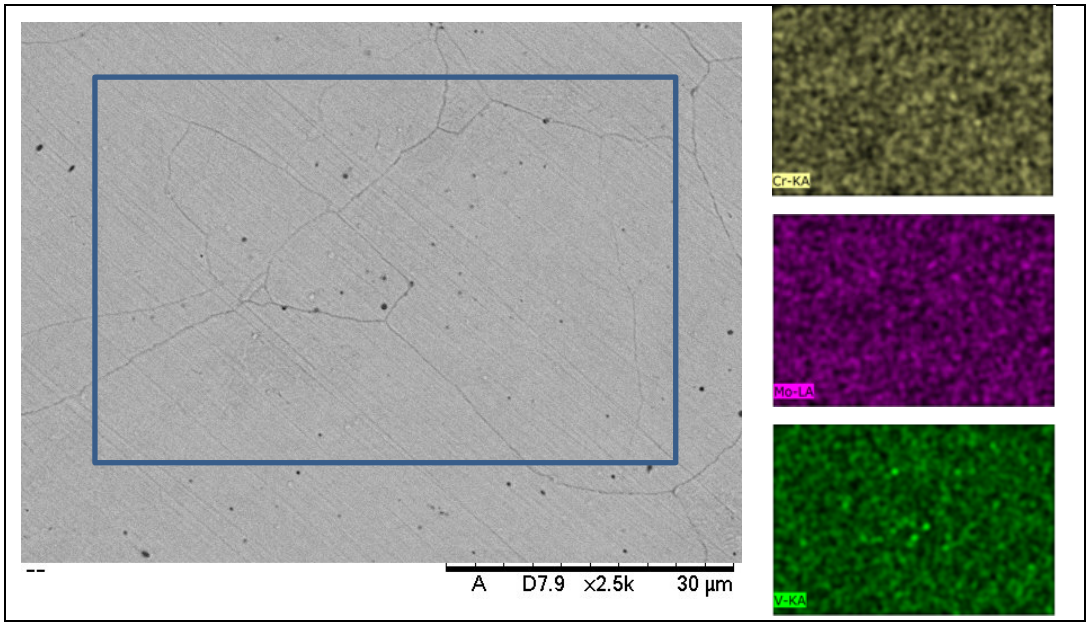

Figure 4.12 Microstructure after soaking 2700 s at 1175 °C, Nital 3%, SEM images and EDS elemental mapping, 2500X

Finally, Figure 4.13 presents the surface density of carbides. The results show that time has a clear effect on the dissolution of carbides. The results also show that, after 2700 s, and for

the 1175 °C to 1260 °C temperature interval a small number of carbides can be seen, while in contrast approximately ten times more carbides were found at 1150 °C.

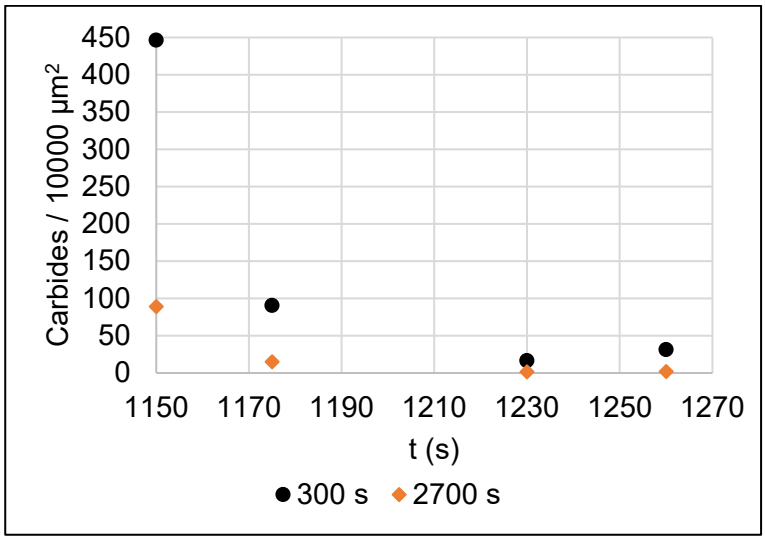

Figure 4.13 Number of carbides per area at different temperatures, for holding times of 300 s and 2700 s

4.2.3 Discussion

The kinetics of grain growth curves reported in Figure 4.5 agrees with the corresponding optical microscope examinations. The microstructures revealed the effect of soaking temperature and time on dissolution of carbides. These restricted the motion of grain boundaries and limited grain growth (Porter & Easterling, 2009b).

The results show that the grains did not grow at 1150 °C, but their size gradually increased from 1175 °C and higher. According to the literature (Porter & Easterling, 2009a), carbides restrict the motion of grain boundaries and limit grain growth. Indeed, the microstructure analysis revealed a high fraction of Mo and V rich carbides at 1150 °C. Those had an important pinning effect on the grains, even after 5400 s when only V rich carbides were identified. From 1175 °C, a sufficient quantity of carbides was dissolved and grain growth could occur. The Cr rich carbides were completely dissolved at each investigated temperature and any of the selected soaking times. Based on the obtained results, the critical holding time for the complete dissolution of the Mo rich carbides is between 1800 s to 2700 s at 1150 °C and 1175

°C, and between 300 s to 900 s at 1205 °C. At 1230 °C and 1260 °C, the thermal energy was sufficient to completely dissolve these carbides at the earliest time. Finally, the V rich carbides were never completely dissolved under the investigated conditions. However, their quantity and size decreased with time and temperature.

The presence of carbides is consistent with the equilibrium solubility temperature of specific carbides calculated from the Gibbs free energy equations (Ning, 2017), as presented in Table 4.4. The critical temperature for dissolution of $Cr_{23}C_6$ was estimated over 788 °C, which confirms why Cr rich carbides were completely dissolved at the investigated temperatures of 1150 °C to 1260 °C. At 1175 °C, a bimodal distribution of the grain size is observed, as seen in Figure 4.6 b), which indicates a transition in the kinetics of grain growth. This coincides with the approximate dissolution temperature of the MoC carbides which is about 1174 °C according to the thermodynamic calculation. Also, in experimental tests with actual samples, carbon and alloy segregation always exists, so the dissolution temperature of carbides will fluctuate in different regions. Finally, as reported by Ning (2017), from 1175 °C and higher, with a sufficient soaking time, the only undissolved precipitate is V_8C_7. The results reported in Figure 4.13 confirm that above 1175 °C and following a minimum holding time, the number of carbides per surface unit is in the same order of magnitude. This suggests that, under these conditions, the observed changes in grain size are related to the impact of temperature on the kinetics of grain growth.

Table 4.4 Calculated equilibrium solubility temperatures of specific carbides in Finkl DC® using Gibbs free energy equations Adapted from Ning (2017)

Carbide type	V_8C_7	MoC	VC	$Cr_{23}C_6$
Temperature (°C)	1279	1174	1050	788

To reach stability, a three-dimensional polycrystalline structure evolves towards equiaxed, hexagonal grains with flat boundaries (Porter & Easterling, 2009a). At 1260 °C after 2700 s, this structure was observed, as shown in Figures 4.6 and 4.7 d). This means that further grain growth could occur, but the kinetics would be slower because the system is close to its stable thermodynamic state. The slower grain growth kinetics was also detected from the calculations of the average grain size as demonstrated by comparing the results at 1260 °C,

after 2700 s and 5400 s soaking times. Considering that the average absolute relative errors of the investigated models are very close, the model extracted from Porter is preferred to depict the slow kinetic at high temperature and long holding time which is the condition encountered in industry.

The isothermal holding tests simulates the conditions during the preheating of large ingots before forging. At 1150 °C, growth is not likely to occur because no such signs were observed during the experiments. At 1260 °C, growth reached a maximum of 463 µm, but the kinetic was slower. Thus, it could be expected that during a multiple-hour holding time, the grain size will achieve a maximum and stable value. Finally, longer holding tests are recommended to confirm the effect of time on the presence and pinning effect of carbides and the maximum grain size achievable.

4.3 Thermomechanical Properties using Hot Compression Tests

To evaluate the state during the actual forging procedure, finite element simulation is a fast and low-cost solution. However, for a reliable FE model, the software must consider a multitude of physical phenomena during metal working, including stress-strain curves (Guo, Lasne, Saunders, & Schillé, 2018). Simulation software such JMATPRO® and FORGE® NxT calculate these curves using the average chemical composition of the material and specific empirical, theoretical, or phenomenological models. However, while the predictions are relatively accurate for most common steels, when it comes to speciality steels such predictions are not always reliable (Simsir & Duran, 2018).

This section aims to model experimental stress strain curves obtained by conducting hot compression tests using the material and the thermomechanical conditions of the actual industrial process. Two types of models are calculated, and then compared with theoretical models. The objective is to determine what model is most suited for H13 at the forging temperatures and strain rates ranges used at Finkl Steel. In addition, compression tests can provide information on the dynamic mechanisms activated during deformation. The shape of the curves and the microstructure of the deformed samples are analysed.

4.3.1 Methodology

In this study, Gleeble 3800, a fully integrated digital closed loop control thermal and mechanical testing system, is used. Cylindrical specimens of 15 mm in height and 10 mm in diameter were prepared. Temperature was measured using a K-type thermocouple spot-welded to the center area of the specimen surface and protected by ceramic tubes. The specimens were heated using a thermo-coupled feedback-controlled AC current. To ensure good conductivity between the specimen and the anvils, graphite foil and nickel paste were added. figure 4.14 shows the schematic of the hot compression tests setup using the Gleeble machine.

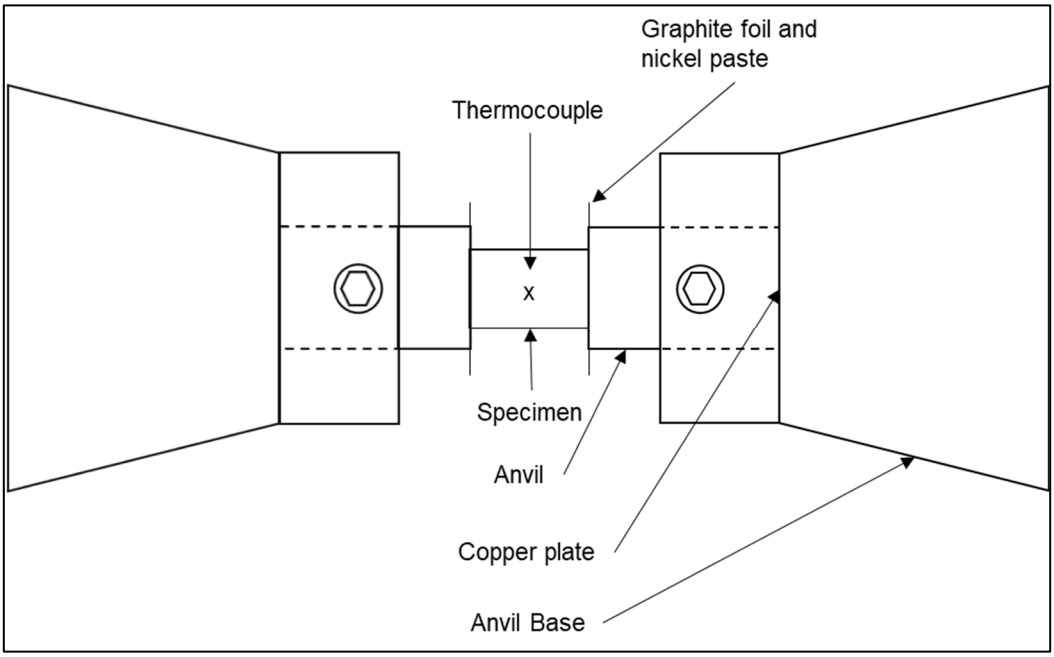

Figure 4.14 Schematic of hot compression tests setup using Gleeble

Table 4.5 presents the experiment design and Figure 4.15 shows the different thermomechanical cycles. The values are explained in the next sections.

Table 4.5 Design of experiment for compression tests with Gleeble

Process parameter	**Values**
Heating rate (°C/s)	2 (fixed)
Holding time (s)	300 (fixed)
Holding temperature (°C)	1260 (fixed)
Temperature (°C)	1150; 1200; 1260
Cooling rate for 1150 °C and 1200 °C tests (°C/s)	2
Holding time for 1150 °C and 1200 °C tests (s)	60
Strain rate (s^{-1})	0.001; 0.01; 0.10; 1.00
Strain ($\Delta A/A_0$)	0.45; 0.65
Atmosphere	Vacuum
Cooling	Air

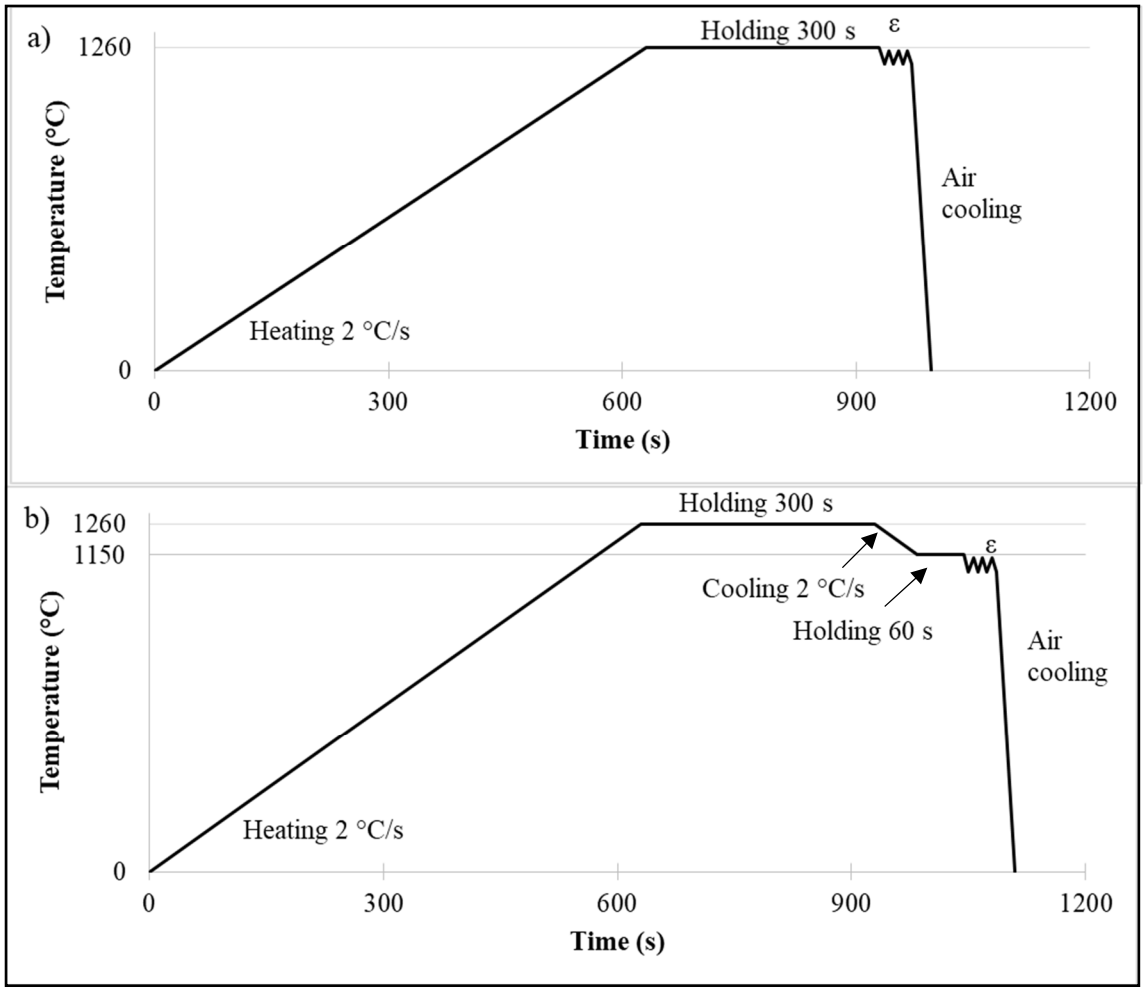

Figure 4.15 Thermomechanical cycles for Gleeble compression tests, (a) 1260 °C, (b) 1150 °C

4.3.1.1 Heating rate

Industrial heating rates are very slow to avoid important temperature gradients that could cause cracking of the very large size pieces. For the present research, a heating rate of 2 °C/s was used. It is slow enough to allow uniform heating of the experimental sample. Similar approaches have been used in previous experiments by Chadha and Shahriari (2015) and Bitterlin and Shahriari (2018).

4.3.1.2 Temperature

Temperature is varied in the experiment to perform simulations at different starting temperatures to evaluate the effect of temperature on the deformation profile. It is also varied to consider the non-uniformity of the industrial furnaces and cooling due to the delay of transportation of the pieces. The latter causes temperature gradients from the surface to the center of a bar and therefore the large size ingot is deformed at different temperatures in different locations.

The actual industrial process for grade H13 is to heat the pieces in a furnace at 1260 ± 15 °C between the forging steps. Trials at Finkl Steel allowed to find that some high chrome and nickel alloys are sensitive to surface cracking. Heating them at 1200 ± 15 °C reduces the risk of creating defects in the material. The holding time is typically 1 hour per inch of diameter. The delay from the furnace to the press varies from 30 s to 300 s, depending on the size of the piece and experience of the operators.

According to the industrial process, the forging temperatures will be 1150 °C, 1200 °C and 1260 °C, when the microstructure is fully austenitic.

4.3.1.3 Strain and strain rate

The strain rate is varied according to the levels attained during the different forging steps. The strain rate is at its maximum value of approximately 0.012 s^{-1} at the beginning of an upset, when the length of the ingot is approximately 2134 mm. Then, the strain rate decreases, due to work hardening and cooling of the piece, until reaching approximately 0.004 s^{-1} at the final length of 1524 mm. During cogging, the maximum strain rate is reached at each blow. Consequently, the strain rate only depends on the block thickness or bar diameter. For initial square shapes of 1270 mm forged to a final bar of 406 mm diameter, the strain rate varies from 0.08 to 0.25 s^{-1}.

In the present work, strain rates of 0.001 s^{-1}, 0.01 s^{-1}, 0.1 s^{-1} and 1 s^{-1} are used to reproduce the industrial values. The strain for each test is set at 0.5, which is the max achieved during

the forging on H13 bars, during upset. Tests will also be performed with at 0.65, to analyse the effect of strain on the microstructure. The details of the strain rates calculations are provided below:

$$\dot{\varepsilon}(t) = \frac{d\varepsilon}{dt} = \frac{v(t)}{L_0}$$

$$v(t) = \frac{\Delta h}{\Delta t}$$

$$v(t)_{\,max} = 25.4\ mm/s$$

$$v(t)_{\,min} = 6.35\ mm/s$$

$$\dot{\varepsilon}(t) = \frac{d\varepsilon}{dt} = \frac{v(t)}{L_0} \tag{4.4}$$

$$\dot{\varepsilon}_{upset\ max}(t) = \frac{25.4\ mm/s}{2134\ mm} = 0.012\ s^{-1}$$

$$\dot{\varepsilon}_{upset\ min}(t) = \frac{6.35\ mm/s}{1524\ mm} = 0.004\ s^{-1}$$

$$\dot{\varepsilon}_{cogging\ max}(t) = \frac{102\ mm/s}{406\ mm} = 0.25\ s^{-1}$$

$$\dot{\varepsilon}_{cogging\ min}(t) = \frac{102\ mm/s}{1270\ mm} = 0.08\ s^{-1}$$

4.3.1.4 Holding time

Each sample is held 300 s at 1260 °C prior to deformation to achieve an equivalent grain size at each test for microstructural homogeneity. For lower deformation temperatures, the sample is cooled from 1260 °C and held 60 s to reach temperature uniformity through the sample.

4.3.2 Results

Two aspects of the compression tests were analyses: The stress strain curves and the microstructure.

4.3.2.1 Stress Strain Curves

The stress strain curves were obtained for the different temperatures and strain rates. As shown in Figure 4.14, the high frequency data acquisition as well as the uncertainty of measurement of the load cell and the extensometer revealed fluctuations in the measurements through the deformation process. However, these fluctuations do not affect the tendency of the stress-strain behavior. Thus, the number of data points was reduced and the curve was softened using a spline interpolation function.

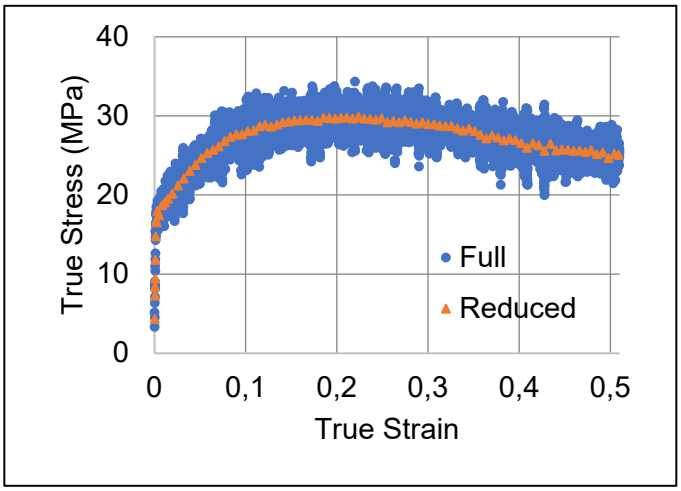

Figure 4.16 Full (high frequency data acquisition vs reduced data)

4.3.2.1.1 Repeatability test

A repeatability test was performed. The stress and strain results were reduced and, to calculate the error per equation (4.3), they were modeled using a polynomial logarithmic equation of the form:

$$\sigma = Aln(\varepsilon) + B\varepsilon + C\varepsilon^2 + E\varepsilon^3 + D \quad (4.5)$$

The reduced and modeled curves are presented in Figure 4.17. There was a very good fit between the tests with an average absolute relative error of 3%.

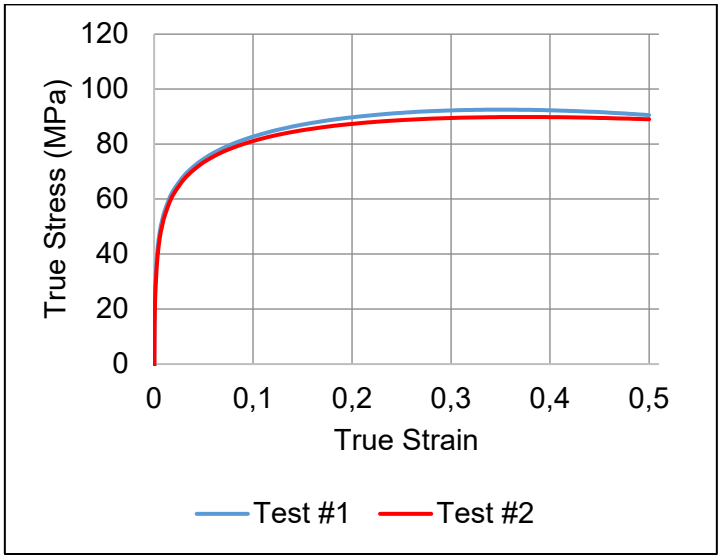

Figure 4.17 Repeatability tests at 1200 °C, 1 s^{-1}

4.3.2.1.2 Correction for dilatation and friction

Then, the results were corrected for dilatation and friction, as recommend per the Gleeble-3800 procedure and as performed in other research (Bitterlin & Shahriari, 2018 ; Dieter, 1988 ; T. Li, 2019). The correction for adiabatic heating was non-significant for this alloy with a high specific heat capacity and the relatively low strain rates used in the present study.

The Gleeble-3800 software requires the initial dimensions of the sample ($L_{0,rt}$ and $D_{0,rt}$) to perform the calculation of the stress strain curves. The dimensions that were input for this experiment were measured at room temperature, but at the time of the deformation, the

sample size was bigger due to dilatation. So, the dilated dimensions (L_0 and D_0) were obtained by adding the increase of the length (ΔL_{dilat}) measured at the end of the heating sequence to $L_{0,rt}$. $D_{0,rt}$ was proportionally increased. During the deformation test, the length gage was set to zero before the heating sequence and right before the deformation start. The dilated dimensions were used to recalculate the stress strain curves by using Eq. (1.5).

As per the Gleeble-3800 procedure, friction should also be eliminated. The model suggested and used in several studies (Bitterlin & Shahriari, 2018 ; Dieter, 1988 ; T. Li, 2019) is:

$$\sigma_{corr} = \frac{C^2 P}{2(e^C - C - 1)} \tag{4.6}$$

$$C = \frac{2\mu r_{th}}{L} \tag{4.7}$$

$$r_{th} = \frac{r_0}{2}\sqrt{\frac{L_0}{L}} \tag{4.8}$$

With μ the constant friction coefficient, $r_{th}$and L respectively the instantaneous theoretical radius and length, P the stress with friction, and C the model constant. The barreling factor needs to be calculated to estimate the friction coefficient:

$$b = 4\left(\frac{r_{f,max} - r_{f,min}}{r_{th}}\right)\left(\frac{L_f}{L_0 - L_f}\right) \tag{4.9}$$

With $r_{f,max}$, $r_{f,min}$ and L_f, respectively the maximum radius, minimum radius and length of the sample at the end of the deformation. The barreling factor that considers the final shape of each sample allows to calculate a friction coefficient that reflects the surface condition (roughness, lubrication) of each test:

$$\mu = \frac{\frac{r_{th}}{L_f} b}{\frac{4}{\sqrt{3}} - \frac{2b}{3\sqrt{3}}} \tag{4.10}$$

The final reduced and corrected curves at each tested temperature and strain rate are shown in Figure 4.18. The flow stress is observed to decline with increasing temperature and decreasing strain rate, which is expected. Also, the four typical stages of a high temperature stress-strain curve are identified, at specific conditions:

1. Strain hardening (accumulation of dislocations)
2. Transition (permanent deformation and activation of softening mechanisms DRV and DRX)
3. Softening (higher contribution of DRV and DRX mechanisms)
4. Steady state (equilibrium between strain hardening and softening)

At all temperatures and strain rates, the strain hardening and transition stages were obvious. The softening stage was distinct only at the highest temperature (1260 °C) and lower strain rates (0.001 s^{-1} and 0.01 s^{-1}).

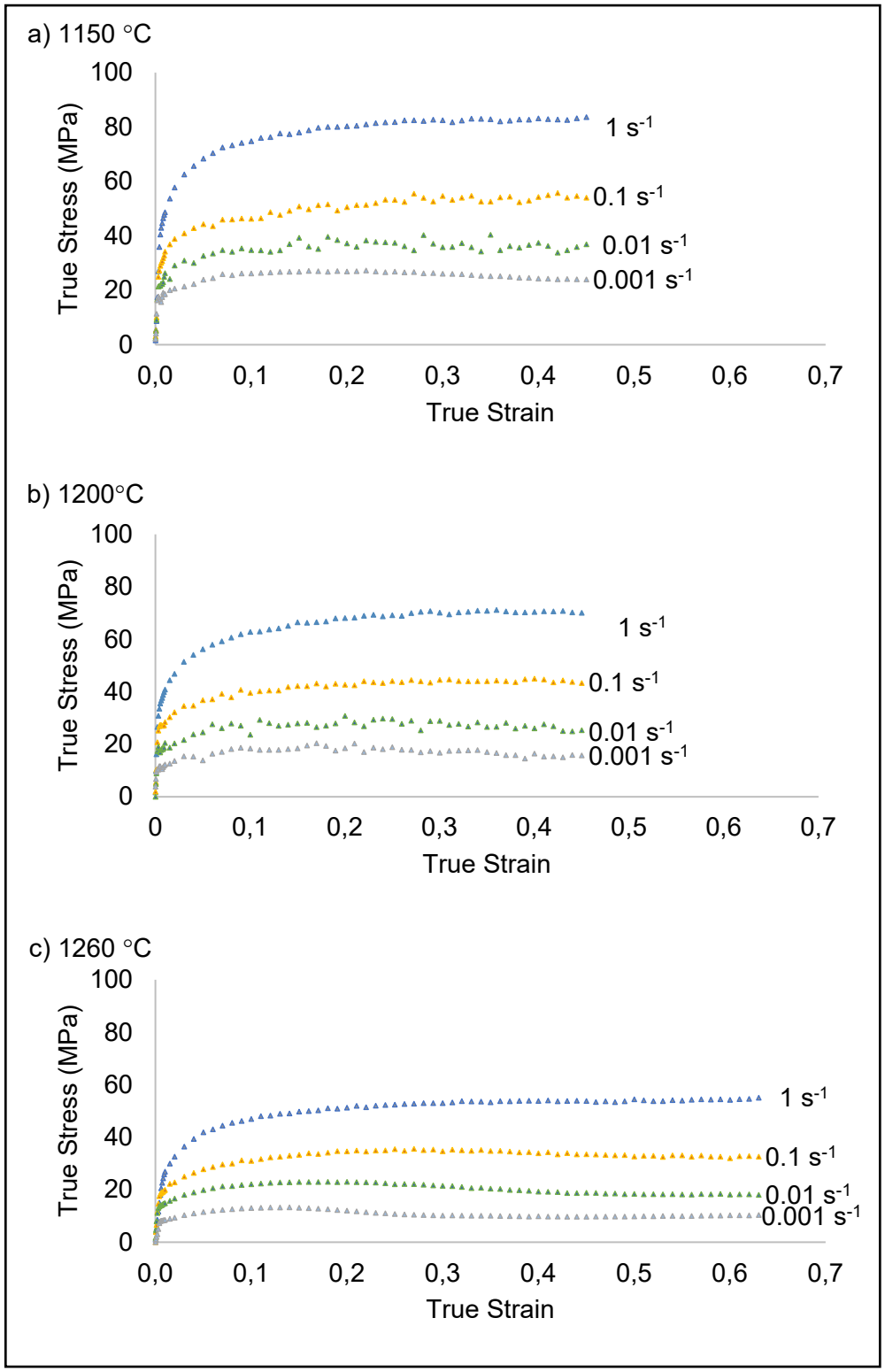

Figure 4.18 Reduced and corrected experimental stress-strain curves at different temperatures and strain rates

4.3.2.1.3 Constitutive modeling of stress strain curves

As described in the literature review, three constitutive models were studied to predict the evolution of the stress with the applied strains and strain rates at different temperatures. H&S and JC were preferred for their simplicity and ease to incorporate in the material data code of a simulation software. Arrhenius constitutive model was also of great interest because it is better adapted for the modelisation of a great dynamic softening behavior, which occurred at the strain rates of 0.01 s^{-1} and 0.001 s^{-1}.

First, the H&S model constants were calculated employing the algorithm of non-linear optimisation Solver of Microsoft Excel. The resulting relation between stress, strain, strain rate, temperature and the various corresponding constants was:

$$\sigma = 3127e^{-0.00512T}\varepsilon^{0.0944}\dot{\varepsilon}^{0.189}e^{\frac{-0.000860}{\varepsilon}}(1+\varepsilon)^{0.00226T}e^{-2.17\varepsilon}T^{0.333} \tag{4.11}$$

The experimental and predicted results with H&S model are presented in Figure 4.19. The curves followed well the experimental data for values up to the peak stress. However, the model did not show an accurate deflection for the softening stage at lower strain rates. The total average absolute relative error was 10%.

Then, the Arrhenius constitutive model was defined as:

$$\sigma = \frac{1}{\alpha} ln\left\{\left(\frac{Z}{A}\right)^{1/n} + \left[\left(\frac{Z}{A}\right)^{2/n} + 1\right]^{1/2}\right\} \tag{4.12}$$

$$Z = \dot{\varepsilon} exp\left(\frac{Q}{RT}\right) \tag{4.13}$$

The polynomial equations for α, n, Q and $\ln(A)$ were developed as described in section 2.3.4, with the exception that a natural logarithm parameter was added for a correlation with the data. The results of the relationships for the calculation of n_1, β, n and Q at a strain of 0.49 are illustrated in Figure 4.20. Figure 4.21 shows the polynomial fit for the determination of the constants of the model and Eq. (4.17) presents the calculated polynomial equations. At last, the experimental and predicted results with Arrhenius model are presented in Figure 4.22.

The total average absolute relative error was 10%. It was observed that the model predicted the transition stage as well as the softening stage at lower strain rates. However, the stress was increasing from a strain of approximately 0.3 for the strain rates of 1 s^{-1} and 0.1 s^{-1}. This showed that the model was not accurate to follow two types of deformation curves: with and without an important softening stage.

At last, a third model, JC, was calculated. The constants were calculated employing the algorithm of non-linear optimisation Solver of Microsoft Excel. The resulting relation between stress, strain, strain rate, temperature and the various corresponding constants was:

$$\sigma = (-65.28 + 95.70\varepsilon^{0.02928})(1 + 0.4186ln\dot{\varepsilon^*})\left(1 - T^{*0.9077}\right) \quad (4.14)$$

With

$$\dot{\varepsilon}^* = \dot{\varepsilon}/0.001 \quad (4.15)$$

$$T^* = (T - 1423)/(1736 - 1423) \quad (4.16)$$

Where $\sigma\ is$ the flow stress, ε is the strain and $\dot{\varepsilon^*}$ is the dimensionless strain rate from $\dot{\varepsilon}^* = \dot{\varepsilon}/\dot{\varepsilon}_{ref}$. $\dot{\varepsilon}_{ref}$ is the reference strain rate and corresponds to the lowest strain rate of the study interval. $T^* = \left(T - T_{ref}\right)/\left(T_m - T_{ref}\right)$ is the relative temperature, T is the experimental temperature, T_{ref} is the reference temperature (lowest of the study interval), and T_m is the melting temperature of the material, in Kelvins.

The experimental and predicted results with JC model are presented in Figure 4.19. As for the H&S model, the JC model did not show an accurate deflection for the softening stage at lower strain rates. In addition, the calculated curves did not adapted to the transition and steady state observed on the experimental data. The total average absolute relative error was 17%, the highest compared to the H&S and Arrhenius models.

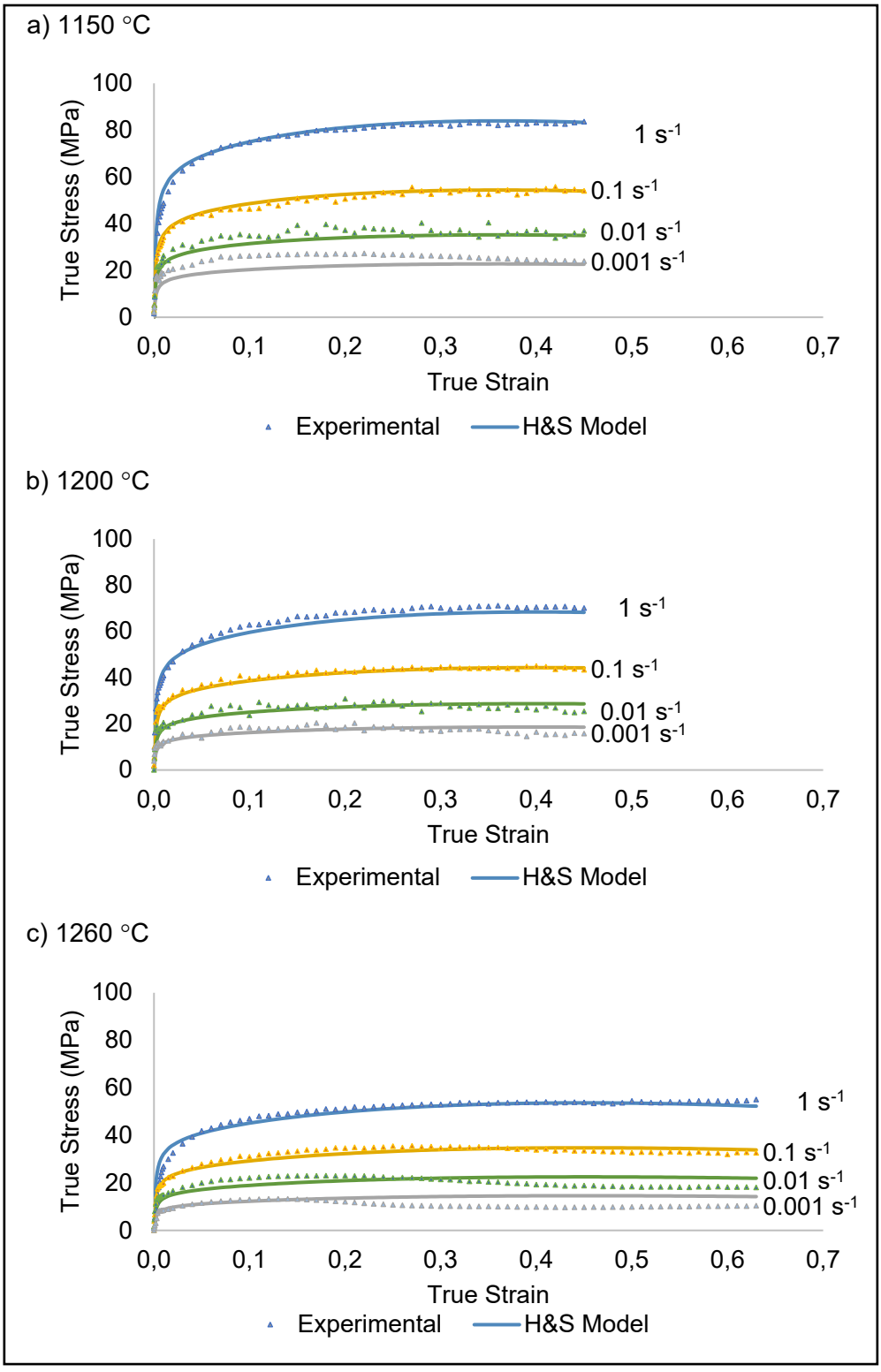

Figure 4.19 Experimental stress strain curves at different temperatures and strain rates vs H&S model

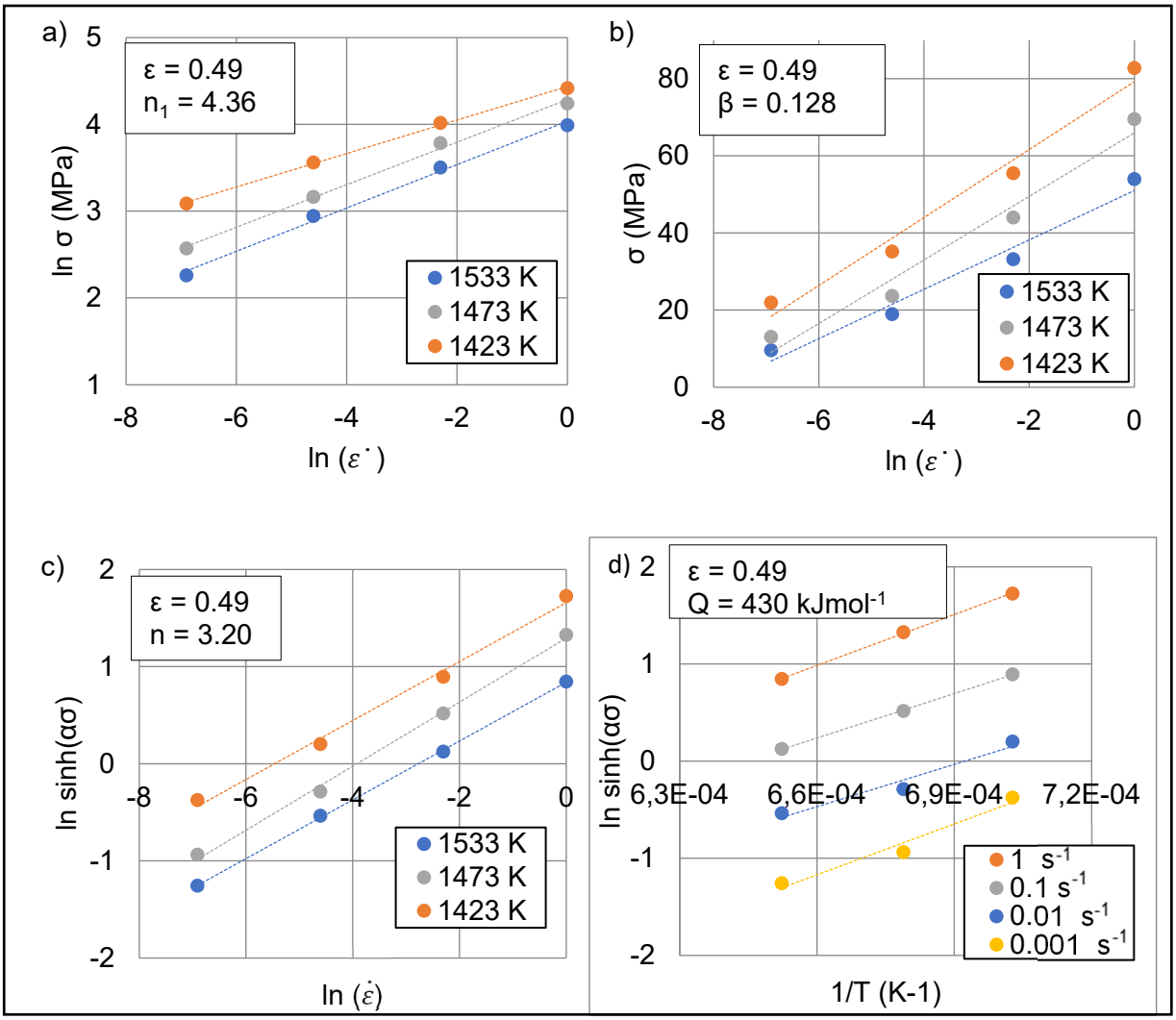

Figure 4.20 Example at ε = 0.49 of the relationships of (a) $\ln(\sigma)$ vs $\ln(\dot{\varepsilon})$ (b) σ vs $\ln(\dot{\varepsilon})$ (c) $\ln(\sinh(\alpha\sigma))$ vs $\ln(\dot{\varepsilon})$ (d) $\ln(\sinh(\alpha\sigma))$ vs $\frac{1}{T}$

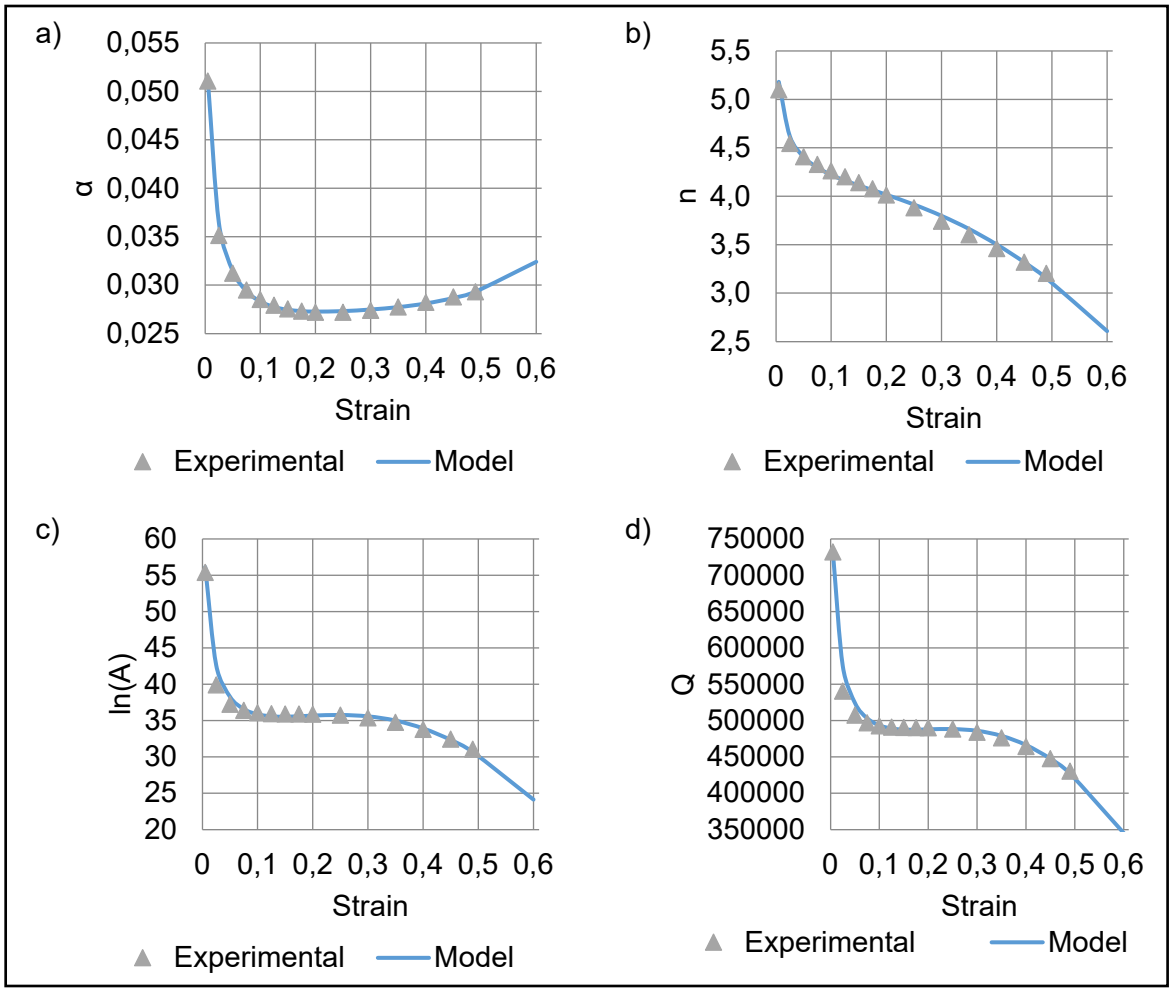

Figure 4.21 Polynomial fit of variation of a) α, b) n, c) $\ln(A)$ and d) Q with strain

$$\begin{aligned}
\alpha &= -0.004399 - 0.01037\ln(\varepsilon) + 0.1047\varepsilon - 0.18\varepsilon^2 + 0.155\varepsilon^3 \\
n &= 3.174 - 0.3769\ln(\varepsilon) + 2.4\varepsilon - 6.105\varepsilon^2 \\
\ln(A) &= 4.308 - 9.685\ln(\varepsilon) + 106\varepsilon - 135.4\varepsilon^2 \\
Q &= 732185 \times (0.2021 - 0.1485\ln(\varepsilon) + 1.461\varepsilon - 1.559\varepsilon^2 - 0.5647\varepsilon^3)
\end{aligned} \tag{4.17}$$

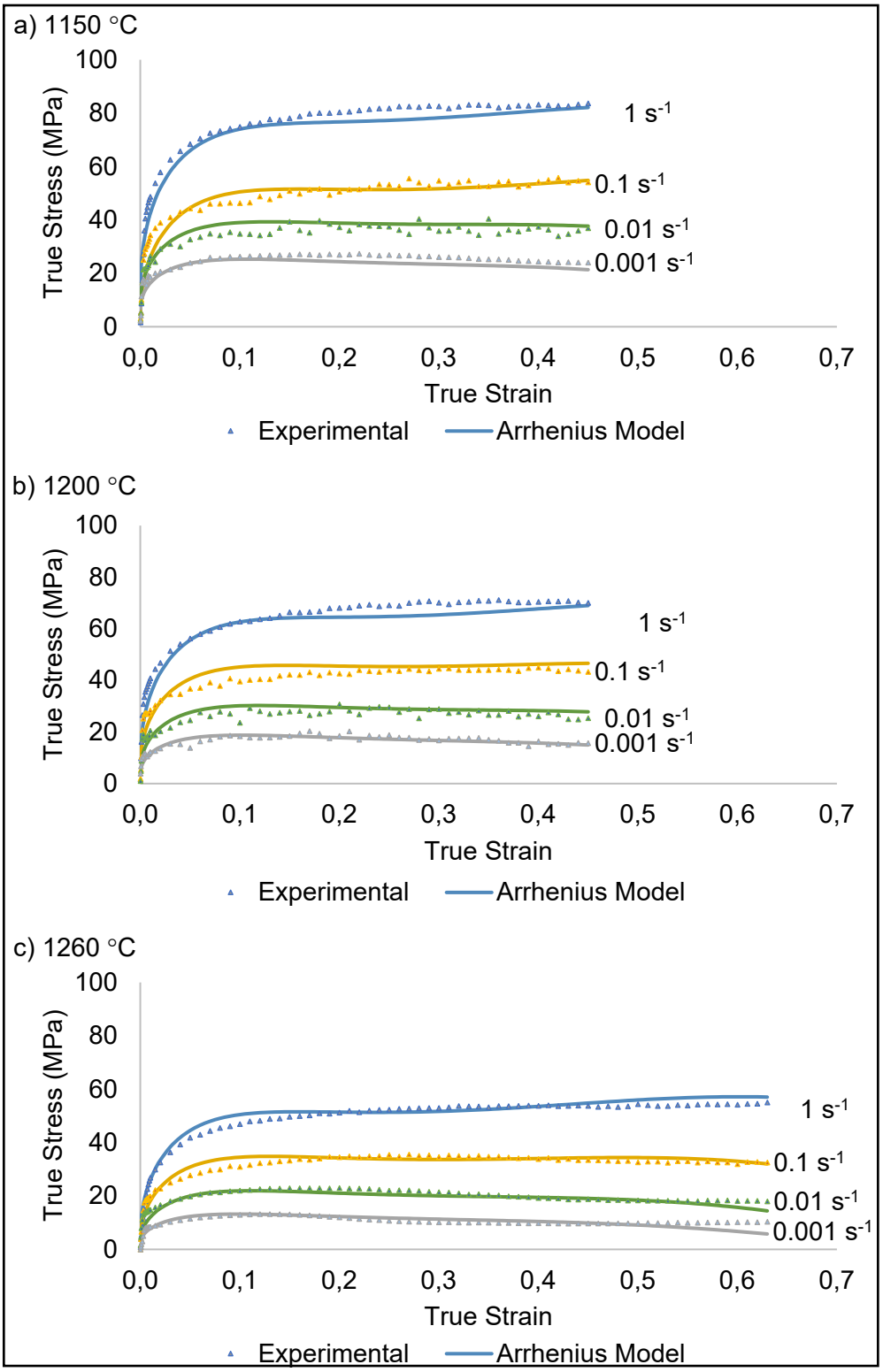

Figure 4.22 Stress strain curves at different temperatures and strain rates, experimental vs Arrhenius model

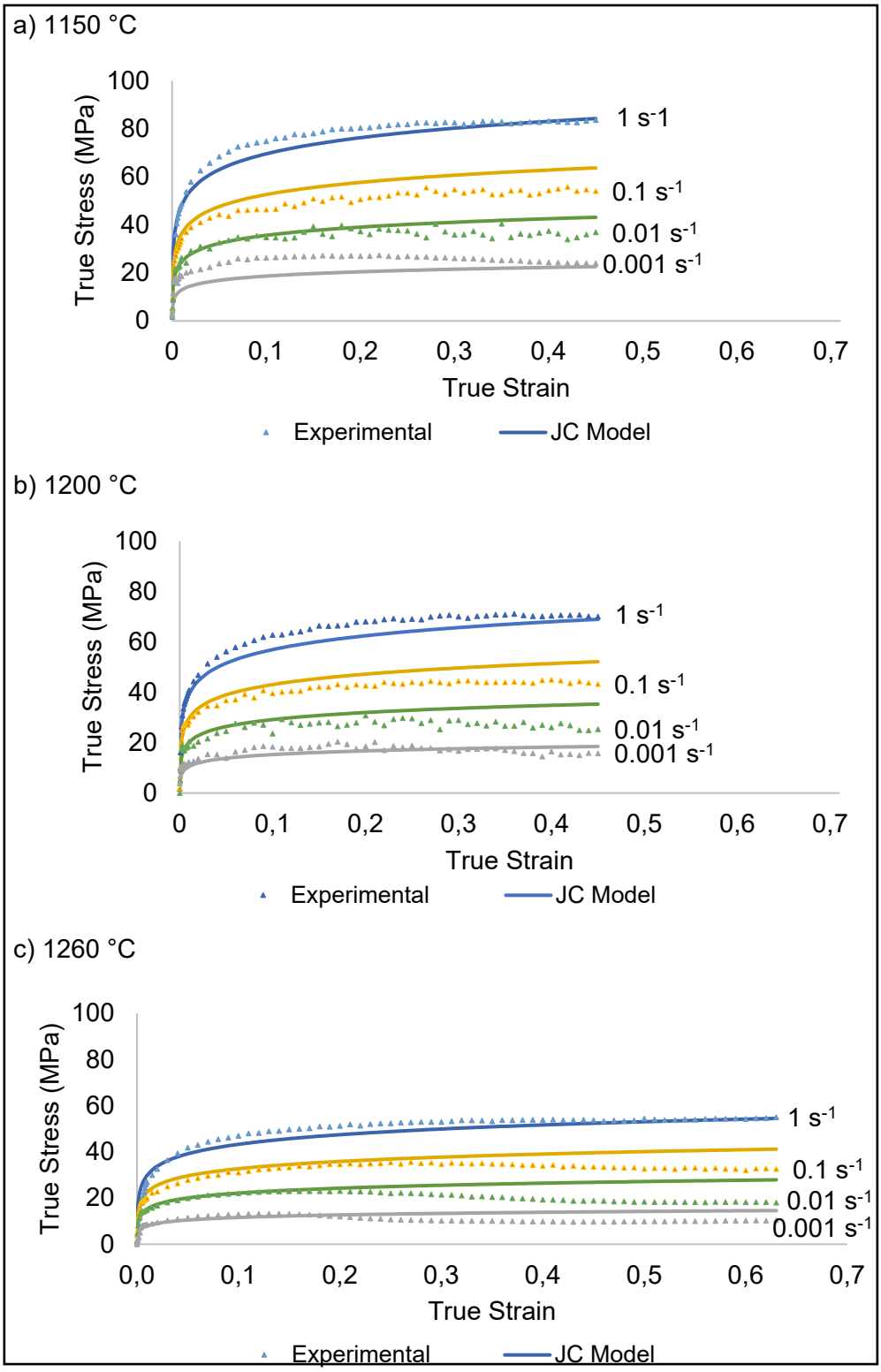

Figure 4.23 Stress strain curves at different temperatures and strain rates, experimental vs JC model

4.3.2.1.4 Comparison with calculated curves from databases

The experimental data and calculated models with lower average relative error (Arrhenius and H&S) were compared to available curves from two different simulation software databases: JMATPRO® and FORGE® NxT. The composition of the investigated alloy was entered in the JMATPRO® software. Figure 4.24 shows the results at 1260 °C, (0.001 s^{-1} and 1 s^{-1}). This comparison revealed important differences in the shape of the curves. First, the JMATPRO® curves showed a straight strain hardening stage and softening at a constant rate. There was no transition stage. The DRV and DRX contributions for softening occurred at a fixed strain, while according to the experimentation they were transient. Practically, the stress would be overestimated if this model was used for simulation in low deformation conditions (strains below 0.3). At higher deformation, after the peak stress, the stress error is lower, but nonetheless it was of -8% to 52%. Secondly, the FORGE® NxT curves showed a better estimation of the transition stage. This was because the model is also a H&S type, with five parameters. However, the peak and steady stage stress was 30% to 172 % higher. In simulation, the stress would be overestimated in medium to high deformation conditions (strain of 0.05 to 0.6). In summary, two important factors could explain the observed differences. The JMATPRO® equation took account of the chemical composition, but probably used a different constitutive model (not provided). While FORGE® NxT software used H&S type model, but considered an average chemical composition.

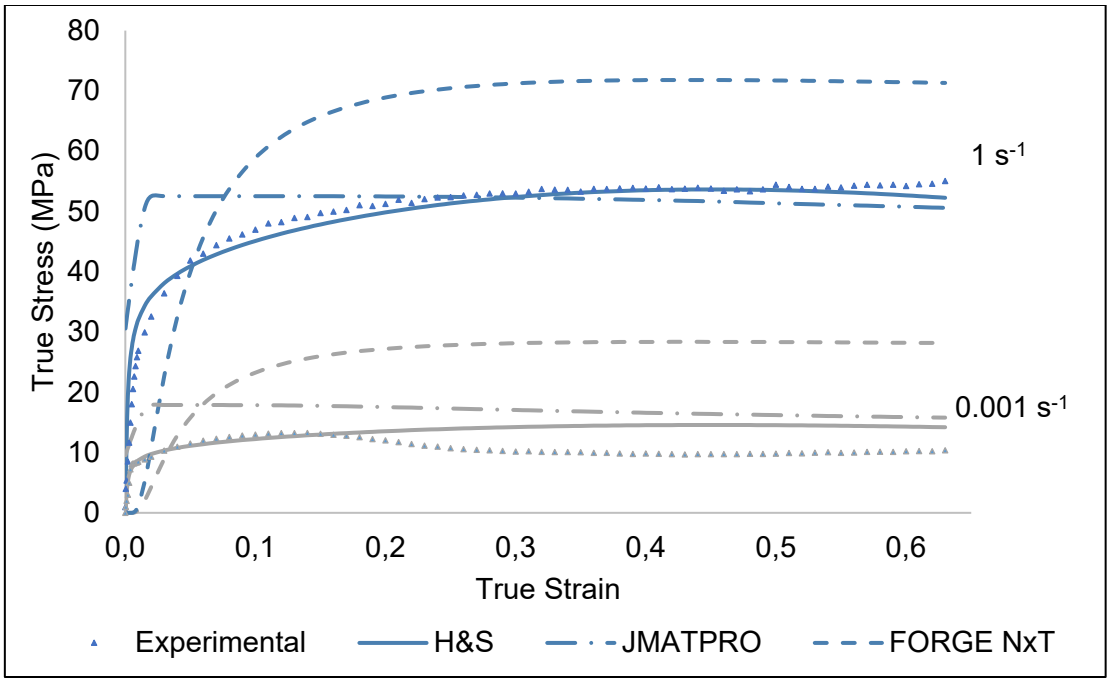

Figure 4.24 Comparison of experimental and modeled stress-strain curves at 1260 °C, 0.001 s^{-1} and 1 s^{-1}

4.3.2.1.5 Analysis of DRV and DRX softening mechanisms

As briefly described in section 1.3.1, the kinetics of recrystallization can be quantified by Avrami equation (Bitterlin & Shahriari, 2018):

$$X = 1 - \exp(-kt^{n_{DRX}}) = 1 - \exp\left[-k\left(\frac{\varepsilon - \varepsilon_c}{\varepsilon_p}\right)^{n_{DRX}}\right] \quad (4.18)$$

The calculation of this equation requests the identification of critical, peak and steady state parameters at each temperature and strain rate (ε_p, σ_p, ε_c, σ_c, ε_s, σ_s). Then, the constants k and n_{DRX} can be calculated when the experimental recrystallization fraction is estimated using:

$$X = \frac{\sigma_p - \sigma}{\sigma_p - \sigma_s} \quad (4.19)$$

According to Najafizadeh (2006) and Bitterlin (2018) studies, the double differentiation method was proved accurate to identify the critical, peak and steady state parameters. In this study, the first ($\theta = \frac{\partial\sigma}{\partial\varepsilon}$) and second ($\frac{\partial\theta}{\partial\sigma}$) differentiation were calculated. To do so, the corrected

experimental data of each temperature and strain rate condition was modeled independently to obtain a smooth curve. The algorithm of non-linear optimisation Solver of Microsoft Excel was used. This polynomial equation showed the best fit, with a total average absolute relative error of 4.9%:

$$\sigma = Aln(\varepsilon) + B\varepsilon + C\varepsilon^2 + D\varepsilon^3 + E \quad (4.20)$$

The results are illustrated in Figure 4.25. The peak parameters correspond to the highest true stress value when the work hardening θ equals 0. The steady state parameters can be identified when there is a lower true stress with a work hardening θ of 0. In the study range, steady state occurred only during the test at a temperature of 1260 °C and a strain rate of 0.001 s^{-1}. With only one validation of the steady state, the kinetics of recrystallization was not calculated. However, the critical parameters could be identified, and they correspond to the first minima of the second differentiation graph (Figure 4.25 c)). The values of the parameters are presented in Table 4.6. In addition, this method allowed to identify whether softening occurred. This corresponds to a stress drop after the peak stress, confirmed with a θ value below 0 on the first differentiation graph. The presence of a softening stage is documented in Table 4.6. Finally, the corresponding Zener-Hollomon parameter, described in Eq. (15), was estimated for each condition with the activation energy determined for the Arrhenius model (Q = 430 $kJmol^{-1}$ at ε = 0,49). It quantifies the flow stress behavior as a function of temperature and strain rate. Theoretically, lower Z (low strain rate and high temperature), the driving force is higher and onset DRX (T.-B. Zhang, 2013). The results are also presented in Table 4.6.

The overall trend showed that the critical and peak strain and stress increased with strain rate and decreased with temperature. The minimum peak stress was measured during the test at 1260 °C, 0.001 s^{-1} with a value of 12.5 MPa, whereas the maximum was measured at 1150 °C, 1 s^{-1} with a value of 82.9 MPa. In addition, an important increase of the critical and peak strain was noted between 0.01 s^{-1} and 0.1 s^{-1}. Respectively at 1150 °C, 1200 °C and 1260 °C, the increase was of 67%, 76% and 120%. This indicated a transition in the kinetic of recrystallization.

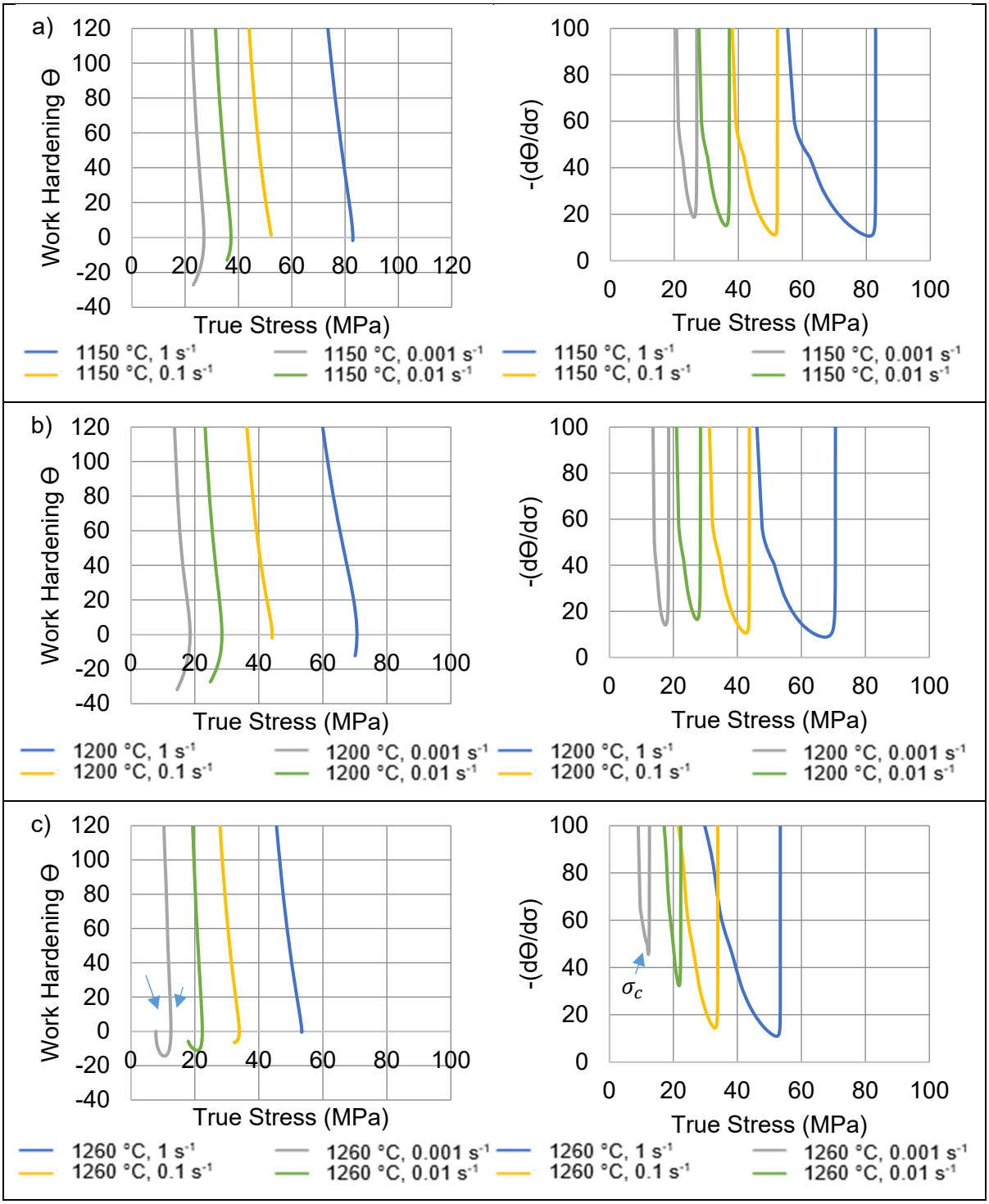

Figure 4.25 First and second differentiation of the modeled data a) 1150 °C, b) 1200 °C, c) 1260 °C

Table 4.6 Stress strain curves analysis by the first and second differentiation method, and estimation of Z parameter at ε = 0.49

T (°C)	$\dot{\varepsilon}$ (s^{-1})	ε_c	σ_c (MPa)	ε_p	σ_p (MPa)	ε_s	σ_s (MPa)	Softening	Z (at ε = 0.49)
1150	0.001	0.10	26	0.19	27			Yes	6E+12
	0.01	0.13	36	0.26	37			Yes	6E+13
	0.1	0.21	51	0.43	52			No	6E+14
	1	0.21	81	0.42	83			No	6E+15
1200	0.001	0.10	18	0.21	19			Yes	2E+12
	0.01	0.11	27	0.21	28			Yes	2E+13
	0.1	0.20	43	0.40	44			No	2E+14
	1	0.18	67	0.37	71			Yes	2E+15
1260	0.001	0.06	12	0.11	13	0.6	8	Yes	5E+11
	0.01	0.07	22	0.13	22			Yes	5E+12
	0.1	0.15	33	0.30	34			Yes	5E+13
	1	0.22	52	0.49	53			No	5E+14

4.3.2.2 Microstructure of the Deformed Samples

Samples were cut as shown in Figure 4.26 to observe the microstructure in the longitudinal (L) and transversal (T) sections of the deformed samples. The sections were mechanically polished using different SiC paper up to 1200 grit followed by 1µm diamond paste as the final polishing step and etched with Nital 5%. Figure 4.27 to Figure 4.30 show the effect of strain rate, temperature and strain on the microstructure.

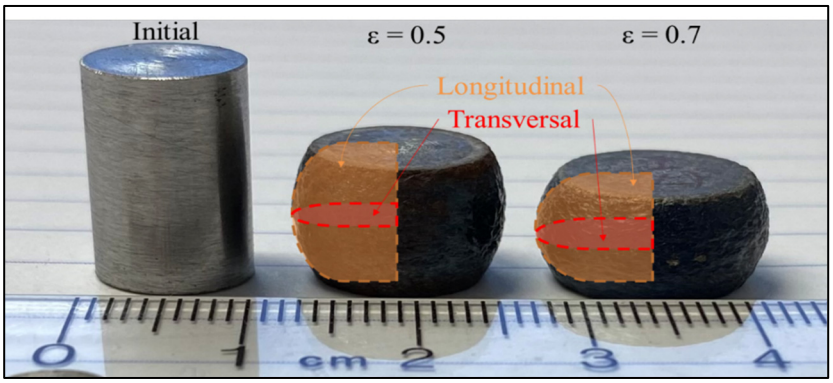

Figure 4.26 Longitudinal and transversal sections of the

deformed samples for microstructural observation

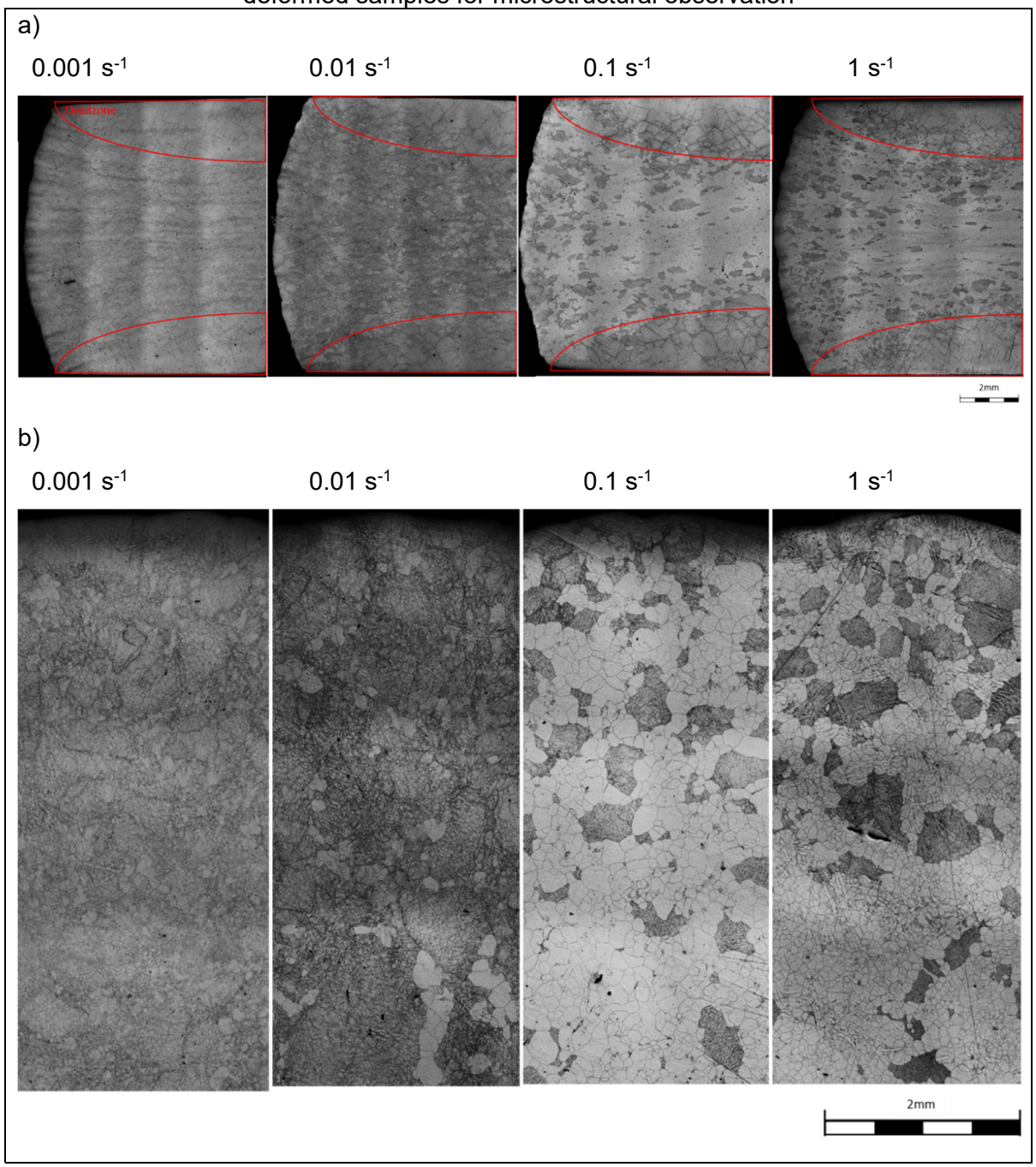

Figure 4.27 Effect of strain rate at 1260 °C, on microstructures of longitudinal (a) and transversal (b) sections, Nital 3%, laser microscopy

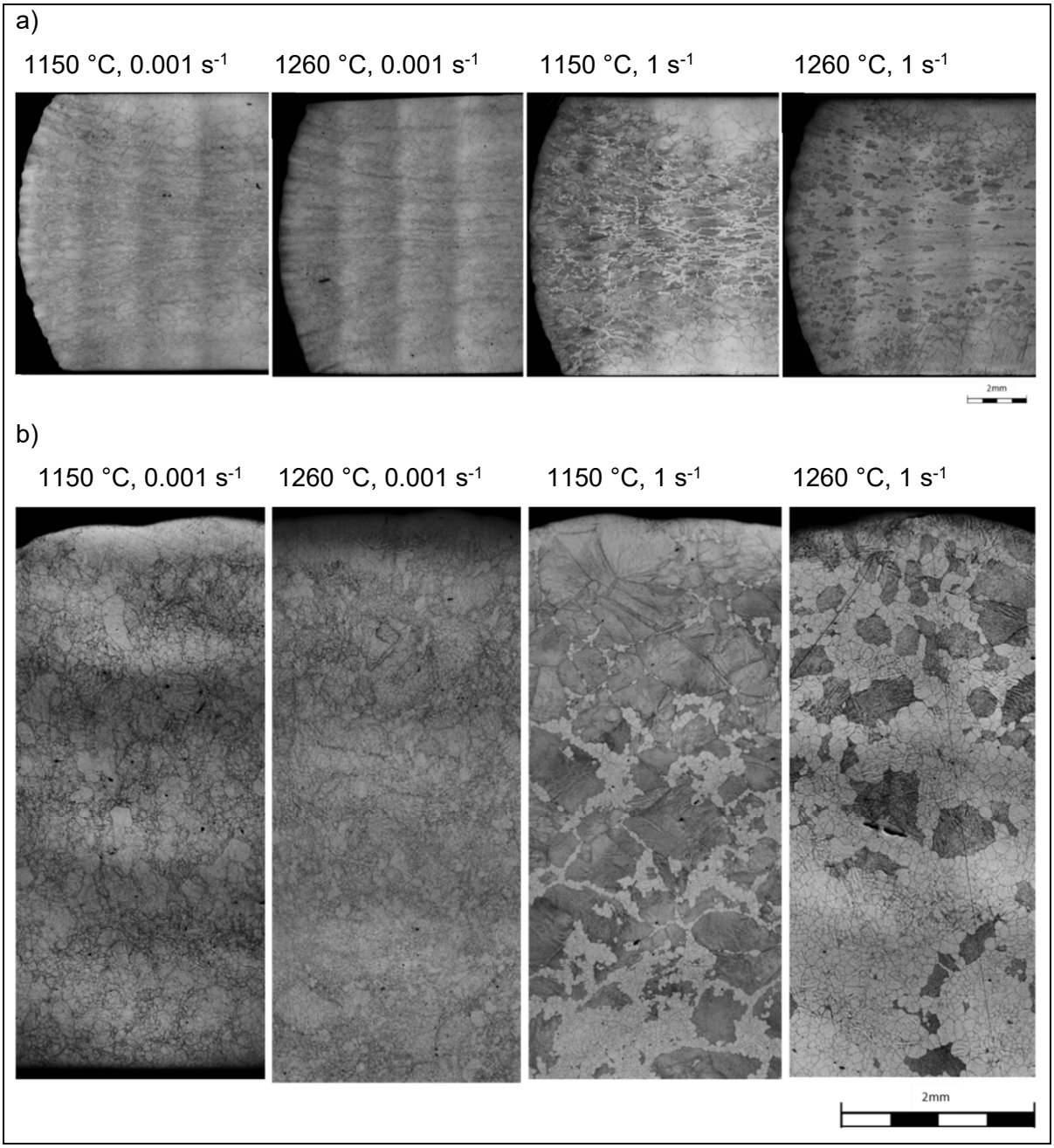

Figure 4.28 Effect of temperature on microstructures of longitudinal (a) and transversal (b) sections, Nital 3%, laser microscopy

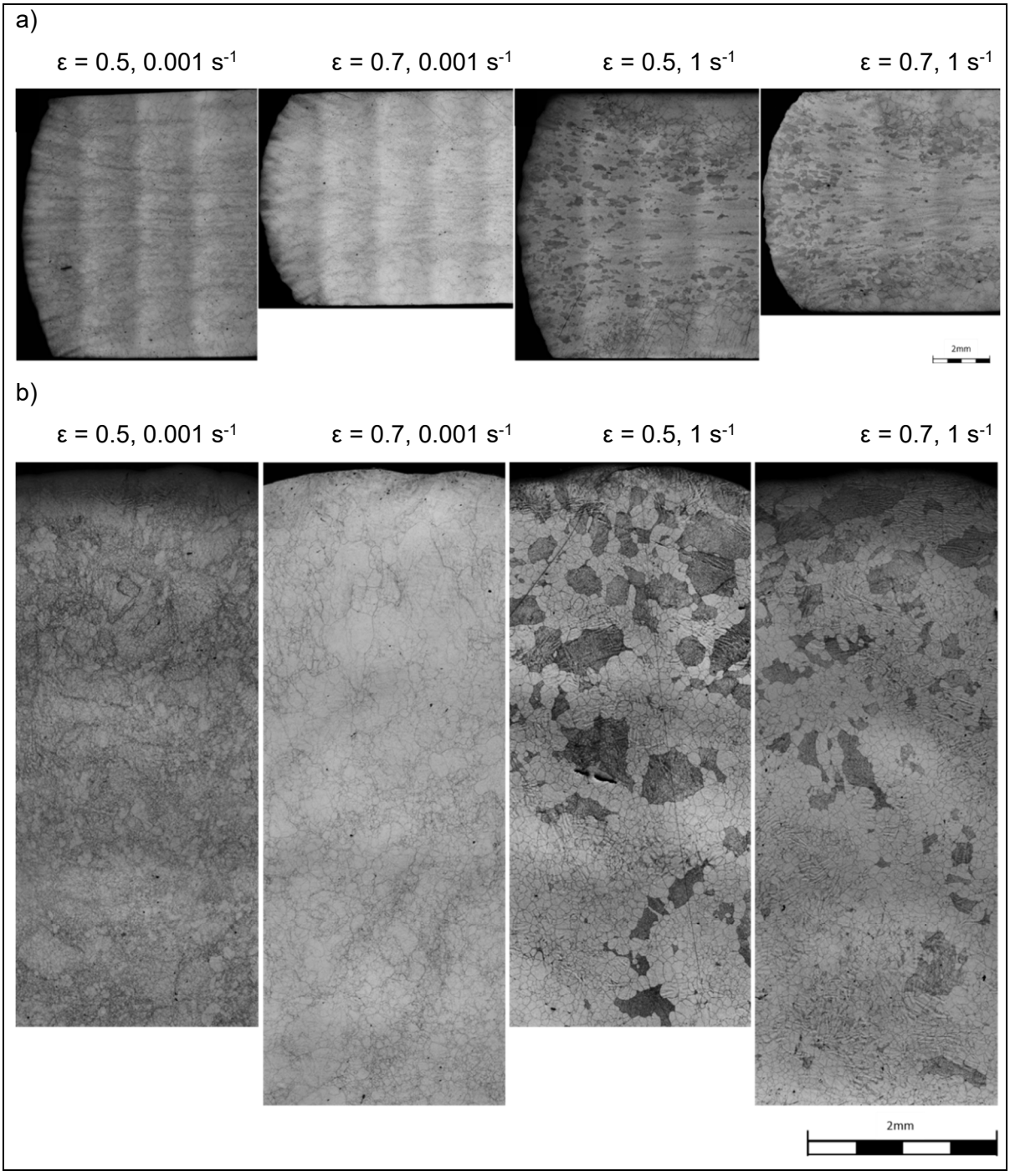

Figure 4.29 Effect of strain at 1260 °C, on microstructures of longitudinal (a) and transversal (b) sections, Nital 3%, laser microscopy

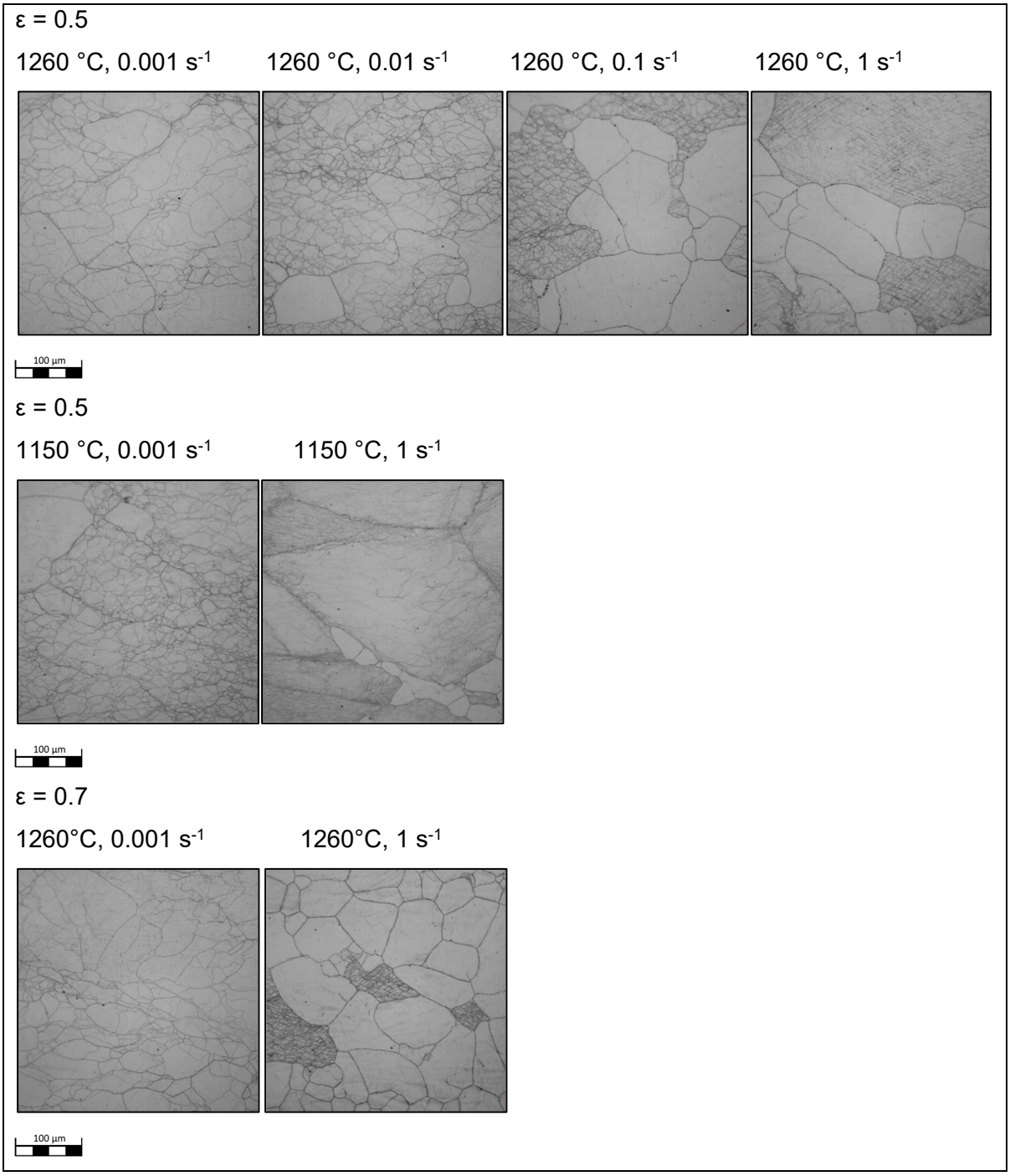

Figure 4.30 Comparison of microstructures in the intense shearing zone, at different temperatures, strain rates and strains, Nital 3%, optical microscopy, 200X

From a general point of view of the longitudinal figures (a), the typical characteristic deformation zones were observed, as indicated in Figure 4.31 (Dieter, 1988).Larger grains were visible near the surfaces in contact with the anvils. These areas with coarse grain size coincided with dead zones, areas with little or no flow stress. Without deformation, refining mechanisms such polygonization and recrystallization could not occur. Thus, a larger grain size was observed. This showed that even with Tantalum sheet and Nickel paste as lubricant, there was friction which limited the metal flow near the contact surfaces. In addition, the average grain size in the dead zone of the samples deformed at 1260 °C was 352 μm (1 s^{-1}) to 430 μm (0.001 s^{-1}). These averages are larger than the estimated grain sizes for a holding time of 300 s to 540 s from the isothermal holding tests. However, they are in the range of the plateau of slower grain growth kinetics reached after 2700 s. The larger grain size could be related to the different heating rate and heat transfer conditions of the hot compression test However, this comparison indicates that the refining mechanisms did not occur in the dead zones, because the grain size is close to the stable state achieved during the isothermal holding tests at 1260 °C. Lastly, especially on the samples deformed at 1 s^{-1}, the edges had a coarser grain size than the center, which corresponded to moderate deformation zones.

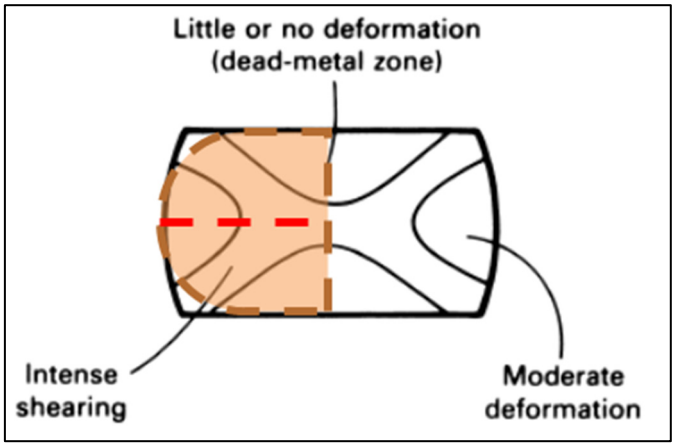

Figure 4.31 Characteristic deformation zones in a compressed cylinder
Taken from Dieter (1988)

The following observations compare the microstructure at the center of the samples, namely the intense shearing zone. The effect of strain rate is presented in Figure 4.27, with the results at a deformation temperature of 1260 °C. When comparing the center of the samples at 0.001 s^{-1} to 0.01 s^{-1}, the grain structure was finer at the lowest strain rate. However, from 0.1 s^{-1} to

1 s^{-1}, the microstructure was finer at the highest strain rate. Then, the effect of temperature is presented in Figure 4.28. At low and high strain rates, the microstructure was finer at higher strain rate. Finally, Figure 4.29 shows the effect of strain. At 0.001 s^{-1}, the microstructure was finer at lower strain, 0.5. However, at 1 s^{-1}, the sample with a strain of 0.7 showed a higher recrystallized proportion with similar grain size.

4.3.3 Discussion

The hot compression tests provided reliable and repeatable data to plot the stress strain curves of Finkl Steel H13 steel, from forging temperatures of 1150 °C to 1260 °C and strain rates of 0.001 s^{-1} to 1 s^{-1}. However, modelling the curves was challenging due to the transition in the activation of dynamic softening mechanisms. The models were inaccurate to follow two types of deformation curves: with and without an important softening stage. While H&S equation showed a good fit for the work hardening and transition stage, it could not be set to follow the stress drop of high temperature and low strain rate conditions. Conversely, the best solution for Arrhenius equation, in terms of total relative error, was with a stress drop in all conditions. Overall, JC model resulted in the poorer fit with 17 % total absolute relative error, and H&S and Arrhenius models showed similar fits with both 10 % total absolute relative error.

When comparing with the curves from two different databases, JMATPRO® and FORGE® NxT, there are important differences which justifies modelling experimental curves. For JMATPRO®, the distinction between the equations resulted in important gaps relative to the stages of the curve (Chadha & Shahriari, 2015). The shapes of the curves were very different, with no transition stage and a constant softening rate with the JMATPRO® relations. For FORGE® NxT, the distinction between the chemical compositions resulted in a gap most likely on the stress level. The shape of the curves was similar, but stress was systematically higher for FORGE® NxT. Perhaps, the chemical composition used for this database has a higher content of strengthening elements, such those that can form carbides (Cr, Mo, V) (Ning, 2017).

As mentioned for the modelling, the curves showed a transition in the activation of dynamic softening mechanisms. The double differentiation method revealed that the highest temperature (1260 °C) and lowest strain rates (0.001 s^{-1} and 0.01 s^{-1}), the condition of low Z parameter (5E+12 and 5E+11), provided sufficient driving force for early activation of the

softening mechanism and stress drop. In these conditions, the peak deformation ε_p was of 0.11 and 0.13. This implied that the high temperatures and low strain rates along with dissolution of carbides allowed dislocation annihilation, polygonization and subsequent formation of recrystallization nuclei that reduced the stress for further deformation. Conversely, higher strain rates do not show softening even at high temperatures, meaning that the driving force was not reached at high Z parameter. From a Z parameter of 2E+14, ε_p was of 0.37 and more.

In addition, the transition in the activation of dynamic softening mechanisms is observable on the microstructures. The conditions with low Z parameter (1260 °C at 0.001 s^{-1}, 1260 °C at 0.01 s^{-1}, and 1150 °C at 0.001 s^{-1}) showed similar features. Their grain structure appeared to be uniform. With lower strain rates, nucleation occurs by bulging near an existing boundary, then creating areas with high energy, ready for DRX (Dehghan-manshadi, 2007). With H13 steel in these conditions, the high driving force provided sufficient energy to activate DRX across the microstructure and complete a uniform recrystallization. Conversely, the samples with high Z parameter (1260 °C at 0.01 s^{-1}, 1260 °C at 1 s^{-1}, and 1150 °C at 1 s^{-1}) showed complex microstructures. At higher strain rates, the intense interaction of dislocations and limited time for cross slip led to accumulation of the strain in specific areas (Chegini, 2020). Consequently, in some cases, the deformation is non-uniform. On the microstructure, this is reflected by the observation of a mix of undeformed grains, new grains and grains with a very fine substructure. At 1150 °C, 1 s^{-1}, (lowest Z) recrystallized grains are clearly observed near grain boundaries of the initial austenitic grain. This is because the density of nuclei is probably higher there because of a higher density of dislocation and precipitates.

Finally, the isothermal conditions experienced by the samples are comparable to the conditions found at the centerline of large forgings, which was the main objective of this study. In other words, the samples are comparable to finite elements inside a workpiece with a specific set of constant temperature and strain rate. In this perspective and according to the results, a set of higher strain rate or lower temperature (low Z) could lead to non-uniform deformation. Under-deformed or conversely highly stresses areas could result in the production of defects discussed in the industrial problematic definition; i.e., unclosed porosities or voids generated by secondary tensile stresses. Conditions of low Z are preferable to activate the dynamic mechanisms that allow a more uniform deformation conditions.

CONCLUSIONS

During this study, different aspects of the thermomechanical forging process of H13 steel were analysed. The objective was to study the influence of isothermal soaking and deformation on microstructure evolution and the flow behavior at the centerline of a large forging. It was achieved by providing material models and process control limits to optimise H13 forging process.

The present study analysed important thermomechanical and microstructural phenomena to consider for a better understanding of H13 tool steel behavior during forging:

- At forging temperatures of 1150 °C to 1260 °C, the kinetic of grain growth highly depends on the dissolution of carbides. At 1150 °C, Cr, Mo and V rich carbides restricted the motion of grain boundaries resulting in almost no grain growth. At 1175 °C, Cr and Mo rich carbides dissolved and released the grain boundaries. This can allow a better flow of material during deformation and promote porosity closure.
- For simulation purpose, the H&S or Arrhenius models can be used to describe the stress-strain curves of H13 tool steel at temperatures of 1150-1260 °C and a strain rate of 0.001 s^{-1} to 1 s^{-1}. However, the softening stage at high temperature (1260 °C) and low strain rates (0.001 s^{-1} to 0.01 s^{-1}) was not taken in account with H&S. Conversely, with Arrhenius, the softening stage is too important at low temperature (1150 °C) and high strain rates (0.1 s^{-1} to 1 s^{-1}). Model selection must be done with care. Curves calculated with JMATPRO®, FORGE® NxT or H&S showed great differences with the experimental data (yield, peak stress and transition stage). Further work should be done to determine the best model for H13 tool steel with specific chemical composition.
- The microstructure analysis showed that a high strain rate (0.1 s^{-1} to 1 s^{-1}) promoted non-uniform deformation and localized DRX, which resulted in a mixed grain size during the experimental compression tests conditions. Conversely, the low strain rates (0.001 s^{-1} to 0.01 s^{-1}) yielded a uniform recrystallized microstructure. This even distribution of energy in the deformed material can promote porosity closure in all locations.

RECOMMENDATIONS

This research focused on the thermomechanical characterisation of H13 tool steel, with different holding temperatures and deformation parameters for a forging process. Promising forging parameters were identified from the results, to promote a higher ductility of the material and a better closure of porosity:

- Temperature higher than 1230°C for a complete dissolution of Cr and Mo carbides.
- Strain rate smaller than 0.1 s^{-1} for a uniform deformation and activation of DRX mechanisms.

To achieve considerable deformation with a lower strain rate at the centerline of a large forging, a solution could be to increase the press capacity. This could expand the range of strain rates and increase the deformation achievable. Furthermore, the analysis of the literature and research results inspired many questions about the actual forging process that would require more investigation. First, the review of 3D simulation cases indicated gaps that would require simulations with new sets of parameters for accurate results on Finkl Steel process. The reduction percentage could be set according to the present die shape in industry, that is, a max pass depth equal to the die edge radius of 44.5 mm. Then, lower die overlap could be studied. In addition, diagonal and round cogging could be studied to have a better understanding of the phenomena of void reopening. Finally, the experimental tests provided microstructures showing characteristic features of the deformation conditions. These could be used as reference to analyse micrographs of the defect zones of actual forged pieces. This could demonstrate whether the problem is of metallurgical of thermomechanical nature.

LIST OF REFERENCES

Avner, S. H. (1964). *Introduction to physical metallurgy*. (S.l.) : New York, McGraw-Hill. http://archive.org/details/introductiontoph00avne

Bitterlin, M., Shahriari, D. (2018). Hot Deformation Behavior of a Nickel-modified AISI 4330 Steel. *ISIJ International*, *58*. https://doi.org/10.2355/isijinternational.ISIJINT-2018-034

Buckingham, R., Argyrakis, C., Hardy, M., Birosca, S. (2016). The Effect of Strain Distribution on Microstructural Developments during Forging in a Newly Developed Nickel Base Superalloy. *Materials Science and Engineering: A*, *654*. https://doi.org/10.1016/j.msea.2015.12.042

Buteler, D. I., Neves, P., Ramos, L., Santos, C., Souza, R., Sinatore, A. (2006). Effect of anvil geometry on the stretching of cylinders. *Journal of Materials Processing Technology*, *179*, 50-55. https://doi.org/10.1016/j.jmatprotec.2006.03.079

Campbell, J. (2011). Introduction to Castings Handbook 2011. Dans J. Campbell (Éd.), *Complete Casting Handbook* (p. xxi). Oxford : Butterworth-Heinemann. https://doi.org/10.1016/B978-1-85617-809-9.10027-1

Chadha, K., Shahriari, D., Jahazi, M. (2015). Constitutive modelling of ingot breakdown process of low alloy steels. Bardolino, Italy : Associazione Italiana di Metallurgia. https://espace2.etsmtl.ca/id/eprint/12914/

Chegini, M., Aboutalebi, M., Seyedein, S., Ebrahimi, G., Jahazi, M. (2020). Study on hot deformation behavior of AISI 414 martensitic stainless steel using 3D processing map. *Journal of Manufacturing Processes*, *56*, 916-927. https://doi.org/10.1016/j.jmapro.2020.05.008

Chen, J., Chandrashekhara, K. (2012). Study of void closure in hot radial forging process using 3D nonlinear finite element analysis. *The International Journal of Advanced Manufacturing Technology*, *62*. https://doi.org/10.1007/s00170-011-3876-3

Chentouf, S., Chamanfar, A., Jahazi, M. (2020). Austenite grain growth and hot deformation behavior in a medium carbon low alloy steel. *Journal of Materials Research and Technology*, *9*, 12102-12114. https://doi.org/10.1016/j.jmrt.2020.08.114

Choi, S. K., Chun, M., Van Tyne, C., Moon, Y. (2006). Optimization of open die forging of round shapes using FEM analysis. *Journal of Materials Processing Technology*, *172*(1), 88-95. https://doi.org/10.1016/j.jmatprotec.2005.09.010

Connolly, B., Paules, J., DeArdo, A. (2015). The effects of composition and thermal path on hot ductility of forging steels. *Metallurgia Italiana*, (107(1)), 3-9.

Dehghan-manshadi, A., Hodgson, P. (2007). Effect of Initial Grain Size on the Dynamic Recrystallization Behaviours of Austenite. *Materials Science Forum - MATER SCI FORUM*, *561-565*, 33-36. https://doi.org/10.4028/www.scientific.net/MSF.561-565.33

Dieter, G. E. (1988). *Mechanical Metallurgy*. (S.l.) : McGraw-Hill.

Ebrahimi, R., Zahiri, S., Najafizadeh, A. (2006). Mathematical modelling of the stress–strain curves of Ti-IF steel at high temperature. *Journal of Materials Processing Technology*, *171*(2), 301-305. https://doi.org/10.1016/j.jmatprotec.2005.06.072

Ghiotti, A., Fanini, S., Bruschi, S., Bariani, P.F. (2009). Modelling of the Mannesmann effect. *CIRP Annals*, *58*(1), 255-258. https://doi.org/10.1016/j.cirp.2009.03.099

Guo, Z., Lasne, P., Saunders, N., Schillé, J.-P. (2018). Introduction of materials modelling into metal forming simulation. *Procedia Manufacturing*, *15*, 372-380. https://doi.org/10.1016/j.promfg.2018.07.232

Harris, N. (2016). *Determination of optimal forging conditions for void elimination in large steel ingots*. masters. École de technologie supérieure, Montréal. https://espace.etsmtl.ca/id/eprint/1771/

He, J., Cui, Z., Chen, F., Xiao, Y., Ruan, L. (2013). The new ductile fracture criterion for 30Cr2Ni4MoV ultra-super-critical rotor steel at elevated temperatures. *Materials & Design (1980-2015)*, *52*, 547-555. https://doi.org/10.1016/j.matdes.2013.05.080

Humphreys, F. J. (Éd.), Haterly, M. (1995). *Recrystallization and Related Annealing Phenomena*. Oxford : Pergamon. https://doi.org/10.1016/B978-0-08-041884-1.50002-7

Kchaou, M., Elleuch, R., Desplanques, Y., Boidin, X., Degallaix, G. (2010). Failure mechanisms of H13 die on relation to the forging process – A case study of brass gas valves. *Engineering Failure Analysis*, *17*(2), 403-415. https://doi.org/10.1016/j.engfailanal.2009.08.015

Khan, F. (2018). The Effect of Soaking on Segregation and Primary-Carbide Dissolution in Ingot-Cast Bearing Steel. https://doi.org/10.3390/met8100800

Lan, P. (2014). Numerical analysis of macrosegregation and shrinkage porosity in large steel ingot. *Ironmaking & Steelmaking*, *41*, 598-606. https://doi.org/10.1179/1743281213Y.0000000172

Lee, M. C., Jang, S., Cho, J., Joun, M. (2008). Finite element simulation of pore closing during cylinder upsetting. *International Journal of Modern Physics B - IJMPB*, *22*. https://doi.org/10.1142/S0217979208051145

Li, J., Li, J., Wang, L., Li, L. (2014). Study on Carbide in Forged and Annealed H13 Hot Work Die Steel. *High Temperature Materials and Processes*, *34*, 593-598. https://doi.org/10.1515/htmp-2014-0073

Li, T., Zhao, B., Lu, J., Xu, L., Zou, Y. (2019). A Comparative Study on Johnson Cook, Modified Zerilli–Armstrong, and Arrhenius-Type Constitutive Models to Predict Compression Flow Behavior of SnSbCu Alloy. *Materials*, *12*, 1726. https://doi.org/10.3390/ma12101726

Lin, M., Zhao, X., Han, L., Liu, Q., Gu, J. (2016). Microstructural Evolution and Carbide Precipitation in a Heat-Treated H13 Hot Work Mold Steel. *Metallography, Microstructure, and Analysis*, *5*(6), 520-527. https://doi.org/10.1007/s13632-016-0318-5

Liu, J., Wang, G., Bao, Y., Yang, Y., Yao, W., Gui, X. (2012). Inclusion Variations of Hot Working Die Steel H13 in Refining Process. *Journal of Iron and Steel Research, International*, *19*(11), 1-7. https://doi.org/10.1016/S1006-706X(13)60012-6

Loucif, A., Ben Fredj, E., Harris, N., Shahriari, D., Jahazi, M., Lapierre-Boire, L. (2018). Evolution of A-Type Macrosegregation in Large Size Steel Ingot After Multistep Forging and Heat Treatment. *Metallurgical and Materials Transactions B*, *49*, 1046-1055. https://doi.org/10.1007/s11663-018-1255-2

Marashi, J., Yakushina, E., Xirouchakis, P., Zante, R., Foster, J. (2017). An evaluation of H13 tool steel deformation in hot forging conditions. *Journal of Materials Processing Technology*, *246*, 276-284. https://doi.org/10.1016/j.jmatprotec.2017.03.026

Mukherjee, M., Prahl, U., Bleck, W. (2010). Modelling of Microstructure and Flow Stress Evolution during Hot Forging. *steel research international*, *81*. https://doi.org/10.1002/srin.201000114

Najafizadeh, A., Jonas, J. (2006). Predicting the Critical Stress for Initiation of Dynamic Recrystallization. *ISIJ International*, *46*(11), 1679-1684.

Ning, A. (2017). Precipitation Behavior of Carbides in H13 Hot Work Die Steel and Its Strengthening during Tempering. *Metals*. https://www.researchgate.net/publication/313945882_Precipitation_Behavior_of_Carbides_in_H13_Hot_Work_Die_Steel_and_Its_Strengthening_during_Tempering

Open Die Forging. (1988). Dans *ASM Handbook* (Vol. 14). (S.l.) : (s.n.). https://www.asminternational.org/asm-handbook-volume-14a-metalworking-bulk-forming/results/-/journal_content/56/06957G/PUBLICATION/

Porter, D. A., Easterling, K. E. (2009a). *Phase Transformations in Metals and Alloys*. (S.l.) : CRC Press.

Simsir, C., Duran, D. (2018). A flow stress model for steel in cold forging process range and the associated method for parameter identification. *The International Journal of Advanced Manufacturing Technology*, *94*. https://doi.org/10.1007/s00170-017-1160-x

Tamura, K., Tajima, J. (2003). Optimisation of open die forging condition and tool design for ensuring both internal quality and dimensional precision by three-dimensional rigid–plastic finite element analysis. *Ironmaking & Steelmaking*, *30*(5), 405-411. https://doi.org/10.1179/030192303225001801

Tamura, I., Watanabe, S., Watanabe, K. (1984). Development of New Processes for Control of Internal Deformation and Internal Stress in Hot Free Forging of Heavy Ingots. *Transactions ISIJ*, *24*, 101-106.

Tremaine, A. (2005). Characterization of Internal Defects in Open Die Forgings. Colorado School of Mines, Golden.

Vamsi Krishna, B., Sidhu, R. (2019). Analysis of Center Burst During Hot Forging. https://doi.org/10.31399/asm.fach.process.c9001615

Wang, H., Li, J., Shi, C., Li, J., He, B. (2017). Evolution of Carbides in H13 Steel in Heat Treatment Process. *MATERIALS TRANSACTIONS*, *58*, 152-156. https://doi.org/10.2320/matertrans.M2016268

Wang, W., Ma, Y., Yang, M., Jiang, P., Yuan, F., Wu, X. (2018). Strain Rate Effect on Tensile Behavior for a High Specific Strength Steel: From Quasi-Static to Intermediate Strain Rates. *Metals*, *8*(1), 11. https://doi.org/10.3390/met8010011

Wen, X.-L. (2018). Void Evolution Law and Its Control in Steel Ingot Forging. *springerprofessional.de*. Repéré à https://www.springerprofessional.de/en/void-evolution-law-and-its-control-in-steel-ingot-forging/17003888

Zhang, T.-B., Shen, Y., Liu, P., Yong, Q., Bao, Y. (2013). New Type Austenite Dynamic Recrystallization of Microalloyed Forging Steels 38MnVS During Forging Process. *Journal of Iron and Steel Research, International*, *20*, 57-60. https://doi.org/10.1016/S1006-706X(13)60098-9

Zhang, X. X., Ma, C., Sun, Y., Ma, F. (2012). Stress Analysis and Failure Mechanism of H13 Steel Hot-Forging Die for Automobile Engine Crankshaft. *Applied Mechanics and Materials*, *217-219*, 1994-1997. https://doi.org/10.4028/www.scientific.net/AMM.217-219.1994

Zhou, J., Blackketter, J., Nash, P. (2012). FEM Study of Centerline Defect Closure in Large Open-Die Forgings. *TMS Annual Meeting*, 63-70. https://doi.org/10.1002/9781118359341.ch7